DISS. ETH NO. 30049

Hyperspectral long-distance metrology using a femtosecond laser supercontinuum

A thesis submitted to attain the degree of

DOCTOR OF SCIENCES

(Dr. sc. ETH Zurich)

presented by

Pabitro Ray

M.S., Indian Institute of Technology Madras

born on 26.07.1990

accepted on the recommendation of

Prof. Dr. Andreas Wieser
Dr. David Salido-Monzú
Prof. Dr. Luis García-Asenjo Villamayor
Prof. Dr. Werner Lienhart

2024

Abstract

Rapid and accurate distance measurements over ranges from tens of meters to kilometers are essential in various applications, such as large-scale industrial manufacturing, alignment of particle accelerators, surveying, and three-dimensional (3D) digitization of our environment. Conventionally, electro-optical distance measurement (EDM) techniques based on nearly monochromatic laser sources are widely used in such applications. The measurement principle relies on monitoring the round-trip propagation delay of optical signals to estimate the distance to a remote target. However, for distances exceeding several hundred meters, the measurement accuracy on cooperative targets is practically limited by the uncertainties in estimating the refractive index of air along the propagation path. It arises from spatial and temporal meteorological variations in the atmosphere and may lead to apparent distance errors of several millimeters or more. Nevertheless, these errors can be compensated by exploiting atmospheric dispersion through simultaneous distance measurements at multiple wavelengths, i.e. multiwavelength EDM. Apart from long-distance metrology, EDM also plays a pivotal role in LiDAR applications for capturing the 3D geometry of natural surfaces. Combining the range information with extended surface reflectance data over multiple (multispectral) or a continuous distribution of wavelengths (hyperspectral) has proved advantageous for automated material classification, point-cloud segmentation, and remote sensing applications.

With the advent of mode-locked femtosecond (fs) lasers, optical frequency combs have emerged as a promising alternative to conventional continuous-wave modulated lasers for high-precision distance metrology. While benefiting from the frequency comb technology, optical supercontinuum (SC) coherently broadened from a mode-locked fs laser is a viable solution for applications requiring measurements over a continuous broadband spectrum or on several spectral bands. This thesis introduces the use of SC for multiwavelength refractivity-compensated EDM and hyperspectral LiDAR for precision laser scanning. Corresponding experimental platforms are developed for the related investigations. Distance measurements are estimated from the differential phase delay of the intermode beats generated upon photodetection of the SC. Experimental analyses show the range precision, accuracy, factors influencing the measurement noise, and current limitations of the technique. The results obtained from the multiwavelength EDM demonstrate effective inline refractivity compensation, indicating the possibility of achieving precise distance measurements in practical conditions. Experiments using the developed hyperspectral LiDAR show favorable range precision compared to established solutions. They highlight its potential for joint high-precision scanning, spectrum-based material classification, and remote sensing of vegetation. The experimental investigations indicate that SC-based distance measurements using the intermode beating approach may lead to a promising technological basis for hyperspectral long-distance metrology.

Kurzfassung

Schnelle und genaue Distanzmessungen über Entfernungen von einigen zehn Metern bis hin zu Kilometern sind für verschiedenen Anwendungen unerlässlich, zum Beispiel in industriellen Großproduktionen, bei der Ausrichtung von Teilchenbeschleunigern, bei der Vermessung und der 3D-Digitalisierung unserer Umwelt. Üblicherweise werden in solchen Anwendungen elektro-optische Distanzmessungen (EDM) eingesetzt, die auf nahezu monochromatischen Laserquellen basieren. Das Messprinzip beruht auf der Beobachtung der Laufzeitverzögerung optischer Signale, um die Entfernung zu einem entfernteren Ziel abzuschätzen. Bei Entfernungen von mehreren hundert Metern ist die Messgenauigkeit jedoch praktisch durch die Unsicherheiten bei der Schätzung des Brechungsindexes der Luft entlang des Ausbreitungsweges begrenzt. Die Schwankungen des Brechungsindexes resultieren aus räumlichen und zeitlichen meteorologischen Veränderungen in der Atmosphäre und können zu scheinbaren Entfernungsfehlern von mehreren Millimetern oder mehr führen. Sie können jedoch durch Ausnutzung der atmosphärischen Dispersion durch gleichzeitige Messungen bei mehreren Wellenlängen, d. h. durch Mehrwellenlängen-EDM, kompensiert werden. Neben dem Einsatz für die Distanzmessung über grosse Entfernungen spielt EDM auch eine zentrale Rolle bei Laserscanning- oder LiDAR-Anwendungen zur Erfassung der 3D-Geometrie natürlicher Oberflächen. Die Kombination der Entfernungsinformationen mit zusätzlichen Oberflächenreflexionsdaten erfasst mit mehreren Wellenlängen (multispektrale) oder eine kontinuierliche Verteilung der Wellenlängen (hyperspektrale) hat sich für die automatische Materialklassifizierung, die Segmentierung von Punktwolken und Fernerkundungsanwendungen als vorteilhaft erwiesen.

Mit dem Aufkommen der modengekoppelten Femtosekundenlaser (fs-Laser) haben sich optische Frequenzkämme als vielversprechende Alternative zu konventionellen wellenmodulierten Lasern für die hochpräzise Entfernungsmessung erwiesen. Das optische Superkontinuum (SC), das von einem modengekoppelten fs-Laser kohärent verbreitert wird, ist eine praktikable Lösung für Anwendungen, die Messungen in einem kontinuierlichen Breitbandspektrum oder in mehreren Spektralbändern erfordern, und profitiert daher von der Frequenzkammtechnologie. In dieser Arbeit wird der Einsatz von SC für multiwellenlängenkompensiertes EDM und hyperspektrales LiDAR für präzises Laserscanning vorgestellt. Entsprechende experimentelle Plattformen werden für die Untersuchungen entwickelt. Entfernungsmessungen werden aus der differentiellen Phasenverzögerung der bei der Photodetektion des SC erzeugten Intermode-Beats geschätzt. Es werden experimentelle Analysen zur Entfernungspräzision, zur Gen-auigkeit, zu Faktoren die das Messrauschen beeinflussen, und zu den derzeitigen Grenzen der Technik vorgestellt. Die Ergebnisse des Mehrwellenlängen-EDM zeigen eine effektive Inline-Brechungskompensation, was auf die Möglichkeit genauer Entfernungsmessungen unter praktischen Bedingungen hinweist. Experimente mit dem entwickelten hyperspektralen LiDAR zeigen eine vorteil-

hafte Entfernungsgenauigkeit im Vergleich zu den etablierten Lösungen. Sie verdeutlichen das Potenzial des Systems für das gemeinsame hochpräzise Scannen, die spektralbasierte Materialklassifizierung und die Fernerkundung von Vegetation. Weitere experimentelle Untersuchungen deuten darauf hin, dass SC-basierte Entfernungsmessungen mit dem Intermode-Beating-Ansatz zu einer vielversprechenden technologischen Basis für die hyperspektrale Langstreckenmesstechnik führen können.

Acknowledgements

I extend my sincere gratitude to all who have supported and guided me during my doctoral studies. Foremost, I am immensely grateful to my thesis supervisor, Prof. Dr. Andreas Wieser, for his constant support and guidance. His feedback has been instrumental in shaping this research and enriching my personal and professional skills. I sincerely thank him for allowing me the freedom to explore and experiment with different ideas, and for fostering a positive research and learning environment within our group. I am also deeply grateful to Dr. David Salido-Monzú, for being a great mentor and colleague. I truly thank him for his exceptional support in laying the foundation of this work, and for the extensive discussions that kept me motivated throughout this journey.

I sincerely thank my committee members, Prof. Dr. Luis García-Asenjo Villamayor and Prof. Dr. Werner Lienhart, for accepting to review my thesis and for providing their valuable time and feedback.

Many thanks to Mr. Robert Presl for his outstanding technical support in designing and constructing the mechanical assemblies of the setup. His prompt assistance was pivotal in enabling the experiments to be executed on time. I also thank him for our countless discussions to address the technical challenges together.

I am grateful to the Swiss National Science Foundation (SNSF) for co-funding and supporting this research. I thank Ms. Yu Han for her collaboration in this SNSF project. Our discussions have been extremely beneficial in advancing this research and have enriched my understanding of the subject through mutual learning. I also thank Dr. Jemil Avers Butt for collaborating on this project and for his help in developing the theoretical framework. I extend my thanks to Mr. Sandro Camenzind and Ms. Nathalie Ryter for their Master's theses in our group, which has significantly contributed to developing my work.

My heartfelt thanks to all the current and former members of our group for the numerous scientific discussions, interesting conversations, dinner gatherings, friendly table tennis matches, trips, and excursions. Thanks to them, my experience here has been truly incredible and memorable. Also, many thanks to the administrative assistants of our group and institute for their kind support and help with various organizational tasks. Additionally, I want to express my sincere gratitude to my Master's thesis advisors at IIT Madras for introducing me to scientific research and supporting my aspiration to pursue doctoral studies. Finally, I am wholeheartedly grateful to my friends, family, and parents for always being there for me and for their constant love and encouragement.

Zurich, March 2024 Pabitro Ray

Contents

Abstract iii

Kurzfassung v

Acknowledgements vii

List of Acronyms xi

1. Introduction 1
- 1.1. Motivation . . . 1
- 1.2. Research questions . . . 3
- 1.3. Outline & contributions . . . 4
  - 1.3.1. High-precision intermode-beating EDM . . . 4
  - 1.3.2. Refractivity corrected distance measurement . . . 5
  - 1.3.3. Hyperspectral LiDAR for precision laser scanning . . . 6
  - 1.3.4. Improved radiometric correction of backscatter intensity . . . 7
- 1.4. Relevance to science and economy . . . 7

2. Background 9
- 2.1. Electro-optical distance measurement . . . 9
- 2.2. Influence of refractivity variations . . . 12
  - 2.2.1. Empirical equations . . . 12
  - 2.2.2. Refractivity errors . . . 14
  - 2.2.3. Dispersion-based refractivity correction . . . 15
- 2.3. Coherent supercontinuum . . . 18
  - 2.3.1. Optical frequency comb . . . 19
  - 2.3.2. Distance measurement using frequency combs . . . 21

3. High-precision intermode-beating EDM 23
- 3.1. Introduction . . . 24
- 3.2. Approach . . . 25
  - 3.2.1. Dual-wavelength method . . . 25
  - 3.2.2. Intermode beating . . . 27
- 3.3. Experimental setup . . . 28
- 3.4. Results . . . 31
- 3.5. Conclusions and outlook . . . 33

4. Refractivity corrected distance measurement 35
- 4.1. Introduction . . . 36

4.2. Methods . . . 38
4.2.1. Experimental approach . . . 38
4.2.2. Experimental setup . . . 40
4.3. Results . . . 43
4.3.1. Measurement precision . . . 43
4.3.2. Relative accuracy . . . 45
4.3.3. Long-term stability . . . 46
4.3.4. Refractivity compensation . . . 47
4.4. Conclusion and outlook . . . 49

5. Hyperspectral LiDAR for precision laser scanning 51
5.1. Introduction . . . 52
5.2. Methods . . . 53
5.2.1. Experimental setup . . . 53
5.2.2. Target properties . . . 56
5.3. Experimental results . . . 59
5.3.1. Range precision . . . 59
5.3.2. Relative range accuracy . . . 62
5.3.3. Hyperspectral laser scanning . . . 63
5.4. Conclusion and Outlook . . . 65
5.5. Supplement 1 . . . 65
5.5.1. Design of the scanning unit . . . 65
5.5.2. Calibration . . . 67

6. Improved radiometric correction of backscatter intensity 69
6.1. Introduction . . . 70
6.2. Experimental approach . . . 71
6.3. Results . . . 74
6.3.1. Range performance . . . 74
6.3.2. Radiometric correction . . . 76
6.3.3. Relevance on the example of vegetation health monitoring . . . 79
6.4. Conclusion and outlook . . . 81

7. Conclusions 83
7.1. Knowledge gained . . . 83
7.2. Limitations . . . 85
7.3. Outlook . . . 87

A. Bibliography 89

B. List of Publications 99

List of Acronyms

ADC Analog to digital converter

AoI Angle of incidence

APD Avalanche photodiode

BE Beam expander

BPF Bandpass filter

BSF Beam sampler

CC Corner cube

CLK Clock

CW Continuous wave

DM Dichroic mirror

EDM Electro-optical distance measurement

FC Frequency comb

FL Focusing lens

GNSS Global navigation satellite system

GPS Global positioning system

HLS Hyperspectral laser scanning

HSL Hyperspectral LiDAR

HWP Half-wave plate

IF Intermediate frequency

IQ In-phase quadrature

LED Light emitting diode

LiDAR Light detection and ranging

LO Local oscillator

LoS Line of sight

MLL Mode-locked laser

MMF Multi-mode fiber

NDF Neutral density filter

NIR Near infrared

OAP Off-axis parabolic

PBS Polarization beam splitter

PCF Photonic crystal fiber

PD Photodetector

PLL Phase-locked loop

PSD Power spectral density

QWP Quarter-wave plate

RF Radio frequency

SC Supercontinuum

SH Mechanical shutter

SNR Signal-to-noise ratio

TLS Terrestrial laser scanners

ToF Time of flight

1 Introduction

1.1. Motivation

Distance meters based on the visible and near-infrared (NIR) light as carrier waves are called electro-optical distance measurement (EDM) instruments [1]. These instruments enable non-contact linear distance measurements over a few mm to several km [2]. Conventional approaches to EDM involve time-of-flight (ToF) measurements of pulsed lasers or phase-based measurements on amplitude-modulated continuous-wave (CW) lasers, both typically implemented with monochromatic laser sources [3]. The technology is a backbone of laser scanning and precision distance metrology in various applications, such as industrial manufacturing, alignment of particle accelerators, surveying, deformation monitoring, and enhanced 3D digitization of our surroundings [4].

Typically, measurements requiring high-accuracy distance observations over long distances use cooperative targets, such as corner cube retroreflectors. Cooperative targets reflect most of the emitted optical energy to the instrument, ensuring an adequate signal-to-noise ratio (SNR). In addition to cooperative targets, EDM can also measure distances to diffusely reflective natural surfaces. The technology is also known as light detection and ranging (LiDAR). Scanning LiDAR, e.g., in laser scanning applications, generates 3D geometric information of natural targets in the form of point clouds [5]. The intensity of the backscattered optical power received at the instrument and the topographic features of the reflecting surface play a critical role in the error budget [6].

However, for long distances exceeding several hundred meters measured on cooperative targets, the achievable accuracy is primarily limited by uncertainties in estimating the refractive index of air along the propagation path. It occurs from variations in the meteorological parameters such as temperature, pressure, relative humidity, and carbon dioxide content in the atmosphere [7]. These variations can induce apparent distance errors of several mm or more. Conventionally, the effective refractive index is estimated from empirical equations like Edlén's [8, 9] or Ciddor's equations [10, 11] by monitoring the meteorological parameters mainly at the instrument or occasionally at a few locations along the propagation path. Refraction-induced distance errors are then mitigated through forward modeling. Although this method is effective for relatively short distances, it typically fails to represent the true spatial distribution of the refractive index along the entire optical path over long distances. Distance errors of more than 5 ppm (parts-per-million) may persist even if the meteorological measurements are taken at both the endpoints (i.e. at the instrument and the target location) [12]. Recent research has demonstrated that achieving distance corrections below the ppm level is challenging in practical outdoor conditions, even with a dense set of meteorological measurements along the optical path [13].

However, since air is dispersive (i.e., the refractive index of air is a function of the optical wavelength), refractivity errors can be compensated by acquiring distance measurements simultaneously on two or more wavelengths. This multiwavelength EDM approach enables inline refractivity correction, without requiring external meteorological measurements. The theoretical foundation of this method was first introduced over 50 years ago [14]. The authors presented a dual-wavelength solution suitable for dry air (relative humidity=0%). Refractivity compensation using the dual-wavelength EDM approach is also known as the two-color method. In humid air conditions (relative humidity $> 0\%$), using more than two wavelengths can mitigate the impact of humidity variations [15, 16]. However, a fundamental limitation of the multiwavelength EDM approach is that the measurement uncertainty of the observed optical path length differences is amplified by a dispersion-related scaling factor. This leads to a higher uncertainty in refractivity-compensated distance measurements compared to the individual optical path length. Therefore, achieving highly precise and accurate distance observations of the differences between the wavelengths is crucial.

In the subsequent years, the two-color method was experimentally demonstrated by using individual lasers and filtered lamp sources at different wavelengths [17, 18]. Based on the same principle, the commercial instrument Terrameter [19] was later conceived in 1981. The instrument claimed an accuracy of about 0.1 ppm over a range of 15 km under favorable conditions. The Terrameter has been the sole commercially manufactured two-color EDM instrument for refractivity correction. However, adapting the instrument at every measurement location required extensive efforts and constant specialized engineering supervision during operation [20]. Moreover, at that time, long-distance measurements spanning several kilometers could be replaced by high-accuracy GPS monitoring, and further developments and commercialization of dual-wavelength EDM did not materialize. Nevertheless, applications such as geomonitoring, tunnel surveying, urban monitoring, and underground construction measurements, particularly where GNSS is not applicable, still require precise long-distance measurements. The latest progress in optical and electronic technologies has stimulated renewed interest in developing dual or multiwavelength EDM solutions. Sec. 2.2.3 outlines a few of the early experimental developments on dual and multiwavelength EDM.

In addition to refractivity compensation, there is also a growing interest in incorporating multiple wavelengths (multispectral) or a continuous distribution of wavelengths (hyperspectral) for laser scanning [21, 22]. Photogrammetric methods are widely used to generate 3D point clouds with spectral information by combining images from a multi- or hyperspectral camera with geometric information derived from those images. However, this approach requires accurate co-registration between the spectral and geometric data derived from the captured images [23]. On the other hand, multi- or hyperspectral LiDAR enables simultaneous acquisition of 3D geometry and spectral reflectance of natural targets, independent of ambient illumination [24, 25]. This ensures precise point-wise mapping of both the range and spectral information of a target without the need for additional co-registration between the datasets. The technique has proven effective for automated point cloud segmentation and material classification based on spectral signatures [26]. However, the established hyperspectral LiDAR solutions offer mm to cm level range precision over distances exceeding a few tens of meters. Improving range

precision may enhance surface reconstruction and improve the estimation of surface orientation which, for instance, is crucial for radiometric correction of intensities.

In recent years, the discovery of optical frequency comb (FC) technology based on mode-locked femtosecond (fs) lasers has led to significant developments in precision distance metrology. In the time domain, the output of a mode-locked laser (MLL) appears as a train of ultrashort optical pulses with a fixed pulse-repetition rate. This results in a series of stable, narrow linewidth, and equally spaced spectral lines in the frequency domain, resembling a comb-like structure, and is therefore referred to as frequency combs [27]. The frequency spacing between the optical comb lines corresponds to the pulse repetition rate of the mode-locked laser. When referenced to an atomic clock, distance measurements obtained from the FC technology can be traced to the SI definition of the meter [28]. Therefore, FC-based distance measurement has emerged as a promising alternative to the established methods [29]. This technique can be extended to ultra-broadband optical supercontinuum (SC) sources generated through coherent spectral broadening of a FC. A SC offers increased flexibility for measurements on several or on a continuous distribution of wavelengths over a broad bandwidth of around hundreds of nm. While distance measurement techniques using FC have been extensively investigated and documented in the literature, the application of SC for distance measurements was relatively unexplored in the past.

This thesis introduces the use of such a coherent SC source for multiwavelength refractivity compensated EDM and hyperspectral LiDAR. The proposed measurement principle is based on monitoring the phase delay observations on the intermode beats generated by direct photodetection of the SC or filtered spectral bands from the SC. The intermode beats are electrical radio-frequency (RF) comb lines, where each beat note represents an inherently high-quality and high-frequency electrical signal suitable for distance measurements. The frequency spacing between the beat notes is equal to the pulse repetition frequency of the seed mode-locked laser. Related experimental investigations are conducted to identify the fundamental limitations of the proposed approach and address practical solutions for its implementation. Corresponding experimental platforms are developed for carrying out such measurements.

1.2. Research questions

This thesis addresses the following research questions:

- Can the intermode beats obtained from a spectrally broadened mode-locked fs laser (i.e., supercontinuum) achieve sub-mm level precision for EDM over a few hundred meters?
- What are the fundamental and practical limitations of employing this approach to compensate for refractivity-induced distance errors?
- Can this approach facilitate 3D geometric acquisition of natural targets with sub-mm to mm level range precision over a few tens of meters, while simultaneously capturing the hyperspectral reflectance of the target?

1.3. Outline & contributions

This thesis is structured as a *cumulative dissertation*, in accordance with the ETH Zurich ordinance on the doctorate of 2021, detailed stipulations of 2022, and additional provisions to the ordinance on doctoral studies of 2015 of the Department of Civil, Environmental, and Geomatics Engineering. Sec. 1.3.1– 1.3.4 below provide an overview of the methodology and contributions of Chapters 3–6 of this thesis. These chapters 3–6 are the four peer-reviewed contributions that represent the core of the cumulative dissertation. The relevance of this thesis to science and economy is discussed in Sec. 1.4. Chapter 2 offers a brief review of the existing literature and establishes the foundational framework for the subsequent chapters. Chapter 3–6 present the selected research articles in their original published or submitted form, typeset to the current layout with only minor typographical corrections. Finally, Chapter 7 summarizes the key findings of this work along with an outlook on directions for future research.

The thesis contributes to understanding the capabilities and limitations of SC-based distance metrology for inline refractivity compensation and hyperspectral laser scanning. These contributions are based on experimental investigations utilizing a SC coherently broadened from a mode-locked fs laser. The emphasis is on leveraging phase-based distance measurements derived from the intermode beats. The experiments are conducted under controlled conditions at the Geodetic Metrology Laboratory of our institute on a 50 m long linear comparator bench, acting as a delay line for measuring the distances. Controlled refractivity variations necessary for our investigation were created along the delay line of the comparator bench using a refraction modifying element (described in Chapter 4). The primary contributions of this thesis include: i) demonstrating high-precision EDM on a cooperative target using the intermode beats obtained at multiple wavelengths filtered from the SC (Sec. 1.3.1), ii) inline refractivity correction using simultaneously acquired distance measurements at two wavelengths (two-color method) and assessing its performance (Sec. 1.3.2), iii) development of hyperspectral LiDAR for laser scanning of natural targets with enhanced range precision and spectrum-based material classification (Sec. 1.3.3), iv) demonstrating the utility of high-precision ranging along with hyperspectral information for radiometric calibration of the acquired intensities and remote sensing of vegetation (Sec. 1.3.4).

1.3.1. High-precision intermode-beating EDM

Chapter 3 corresponds to the publication Ray et al. (2023) High-precision intermode beating electro-optic distance measurement for mitigation of atmospheric delays [30], published in the Journal of Applied Geodesy. It presents a novel experimental basis for high-precision multiwavelength EDM using a SC. Distances are derived from phase-delay observations on the intermode beat notes obtained on two spectral bands filtered from the SC. Cooperative targets are used in these experiments. The feasibility of this approach has previously been demonstrated over very short distances of only about 5 cm [31]. I now extended the previous work by showing comparable performance over 50 m, representing three orders of magnitude longer range. The experimental setup is designed to be adaptable for even longer distances, potentially extending by another 1-2 orders of

magnitude. A unique aspect of our approach is the capability to support measurements on any set of chosen wavelengths from within the SC. Herein, we demonstrate this by using optical band-pass filters and multiple detectors in parallel.

Main scientific contributions:

1. We demonstrated an empirically estimated measurement precision of around 30 µm at a distance of 50 m using a specific wavelength pair (590 and 890 nm) filtered from the SC. Each data point was averaged over an acquisition window of 3 ms.
2. As the underlying measurement processes at these timescales are found to be dominated by white noise, the distance precision can be further improved to < 10 µm by increasing the data integration time to around 1 s.
3. Deviations between our results and those obtained from a reference He-Ne interferometer (for ground truth measurements) were within 100 µm for displacements up to 50 m. This implies a relative accuracy of about 2 ppm.
4. We identified that the long-term measurement stability is primarily affected by optical power fluctuations and thermally-induced differential length changes in the RF cables. These factors were recognized as the main practical limitations of the experimental setup presented in this study, and were improved for subsequent publications.

1.3.2. Refractivity corrected distance measurement

Chapter 4 corresponds to the publication Ray et al. (2024) Refractivity corrected distance measurement using the intermode beats derived from a supercontinuum [32], published in Optics Express. It demonstrates an improved experimental design for SC-based multiwavelength EDM in comparison to the setup used in [30] (Chapter 3). The optical and electronic designs are adapted to enhance measurement precision and ensure long-term measurement stability over a few hours. The dependency of the estimated precision on distance and data integration time is experimentally evaluated. Our investigation also includes an assessment of the underlying noise processes, accuracy, and long-term precision. Pressure-induced refractivity variations are introduced along the delay line. We then use the two-color method to demonstrate refractivity compensated EDM. The results indicate the potential of SC-based multiwavelength EDM to achieve high-accuracy long-distance measurements. The primary error sources in the measurements are attributed to optical power and beam-pointing fluctuations.

Main scientific contributions:

1. We achieved an empirically estimated measurement precision of around 10 µm at 50 m for the selected wavelengths (590 and 890 nm), with a data integration time of 27 ms.
2. The estimated distance-dependent component of the measurement precision is below 0.2 ppm. Thus, indicating the potential for achieving sub-mm level precision over several km.

3. The relative accuracy, compared to results obtained from a reference interferometer, was on the order of 0.1 ppm for displacements up to 50 m.

4. We demonstrated inline refractivity compensation using the two-color method. A pressure-induced optical path length change of about 0.4 mm was introduced along the probe path. The refractivity-corrected distance measurements exhibited an empirical standard deviation of less than 0.1 mm at 15 m without any external meteorological observation. This shows an effective two-color refractivity compensation, highlighting promising perspectives for extending the method to longer, practically useful ranges.

1.3.3. Hyperspectral LiDAR for precision laser scanning

Chapter 5 corresponds to the publication Ray et al. (2023) Supercontinuum-based hyperspectral LiDAR for precision laser scanning [33], published in Optics Express. Hyperspectral LiDAR (HSL) enables accurate remote mapping of reflectance signatures onto the 3D surface geometry of natural targets. The established HSL solutions reported in the literature typically use SC sources incoherently broadened from pulsed lasers. Such solutions have shown mm to cm level range precision over a few tens of meters using direct delay-based ToF measurements. In Chapter 5, we demonstrate a novel approach to hyperspectral LiDAR using SC that is coherently broadened from a frequency comb [33]. Our approach shows a sub-mm to mm level of range precision over a few tens of meters. Here, the range measurements are obtained from the phase delay of the intermode beat notes generated upon direct photodetection of the whole SC (unlike the spectrally filtered bands of the SC as in Sec. 1.3.1 and Sec. 1.3.2). For each scanned point, the backscattered spectrum is acquired using a commercial spectrometer over the entire spectral range of the SC output. Chapter 5 describes the features and limitations of our experimental approach and the scanning unit. The developed experimental setup generates hyperspectral 3D point clouds by scanning natural surfaces and scenes. We experimentally analyzed the dependency of range precision on the measurement distance, data integration time, and surface reflectance of the target. Experimental results show high-precision ranging augmented with hyperspectral data, indicating the potential of this approach for finer point cloud segmentation and spectrum-based material classification.

Main scientific contributions:

1. We achieved an empirically estimated measurement precision below 0.1 mm for stand-off distances up to 50 m on a diffusely reflective target with around 89% surface reflectance. This is one order of magnitude better than the established HSL alternatives. In this work, each data point was averaged over 13 ms.

2. We analyzed the range performance in terms of distance to the target, surface reflectance, and data integration time. The range precision was found to be directly proportional to distance squared, indirectly proportional to reflectance, and inversely proportional to the square root of integration time over certain timescales.

3. Comparing our results with a reference interferometer showed a relative range accuracy of around 10 ppm for stand-off distances of up to 50 m.

4. Using the captured reflectance signatures, the 3 materials (beech wood, balsa wood, low-density fiberboard) used in these experiments could be distinguished for each point in the 3D point cloud by classification.

1.3.4. Improved radiometric correction of backscatter intensity

Chapter 6 corresponds to the publication Ray et al. (2023) High-precision hyperspectral laser scanning for improved radiometric correction of backscatter intensity [34], currently under review. Radiometric data in laser scanning offers valuable insights into the surface characteristics and material properties of a target. However, factors such as atmospheric conditions, stand-off distance, sensor characteristics, and the angle of incidence can introduce a bias in the captured radiometric data. Accurately estimating surface geometry and its orientation is crucial for mitigating the bias introduced by the angle of incidence (AoI) and achieving an enhanced radiometric correction. In Chapter 6, we present an application of the developed hyperspectral LiDAR (mentioned in Sec. 1.3.3) for radiometric correction of intensities with reduced AoI bias. This approach benefits from the high-precision range observations of the developed hyperspectral LiDAR. We also assessed the impact of range precision on estimating the surface normals. These measurements were carried out at a stand-off range of 5 m. Additionally, we utilized the radiometrically corrected hyperspectral signatures to derive vegetation indices that are commonly used as plant health indicators. The results highlight new opportunities for future research on plant phenotyping and remote sensing of vegetation.

Main scientific contributions:

1. We achieved a scanning range performance that is comparable to or better than that of commercial state-of-the-art terrestrial laser scanners (TLS). While these TLSs use a single-wavelength narrow linewidth laser source, our approach additionally provides a point-wise hyperspectral signature.

2. By exploiting the precise geometric information, we presented a data-driven approach for accurately estimating local surface geometry (orientation, surface normal, and AoI). The improved estimation of the surface orientation allows direct 3D mapping of hyperspectral data on plant leaves with a reduced AoI bias.

3. Initial results demonstrated accurate mapping of plant vegetation indices (such as normalized difference vegetation index) on the leaves of a plant. These indices are typically used as indicators to monitor plant health. This shows the potential of our approach towards plant phenotyping and remote sensing of vegetation.

4. Beyond remote sensing of vegetation, the proposed approach is also applicable for enhanced material probing of natural targets.

1.4. Relevance to science and economy

The work presented in this thesis primarily contributes to scientific and industrial applications requiring high-precision multi- or hyperspectral distance measurements. The

interdisciplinary nature of this research is relevant across diverse fields, including optical distance metrology, laser scanning, precision measurement and instrumentation, engineering geodesy, remote spectroscopy, and material probing, among other disciplines. This work explores the use of an emerging laser technology that is applicable for hyperspectral distance measurements and may benefit other researchers and technology professionals engaged in related investigations.

Scientific recognition: The content of this thesis is based on four journal publications that are included as the core chapters. Three of these research articles are published and one is currently under review in renowned scientific journals. Apart from the journal publications, two conference proceedings were contributed as oral presentations at recognized scientific conferences. All published articles are (or will be made) openly accessible or their preprints are publicly available online. The data underlying the journal publications is publicly available through the ETH Zurich Research Collection.

In addition to scientific contributions and potential applications highlighted earlier, the investigation into multiwavelength EDM presented herein may open new opportunities for further research into remote inspection of transparent media, such as monitoring atmospheric conditions along the optical path. Scientific research requiring high-precision geometry and remote spectroscopy may benefit from the developed instrumental basis for hyperspectral LiDAR (HSL). Within our institute, the developed HSL setup is actively utilized in project *DeePER* (Deep Phenotyping using LiDAR) to achieve accurate remote mapping of sugar concentration in fruits from the acquired point clouds [35].

Relevance to economy: Applications demanding accurate distance measurements over long ranges that cannot be addressed by alternative solutions such as high-accuracy GNSS will benefit the most from the work presented in this thesis. Examples include alignment of particle accelerators, tunnel surveying, and monitoring small geological changes in mountainous terrain. Furthermore, the research also contributes to hyperspectral laser scanning which is a rapidly growing field. The technology could be integrated into terrestrial laser scanners to achieve highly precise 3D digitization of our environment with hyperspectral signatures. This can be particularly effective in crop health monitoring to predict crop yield or harvest time with greater accuracy; urban planning to optimize topographic mapping and related analyses for more efficient development; non-destructive testing to identify structural defects in industrial or aerospace applications without compromising the structural integrity; and in mining applications where the technology may enhance mineral detection and exploration capabilities.

2 | Background

This chapter introduces the fundamentals and methods pertinent to the core chapters of this thesis. Sec. 2.1 provides a brief overview of the basic principles of traditional electro-optical distance measurement (EDM) techniques and of laser scanning. Sec. 2.2 outlines the influence of refractive index variations on EDM and conventional methods for compensating such refractivity errors. Sec. 2.3 provides an overview of the optical frequency combs and supercontinuum generation, with a focus on their applications in distance metrology.

2.1. Electro-optical distance measurement

EDM technology uses the propagation time of signals superimposed on visible or infrared light for non-contact distance measurement. Conventional EDM instruments typically employ direct time-of-flight (ToF), phase-difference based methods, or a combination of both such as waveform digitization techniques [36]. This section describes the fundamental principles of direct ToF and phase-difference techniques.

Fig. 2.1(a, b) shows a basic schematic representation of both direct ToF and phase-difference methods respectively. In the ToF approach, the amplitude of the light source is either directly or externally modulated using an amplitude modulator (AM) to emit a short optical pulse. The observed optical path length ℓ is directly proportional to the round-trip time delay (Δt) between the transmission and reception of the pulse echo from the target. The geometrical distance D is then estimated as

$$D = \frac{\ell}{n} = \frac{c}{n} \cdot \frac{\Delta t}{2}. \tag{2.1}$$

Here, c is the speed of light in vacuum, and n is the refractive index of air (or of the probed medium if otherwise) at wavelength λ of the light source. As depicted in Fig. 2.1(a), a portion of the emitted light reflects off a beam splitter (BS) and is directed to the photodetector (PD), generating an electrical pulse T_s corresponding to the transmitted optical signal. The reflected pulse is detected by the second PD, to obtain the received signal R_s. Although two photodetectors are shown in this basic schematic, direct ToF can also be done with only one PD i.e. T_s and R_s fed to the same PD. The optical isolator indicated in this schematic is commonly utilized in practice to protect the laser module from the reflected light.

To measure the transit time Δt, a time discriminator is used to generate the trigger signals at the precise instant when the pulses are transmitted or received. Typically, triggers are initiated by factors like the rising edge of the pulse, a pre-defined threshold

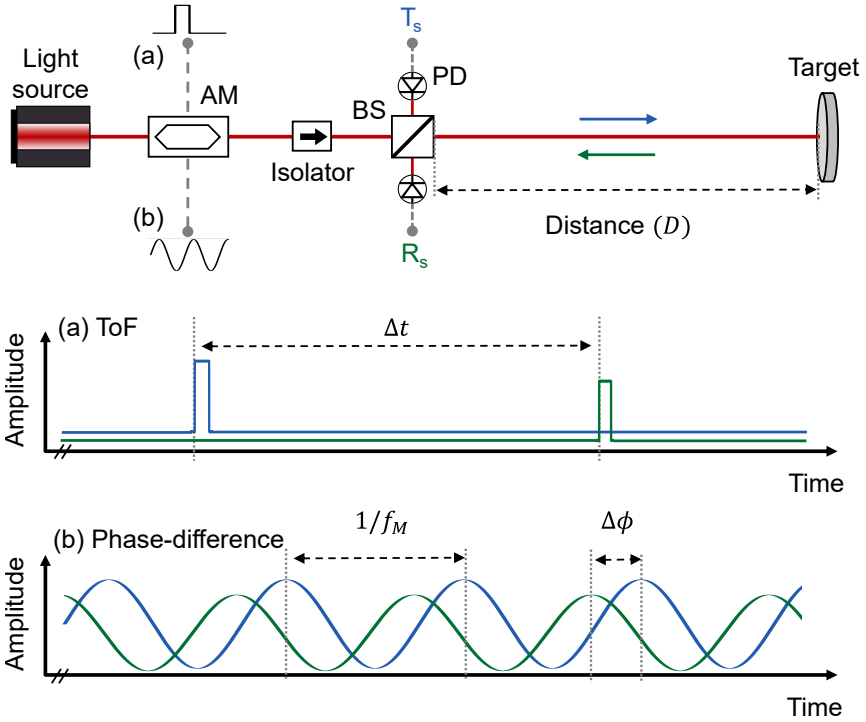

Figure 2.1. Basic schematic representation of the (a) time-of-flight (ToF) and (b) phase-difference approach for distance measurements. (AM: amplitude modulator; BS: beam splitter; PD: photodetector; T_s: transmitted signal; R_s: received signal)

amplitude, or a constant fraction discriminator [3]. Achieving a high temporal accuracy is crucial, as it results in a high spatial accuracy. For example, a temporal accuracy of 1 ns can yield a spatial accuracy of 15 cm. A single transmitted pulse can be received and analyzed to identify multiple reflections, thus allowing us to determine the distances to several targets along a line-of-sight (LoS). The received time traces are usually interpolated to obtain a finer time resolution and consequently derive a better spatial resolution. Averaging over several pulses enhances ranging precision. The inherent sources of uncertainties, such as timing jitter and random walk at the discriminator impact the achievable precision. Direct ToF techniques find utility in applications requiring very long distance measurements, such as satellite or lunar laser ranging, and are also applicable for multi-target ranging along the LoS. Recent advancements in miniaturized optoelectronics have led to the development of compact, affordable, and energy-efficient ToF sensors. These advancements have significantly contributed to the widespread adoption of ToF sensors for proximity sensing in robotics and autonomous vehicles.

In phase-difference techniques, see Fig. 2.1(b), the amplitude of the light source is continuously modulated at a known frequency f_M before its transmission. The geometrical distance (D) is once again estimated from the optical path length (ℓ), where ℓ is now calculated using the accumulated phase difference ($\Delta\phi$) between the transmitted and received signals, expressed as

$$D = \frac{\ell}{n} = \frac{c}{2nf_M}\left(m + \frac{\Delta\phi}{2\pi}\right). \tag{2.2}$$

Here, $c/(2nf_M)$ represents the ambiguity range (or unambiguous distance), and m is an integral number of round-trip ambiguity range cycles. An analog or digital phasemeter determines $\Delta\phi$ through phase measurement techniques like phase-locked-loop (PLL), signal cross-correlation, and in-phase/quadrature (I/Q) demodulation. The heterodyne detection provides narrow bandwidth amplification. This enhances the received signal-to-noise ratio (SNR) and therefore allows for precise estimation of the measured distance. The ambiguity range is inversely related to the modulation frequency f_M. For example, $f_M = 1$ GHz results in an unambiguous distance of approximately 15 cm, while $f_M =$ 100 MHz results in 1.5 m. Although a lower f_M generates a longer unambiguous distance, a higher f_M yields a better range precision (assuming a fixed phase resolution of the phasemeter). Therefore, conventional phase-based EDM instruments typically employ a combination of different modulation frequencies to achieve precise and absolute distance measurements over long ranges [1]. Such instruments find widespread use in engineering surveying and monitoring applications.

Laser scanning: EDM instruments are extended by angle encoders to gather the 3D coordinates of the measured point in space relative to the instrument. This capability is crucial in terrestrial laser scanning of natural surfaces. The technology is also known as scanning light detection and ranging (LiDAR). A deflection or scanning mirror is employed to sweep the light beam across the scanning area, while the LiDAR instrument captures both distance and angular data at multiple points. The acquired data points collectively form a point cloud, representing a 3D digital model of the scanned environment. The angle encoders provide readings to the scanner's two axes of rotation can be derived. For an upright scanner, these angles can be interpreted as zenith distance (ϑ) and horizontal angle (φ). Together with the distance (D) estimated using the traditional distance measurement techniques as described earlier, these polar coordinates can be converted into corresponding Cartesian coordinates (x, y, z) as

$$\begin{pmatrix} x \\ y \\ z \end{pmatrix} = \begin{pmatrix} D \cdot \sin\vartheta \cdot \cos\varphi \\ D \cdot \sin\vartheta \cdot \sin\varphi \\ D \cdot \cos\vartheta \end{pmatrix} \tag{2.3}$$

The acquired data points collectively form a point cloud, representing a 3D digital model of the scanned environment. The digital representation in the form of 3D point clouds finds extensive applications, such as in deformation monitoring, urban planning, cultural heritage preservation, and architectural design. Fig. 2.2 shows a schematic illustration of a terrestrial laser scanner.

The maximum distance that can be measured is primarily determined by the SNR of the received signals. Long-range measurements often involve the use of cooperative targets (retroreflectors) because they reflect a substantial amount of optical energy back to the receiver of the instrument. The maximum measurable range in this case is primarily constrained by the optical energy attenuation along the probe path. In contrast, natural targets diffusely reflect the probe light, resulting in only a portion of the backscattered light being captured by the instrument. In this case, additional factors such as the surface reflectance of the target, angle of incidence, and instrumental factors further influence the measurement SNR.

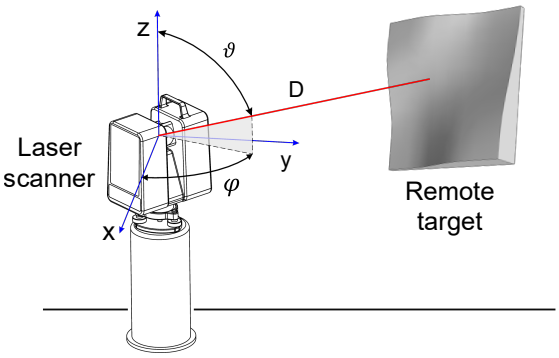

Figure 2.2. Schematic representation of a terrestrial laser scanner (TLS) showing the measured angles and distance coordinates on a remotely placed natural target.

In general, for distance measurements exceeding tens of meters, a laser source is preferred over light-emitting diodes (LED). This is mainly due to the high directionality of the laser source, its peak intensity, longer coherence length, and ease of collimation.

2.2. Influence of refractivity variations

Irrespective of the EDM technique employed, accurately estimating the refractive index of air (n) along the optical path is crucial for determining the geometrical distance accurately (see Eq. 2.1 and 2.2). As mentioned earlier, for long-distance measurements on cooperative targets, the practically attainable accuracy is limited by the insufficient knowledge of n along the measurement path. The functional relation of n with λ and the meteorological parameters is described through the empirical equations [8, 10, 11] established in the literature.

2.2.1. Empirical equations

Primarily, the modified Edlén equations [9] or Ciddor's equations [10, 11] are used in practice to determine n. The modified Edlén equations are derived from accurate measurements of the refractive index using an air refractometer. These measurements were conducted for both dry and moist air conditions across various wavelengths distributed over the visible and infrared spectrum. The general form of this equation, as shown by [37] is represented as

$$n_p(\lambda, T, P, p_w, x_c) - 1 = K(\lambda) \cdot S(T, P, x_c) - p_w \cdot g(\lambda), \tag{2.4}$$

where, n_p is the phase refractive index of air, $(n-1)$ is a general expression for refractivity. The term n_p is expressed as a function of the optical wavelength (λ), temperature (T), pressure (P), partial pressure of water vapor (p_w), and carbon dioxide content (x_c). The group refractive index (n_g) is calculated as $n_g = n_p - \lambda \cdot dn_p/d\lambda$. The terms K and g rely only the optical wavelength λ and are expressed as

$$K(\lambda) = 10^{-8} \times \Big(8091.37 + \frac{2333983}{130 - 1/(\lambda/\mu\text{m})^2} + \frac{15518}{38.9 - (\lambda/\mu\text{m})^2}\Big),$$
$$g(\lambda) = 10^{-10} \times \big(3.802 - 0.0384/(\lambda/\mu\text{m})^2\big),$$

and the term S accounts for the meteorological parameters T, P, x_c.

$$S(T, P, x_c) = \frac{P/\text{Pa}}{932164.60} \times \frac{1 + 10^{-8}(0.5953 - 0.009876\ T/^\circ\text{C})\ P/\text{Pa}}{1 + 0.0036610\ T/^\circ\text{C}} \times \big(1 + 0.5327(x_c - 0.0004)\big).$$

To estimate p_w, the relative humidity $RH\%$ (which can be measured using standard hygrometers) and the air temperature have to be known. Considering $T_K = 273.15 + T/^\circ\text{C}$ where T_K is the air temperature in Kelvin, p_w is calculated as

$$p_w/\text{Pa} = \frac{RH}{100} \cdot e^{aT_K^2 + bT_K + c + d/T_K}, \tag{2.5}$$

with

$$a = 1.2378847 \times 10^{-5}/\ \text{K}^2, \quad b = -0.019121316/\ \text{K},$$
$$c = 33.93711047, \quad d = -6343.1645\ \text{K}.$$

Ciddor's equations [10, 11] were formulated as part of a working group of the International Association of Geodesy (IAG) and were accepted as a standard for calculating the refractive index of air. They were developed to accommodate a broader range of atmospheric conditions and wavelengths compared to Edlén's equation. The general expression of Ciddor's equations to calculate the phase refractive index (n_p) is

$$n_p(\lambda, T, P, p_w, x_c) - 1 = \frac{\rho_a(T, P, x_c)}{\rho_{\text{axs}}(x_c)}\Big(n_{\text{axs}}(\lambda, x_c) - 1\Big) + \frac{\rho_w(T, P, p_w)}{\rho_{\text{ws}}(p_w)}\Big(n_{\text{ws}}(\lambda, p_w) - 1\Big), \tag{2.6}$$

where ρ_a is the density of dry air (humidity=0%) at current atmospheric conditions, ρ_{axs} is the density of standard dry air at 15°C, 1013.25 hPa with x_c ppm of CO_2, and n_{axs} is the refractive index of standard dry air at λ. In the second term, ρ_w is the density of water vapor at current atmospheric conditions, ρ_{ws} and n_{ws} are the density and refractive index of water vapor respectively, at 20°C and 13.33 hPa. The complete set of equations for computing the phase and group refractive index can be found in [10, 11] respectively.

A recent correction to the analytical expression of Ciddor's equation was made to rectify a sign error [38]. This correction accounted for a relative error of approximately 2 ppm in n_g at around 1560 nm (which is the typically used wavelength in commercial EDM instruments). Nevertheless, the inherent uncertainty of Ciddor's and Edlén's equations is on the order of 10^{-8}, and therefore both of these equations are used in practical applications.

The phase refractive index (n_p) is employed to estimate distances from interferometric measurements. Established commercial instruments, such as total stations or laser scanners utilize intensity-modulated lasers that in practice have a certain bandwidth. Therefore, they use the group refractive index (n_g) for computing the distance. Since our

approach for distance measurements involves a non-interferometric technique, we also use n_g to estimate the distances from the optical path length. We will primarily consider using n_g throughout this thesis. However, the general concepts discussed in this chapter also apply to the phase refractive index of air. Fig. 2.3 shows the dispersion profile of air calculated using the corrected Ciddor equations (as provided in [38]) considering the typical values of the meteorological parameters in our laboratory (where, $T \approx 20°C$, $P \approx 960$ hPa, $RH \approx 50\%$, and $x_c \approx 440$ ppm). It can be observed that the gradient of the refractivity is steeper in the shorter wavelength region of the visible spectrum as compared to the infrared spectrum.

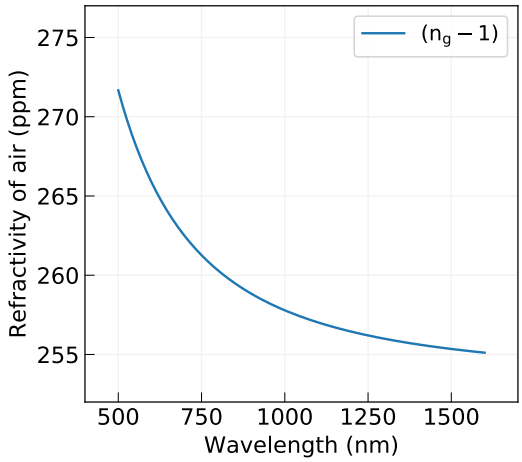

Figure 2.3. Group refractivity in air $(n_g - 1)$ as a function of the optical wavelength from 500 to 1600 nm. The values are calculated using Ciddor's equation from [13] for $T = 20°C$, $P = 960$ hPa, $RH = 50\%$ and $x_c = 410$ ppm.

2.2.2. Refractivity errors

The empirical equations presented in Sec. 2.2.1 highlight that n is influenced by variations in the meteorological parameters. Given that the measured optical path length is $\ell = n{\cdot}D$, where D is the true geometrical distance to the target, any deviation in n can result in distance errors. Table 2.1 shows the impact of the different meteorological parameters on the refractive index, calculated at $\lambda_1 = 780$ nm and $\lambda_2 = 1560$ nm in the near-infrared. The initial meteorological values are the same as shown earlier in Fig. 2.3. The chosen wavelengths (λ_1, λ_2) are quasi-randomly selected; they represent the typical wavelength used in commercial EDM instruments (i.e. around 1550 or 1560 nm, which is also used in fiber optic communication due to lower attenuation of optical fibers around this wavelength) and its frequency-doubled component i.e., 780 nm for comparison.

Table 2.1 indicates that the relative impact of variations in T and P are significantly larger compared to variations in RH and x_c. Considering the spatial and temporal variations of the meteorological parameters in practical EDM, the impact of variations in RH and x_c are often neglected as compared to T and P. Moreover, changes in T and P have a slightly higher impact near the visible part of the spectrum as compared to longer wavelengths in the near-infrared region. The corresponding distance errors can

Table 2.1. Impact of changes in the meteorological parameters $\mathcal{X}$ on the group refractive index n_g of air, calculated at $\lambda_1 = 780$ nm and $\lambda_2 = 1560$ nm with initial meteorological parameters $T = 20°\text{C}$, $P = 960$ hPa, $RH = 50\%$ and $x_c = 410$ ppm.

$\mathcal{X}$	$\Delta\mathcal{X}$	$\Delta n_{g,\lambda_1}$	$\Delta n_{g,\lambda_2}$
T	1°C	-9.1×10^{-7}	-8.9×10^{-7}
P	1 hPa	2.7×10^{-7}	2.6×10^{-7}
RH	1%	-8.2×10^{-9}	-8.6×10^{-9}
x_c	1 ppm	13.7×10^{-11}	13.4×10^{-11}

be computed from the errors in n. For example, $\Delta T = 1°\text{C}$ or $\Delta P = 4$ hPa results in distance deviations of around 1 ppm. This implies that a variation of 1°C along the LoS would introduce a distance error of around 1 mm over 1 km.

In general, the achievable measurement accuracy is practically constrained by the spatial and temporal variability of n along the probe path. The standard approach to account for refractivity in EDM involves recording the meteorological parameters with sufficient temporal resolution at a few locations along the probe path. Usually, the meteorological data is acquired near the instrument and, occasionally at the other end (near the reflecting target) if a higher level of accuracy is necessary. The meteorological corrections are then calculated using a forward modeling approach. However, accurately determining the integral value of n along the entire probe path based on a limited number of meteorological measurements is challenging. Even with a dense set of meteorological observations, such as every 10 m along a path of 600 m, achieving distance corrections below the ppm level has proved practically challenging [13]. This difficulty arises from local variations and temporal changes in the spatial distribution of n, coupled with inherent uncertainties in the meteorological observations.

2.2.3. Dispersion-based refractivity correction

An alternative method for refractivity correction relies on atmospheric dispersion and uses simultaneous distance measurements on two or more wavelengths. The approach of using two wavelengths was proposed in the early 1960s [14], and is commonly known as the two-color method. This method enables estimating the integral impact of the refractive index along the probe path and correcting its effect on the measured distances, and is robust against spatial and temporal fluctuations. The observed path lengths (ℓ_1, ℓ_2) on two wavelengths (λ_1, λ_2) can be expressed as $\ell_1 = n_1 \cdot D$ and $\ell_2 = n_2 \cdot D$, where D is the true geometrical distance to the target. The differences in the observed optical path lengths originate from the effective refractive indices (n_1, n_2) at these wavelengths under specific atmospheric conditions. According to the two-color method, the refraction compensated geometrical distance $\hat{D}$ can be estimated from the observations ℓ_1, ℓ_2 as

$$\hat{D} = \ell_1 - A \cdot (\ell_2 - \ell_1). \tag{2.7}$$

Here, $A = (n_1 - 1)/(n_2 - n_1)$ and is typically referred to as the A-factor. Using the general form of the Edlén equations (see Eq. 2.4), the coefficient A can be written as

$$\begin{aligned} A &= \frac{n(\lambda_1, T, P, p_w, x_c) - 1}{n(\lambda_2, T, P, p_w, x_c) - n(\lambda_1, T, P, p_w, x_c)} \\ &= \frac{K(\lambda_1) \cdot S(T, P, x_c) - p_w \cdot g(\lambda_1)}{\big(K(\lambda_2) \cdot S(T, P, x_c) - p_w \cdot g(\lambda_2)\big) - \big(K(\lambda_1) \cdot S(T, P, x_c) - p_w \cdot g(\lambda_1)\big)}. \end{aligned} \tag{2.8}$$

For dry-air, $RH = 0\%$ and thus $p_w = 0$ Pa (from Eq. 2.5). This results in

$$A = \frac{K(\lambda_1) \cdot S(T, P, x_c)}{K(\lambda_2) \cdot S(T, P, x_c) - K(\lambda_1) \cdot S(T, P, x_c)} = \frac{K(\lambda_1)}{K(\lambda_2) - K(\lambda_1)} \tag{2.9}$$

Eq. 2.9 implies that for dry-air, the A-factor is only a function of the two wavelengths [37]. Hence, under dry-air conditions, the two-color method is independent of any external meteorological parameter.

Table 2.2. Approximate deviations in the optical path length (ℓ_λ), the $|A|$-factor, and the estimated $\hat{D}$ from the two-color method, corresponding to the variations in the meteorological parameters $\mathcal{X}$ i.e (T, P, RH). The impact of Δx_c is negligible and hence not shown here. The 780/1560 nm wavelength pair (λ_1, λ_2) with initial meteorological parameters $T = 20$°C, $P = 960$ hPa, and $x_c = 410$ ppm are used for the calculations.

RH	$\Delta\mathcal{X}$	$\Delta\ell_1$ **(ppm)**	$\Delta\lvert A\rvert$	$\Delta\hat{D}$ **(ppm)**
0%	1°C	-8.8×10^{-1}	$\approx 10^{-11}$	$\approx -10^{-10}$
	1 hpa	2.7×10^{-1}	$\approx 10^{-12}$	$\approx 10^{-11}$
	1%	-8.3×10^{-3}	0.4×10^{-2}	-0.2×10^{-1}
50%	1°C	-9.1×10^{-1}	0.1×10^{-1}	-0.8×10^{-1}
	1 hpa	2.7×10^{-1}	0.2×10^{-3}	0.1×10^{-2}
	1%	-8.2×10^{-3}	0.4×10^{-2}	-0.2×10^{-1}
99%	1°C	-9.3×10^{-1}	0.3×10^{-1}	-1.6×10^{-1}
	1 hpa	2.7×10^{-1}	0.4×10^{-3}	0.2×10^{-2}
	1%	-8.1×10^{-3}	0.4×10^{-2}	-0.2×10^{-1}

However, the main drawback of this approach is that the distance uncertainty of $(\ell_2 - \ell_1)$ is scaled by A, leading to increased uncertainty in the estimated geometrical distance $\hat{D}$ as $|A| > 1$. Therefore it is necessary to select a wavelength pair (λ_1, λ_2) such that the value of A is relatively low. This requires the wavelengths λ_1 and λ_2 to be widely separated from each other in the spectral domain, preferably also exploiting the steeper dispersion gradient in the visible part of the spectrum. This leads to a larger value in the denominator of Eq. 2.9 and consequently a lower value of A. Values of $A > 20$ (for group refractive indices) can be expected if both the wavelengths are between 550 and 1600 nm. For example, using a 1560/780 nm wavelength pair results in $|A| = 48$ for dry air. This suggests that if the uncertainty of $(\ell_2 - \ell_1)$ is approximately equal to 1 µm, then the achieved uncertainty of $\hat{D}$ will be around 48 µm. Therefore, the dispersion-based refractivity correction approach also requires highly precise measurements of the individual optical path lengths.

Another limitation of the two-color method is its applicability only to dry-air. In practical outdoor conditions, typically $RH > 0\%$ and the terms $S(T, P, x_c)$ and $p_w \cdot g(\lambda)$ in Eq. 2.7 do not cancel. Therefore, the dependency on the meteorological parameters persists. Tab. 2.2 shows the corresponding variations in ℓ, A, and $\hat{D}$ for both dry and wet air conditions along with their meteorological impact. Tab. 2.2 indicates that the influence of changes in RH on $\hat{D}$ is approximately 3 times higher than on the individual observations ℓ (for any absolute value of RH). A variation of $\Delta RH = 100\%$ leads to a relative error of about 2 ppm on $\hat{D}$ when $T \leq 20°\text{C}$ and even more at higher temperatures. Nevertheless, a relative uncertainty better than 0.1 ppm on $\hat{D}$ can be achieved if RH is monitored with a measurement uncertainty below 4%. For many applications, the changes in RH thus persist but moderately affect the two-color method or even negligible degradation of the accuracy as compared to dry air. Therefore, the method remains useful for practical applications.

Multi-color method: Theoretically, using more than two wavelengths can mitigate the impact of RH. A three-color method has already been demonstrated in the literature [15]. However, in the visible and near-infrared wavelengths, the scaling factor of the measurement uncertainties is on the order of 10^3. This requires a nm level or better optical path length differences to achieve a ppm level refraction correction using the three-color method. Recently, a multi-color approach was proposed using > 3 wavelengths and was experimentally demonstrated through measurements on 4 wavelengths using dispersive interferometry [16]. The theoretical formulation of the multi-color approach [16] derived from the modified Edlén equations [9] is expressed as

$$\begin{bmatrix} 1 & K_1 & -g_1 \\ 1 & K_2 & -g_2 \\ \vdots & \vdots & \vdots \\ 1 & K_m & -g_m \end{bmatrix} \begin{bmatrix} \hat{D} \\ \hat{D} \cdot S \\ \hat{D} \cdot p_w \end{bmatrix} = \begin{bmatrix} \ell_1 \\ \ell_2 \\ \vdots \\ \ell_m \end{bmatrix}, \tag{2.10}$$

where m is the number of wavelengths used for the distance measurements. Considering $\mathbf{B}$ as the first matrix with the K and g terms, $\hat{D}$ is estimated as

$$\hat{D} = \sum_{i=1}^{m} (\mathbf{B}_i^{\mathbf{T}} \mathbf{B}_i)^{-1} \mathbf{B}_i^{\mathbf{T}} \cdot \ell_i. \tag{2.11}$$

where $^{\mathbf{T}}$ denotes matrix transpose. This method also requires sub-µm to nm level precision to benefit from multi-color refraction compensation. Nevertheless, the two-color or multi-color method provides solutions for inline refractivity compensation without relying on external meteorological observations, thus making it useful for achieving accurate measurements over long distances.

Few early experimental developments: The first demonstration of inline refractivity compensation was reported in 1967 using the two-color method [17]. The authors developed a laboratory setup employing a He-Ne laser (633 nm) and a filtered broadband source at 368 nm. A more portable version of this design, substituting the blue lamp at 368 nm with a He-Cd laser at 442 nm, was introduced in 1972 [39]. The measurement principle utilized a phase-based EDM approach by indirectly modulating the intensity

through a polarization modulator. The improved platform underwent further tests in varying atmospheric conditions on a 5.9 km long path, thereby marking the first practical demonstration of the two-color method.

In subsequent developments, an additional RF link at 9.6 GHz was introduced to obtain an extra range difference between the optical and microwave regions [40]. The objective was to eliminate the reliance on atmospheric pressure and water vapor partial pressure. A few years later, the feasibility of using the two-color method in direct ToF measurements was investigated by using high-power pulsed laser sources [41]. The goal was to show refractivity compensation over longer distances. To achieve this, the authors utilized the first and second harmonics of a Q-switched ruby laser with a power density of 50 MW/cm^2, along with fast photomultipliers and counting circuity. This approach showed that two-wavelength pulsed laser telemeters can reach 1 ppm accuracies for distances exceeding a few kilometers.

In 1981, the first two-color commercial instrument, Terrameter, was introduced [19]. Its experimental design closely resembled that of [40], however without the RF measurement. The authors incorporated a He-Cd and He-Ne laser source for the two-color EDM. To mitigate potential frequency-related errors, a Rb-frequency standard served as a reference for the counters measuring the distance-dependent modulation frequency. The measurements required the initial end-point observations of the meteorological parameters and a coarse distance value to solve the half-wavelength ambiguity range. The instrument claimed an accuracy of about 0.1 ppm with good visibility over a measurement range of up to 15 km. However, extensive efforts were required to adapt the instrument at each location, requiring constant specialized engineering supervision during its operation [20].

Although a theoretical solution for the three-color approach was proposed in 1997 [15], there was no subsequent experimental demonstration of the technique in the following years. This may have been due to the availability of high-accuracy GNSS at that time, which offered a cost-effective and accurate distance measurement over extended ranges. However, as mentioned earlier in Sec. 1.4, there are open applications requiring highly accurate distance measurements, particularly where GNSS-based solutions are not applicable. In recent years, with the discovery of frequency comb (FC) technology, there has been a growing interest in exploiting the FC technology for high-precision distance measurements over long distances and for conducting refraction-corrected distance measurements using two-color FC sources.

2.3. Coherent supercontinuum

This section provides an overview of optical frequency comb technology and the generation of supercontinuum laser sources from such frequency combs. It also outlines the applications of frequency combs and supercontinuum, primarily focusing on their relevance to distance measurements.

2.3.1. Optical frequency comb

Optical frequency comb (FC) represents a spectrum consisting of a series of stable, narrow linewidth, and equally spaced frequency lines [27]. The technology was developed more than 20 years ago, utilizing a phase-stabilized mode-locked laser (MLL). The MLL generates ultrashort optical pulses, typically in the femto- or picosecond time scale, which is achieved through the coherent addition of hundreds of thousands to millions of resonant longitudinal optical cavity modes [42, 43]. The temporal width of the emitted pulse (t_p) is inversely related to the cavity gain bandwidth (G_B) of the laser. For instance, if $G_B = 10$ THz, then $t_p = 100$ fs. In the time domain, the laser emits a train of optical pulses, each separated by a specific pulse period (T_r) which is determined by the round-trip time of the pulses within the laser cavity. This temporal pattern translates to a series of frequency lines in the Fourier spectrum resembling a comb structure, and hence the term *frequency comb*. Fig. 2.4 illustrates the time and frequency domain representation of a phase-stabilized mode-locked femtosecond laser, also commonly known as a frequency comb (FC).

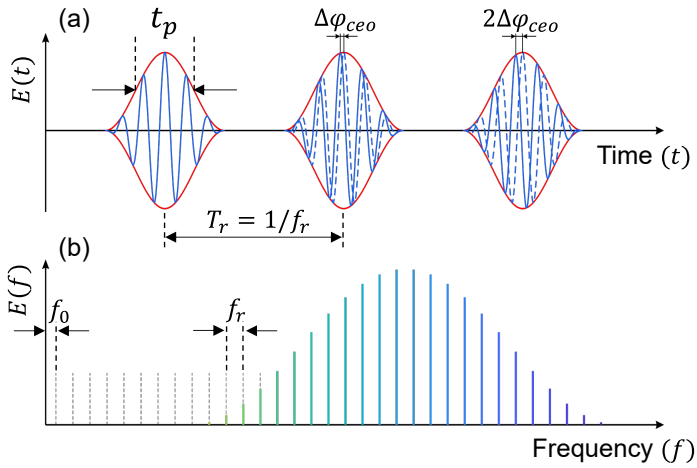

Figure 2.4. Schematic representation of the (a) time and (b) frequency domain response of an optical frequency comb. The pulse width t_p, pulse-repetition rate $f_r = 1/T_r$, carrier offset frequency f_o and the carrier-envelope phase offset $\Delta\varphi_{ceo}$ are also indicated in the figure.

The term $\Delta\varphi_{ceo}$ represents the carrier-envelope phase offset, indicating the phase difference between the carrier wave and its envelope. The offset frequency f_0 is related to the carrier-envelope phase offset as $f_0 = (1/2\pi) \cdot (\Delta\varphi_{ceo} \cdot f_r)$. This f_0 can vary between zero and f_r. The electric field $E(t)$ of the optical carrier modulated by a periodic pulse envelope $X(t)$ can be expressed as

$$E(t) = X(t) \cdot e^{i2\pi f_c t} = \sum_{N=N_1}^{N_2} X_N \cdot e^{i2\pi f_N t}. \tag{2.12}$$

Here, f_c is the carrier-frequency, f_N denotes the Fourier series having an amplitude of X_N for mode number N which is an integer number between 10^5 to 10^6 [43]. The pulse-to-pulse period $T_r = 2L/v_g$, where L is the length of the optical cavity, and v_g is the pulse group velocity in the cavity. The T_r is also inversely related to the pulse repetition

frequency (f_r), i.e. $T_r = 1/f_r$. The comb lines in the frequency domain are defined as

$$f_N = N \cdot f_r + f_0. \tag{2.13}$$

Eq. 2.13 is also referred to as the comb equation. Although, f_r is known and fixed by the cavity length, to obtain absolute frequency references it is essential to determine the value of f_0. This is generally accomplished via self-referencing of an octave-spanning comb spectrum [43] typically achieved through coherent broadening of the comb i.e.

$$f_0 = 2 \cdot f_N - f_{2N}. \tag{2.14}$$

Due to the limited bandwidth (BW) of photodetectors (PD) which is typically on the order of a few GHz, they lack the speed to directly observe the optical frequencies. When a FC is fed to a PD, the adjacent optical comb lines beat with each other, generating electrical beat note frequencies within the BW of the PD. The process is generally known as intermode beating, and the resulting electrical beat notes are called intermode beats. These electrical beat notes constitute a series of stable, evenly spaced radio frequencies, each separated by f_r. This capability of accurately transferring optical frequencies in the hundreds of THz range to radio frequencies in the GHz is what makes the FC an interesting tool for precision metrology applications [29]. Over the recent years, FC-based measurement techniques have shown remarkable developments in the field of frequency metrology [42], optical atomic clocks [44], ultra-low noise microwave generation [45], astrocombs [46], precision spectroscopy [47] and distance metrology [48].

Supercontinuum generation: An optical supercontinuum (SC) is generated by spectrally broadening such ultrashort pulses using a highly nonlinear medium. A conventional method to coherently broaden the FC source is by transmitting it through a photonic crystal fiber (PCF) or microstructured optical fiber [49, 50]. These fibers typically feature a periodic arrangement of air holes or channels along their length [51]. The primary advantage of such coherent SC sources is the expanded spectral distribution spanning several hundred nm while maintaining the inherent comb line spacing between each optical mode. For instance, considering $G_B = 10$ THz (as in the example earlier) and $f_r = 100$ MHz of the laser cavity, a 780 nm FC source would exhibit a linewidth of around 20 nm. Although this exceeds the typical linewidth of a single-wavelength laser source, it is still insufficient for multiwavelength refractivity-compensated EDM which requires the two wavelengths far separated from each other (see. Sec. 2.2.3). Therefore, multiple FC sources centered at different wavelengths are necessary. In contrast, assuming a nominal spectral broadening of around 20 times, the SC generated from FC would span over 400 nm while maintaining the same comb spacing, i.e. $f_r = 100$ MHz. The broadband spectral range allows the flexibility in selecting any wavelengths or a range of wavelengths from a single source. This characteristic of the SC is particularly valuable for refractivity-compensated multiwavelength EDM and also for hyperspectral LiDAR as previously mentioned, which is further explored in the research presented herein. While hyperspectral LiDAR utilizes the entire output spectrum, multiwavelength refractivity-corrected EDM typically only utilizes a limited number of spectral bands, often just two. Consequently, refractivity correction through SC-based multiwavelength EDM results in

the inefficient utilization of most of the optical energy, although offering the advantage of flexibly selecting the spectral bands.

However, SC generated from microstructured optical fibers or PCF exhibits a low-frequency and broadband noise component [52]. The low-frequency component primarily arises from the laser power and beam-pointing instability at the fiber input, whereas the broadband component results from the intrinsic quantum noise sources. Therefore the phase noise of the optical comb lines in SC is slightly larger than its seed FC source. These intrinsic errors constitute the basic limitations of using a SC for distance measurements compared to a stabilized FC.

2.3.2. Distance measurement using frequency combs

The application of FC for distance measurements was first proposed nearly two decades ago by using the intermode beats of a mode-locked fs laser [53]. Experiments were conducted in a 240 m tunnel using two FCs centered at 1560 and 780 nm. An accuracy of around 50 µm was achieved using phase measurements at the 1 GHz beat note on a cooperative target. Subsequently, the authors demonstrated an accuracy of 14 µm using a higher-order 10 GHz beat note on a similar setup [54]. A portable design of the setup was also tested in open-air conditions [55], reporting a measurement uncertainty on the order of 0.1 ppm up to a distance of 318 m, which was primarily affected by the air turbulence.

Since then various other techniques, such as those based on interferometry [56, 57, 58], time-of-flight [59], and dual-combs [60, 61] are demonstrated. These techniques showcase the feasibility of achieving high measurement precision (on the order nm to a few µm) and sub-mm to mm level accuracy over ranges from several hundred meters to a few km on cooperative targets. Two-color solutions using FC have also been reported in the literature [62, 63, 64, 65, 66, 67], demonstrating effective refractivity compensation. Additionally, the use of this technology for measurements on natural surfaces was also reported recently in the literature [68, 69, 70].

In this study, we employ the intermode beating approach for distance measurements. The non-interferometric nature of the intermode beating approach, characterized by less stringent coherency requirements compared to interferometric methods, makes it robust against complex atmospheric conditions. The approach has the potential to enable accurate measurements over longer ranges [28, 71]. The existing literature on the FC-based intermode beating approach has demonstrated deviations smaller than 10 µm over distances up to 100 m when compared with a reference interferometer [28]. Very recently, distance measurement using a dynamic FC was also reported [72]. The authors proposed using the slope of the intermode beat phase by sweeping the repetition frequency of the comb. This could theoretically achieve an infinite non-ambiguous range. Experimental results showed errors within 25 µm at 65 m in the laboratory and within 100 µm at 219 m outdoors. These findings highlight the potential of distance measurements using intermode beats as a promising alternative to established EDM approaches. However, there is a lack of detailed investigations on distance measurements using the intermode beats obtained from a SC, which forms the core contribution of this thesis.

A parallel experimental investigation conducted within our institute has recently demonstrated the utility of SC for material classification through spectrally-resolved delay and power measurements at multiple wavelengths [73]. Additionally, polarized reflectance signatures of natural surfaces have proven to be valuable for classifying material roughness [74].

Subsequent chapters in this thesis present investigations on high-precision distance measurements utilizing the intermode beats obtained from a SC. Chapters 3–4 demonstrate how distance measurements on spectral bands filtered from the SC enable inline refraction correction. Fig. 2.5 illustrates the optical part of the experimental setup designed for two-color inline refraction correction described in Chapter 4.

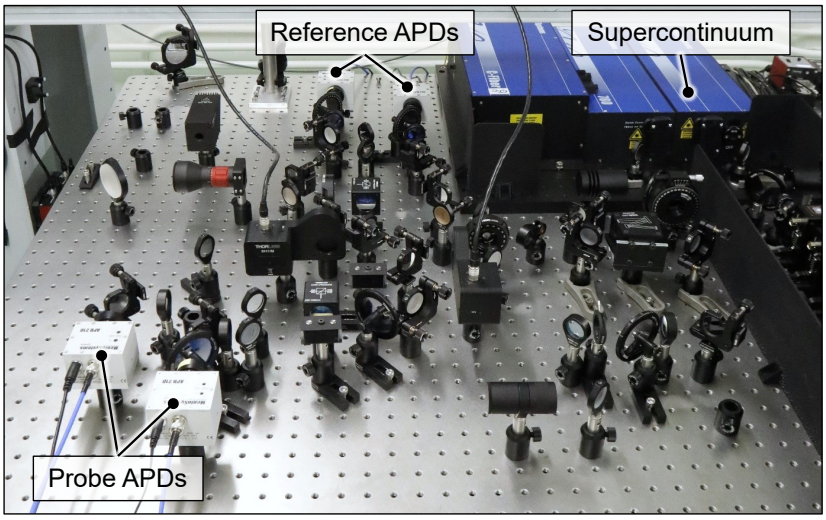

Figure 2.5. A picture of the optical setup developed for the experiments on two-color inline refraction correction. The optical table has a mounting hole spacing of an inch.

Additionally, the chapters 5–6 demonstrate SC-based hyperspectral LiDAR for precision laser scanning. In this case, the whole SC output is used for ranging while the backscattered spectral information from the target is captured across the entire SC output, thereby providing precise geometric information along with the spectral data mapped onto each scanned point. Fig. 5.11(a) in Chapter 5 shows a picture of the scanning module developed for hyperspectral laser scanning.

3 High-precision intermode beating electro-optic distance measurement for mitigation of atmospheric delays

Pabitro Ray, David Salido-Monzú, and Andreas Wieser
Journal of Applied Geodesy, 17(2), pp. 93-101, 2023
doi: 10.1515/jag-2022-0039

(Author version; for typeset version please refer to the original paper)

Abstract

High-precision electro-optic distance measurement (EDM) is essential for deformation monitoring. Although sub-ppm instrumental accuracy is already feasible with state-of-the-art commercial technology, the practically attainable accuracy on distances over more than a few hundred meters is limited by uncertainties in estimating the integral refractive index along the propagation path, which often results in measurement errors of several ppm. This paper presents a new instrumental basis for high-accuracy multispectral EDM using an optical supercontinuum to enable dispersion-based inline refractivity compensation. Initial experiments performed on two spectrally filtered bands of 590 and 890 nm from the supercontinuum show measurement precision better than 0.05 mm over 50 m for an acquisition time of around 3 ms on the individual bands. This represents a comparable performance to our previously reported results on 5 cm by over a range of 3 orders of magnitude longer, which can still be improved by increasing the acquisition time. The preliminary results indicate a relative accuracy of about 0.1 mm at 50 m on each wavelength. Improvement is possible by calibration and by implementing a self-reference scheme that mitigates slow drifts caused by power-to-phase coupling. The results reported herein thus indicate that the presented approach can be further developed for achieving sub-ppm accuracy of refractivity compensated distance measurements on practically useful ranges and under outdoor conditions.

3.1. Introduction

High-precision electro-optic distance measurement (EDM) technology is a key element for a variety of applications such as surveying, industrial metrology, and deformation monitoring of large-scale structures [1]. The technology has enabled non-contact measurements over distances from a few mm to several km with sub-mm-level instrumental precision. However, for long-distance EDM (distances $>$ 100 m), the measurement accuracy under practical conditions is limited by the uncertainties of the refractive index (n) of the air. Errors result from insufficient knowledge of the atmospheric conditions and thus of n along the optical path. This restricts the accuracy of long-distance EDM to 1 ppm or worse with commercial instruments [12]. For standard air and EDM using optical wavelengths, primarily spatial and temporal variations of temperature (T) and pressure (P) cause refractivity errors. E.g., a deviation of 1 K in temperature or 4 hPa in pressure leads to a distance deviation of 1 ppm. Relative humidity (RH) and CO_2 concentration (X_c) have a much smaller impact.

Conventionally, such refractivity-induced errors are mitigated by forward modeling using meteorological parameters measured at a few locations (often only at the instrument location) and estimating the refractive index using empirical equations such as Ciddor's equations [10, 11] or Edlen's updated equations [9]. The accuracy of these empirical equations is on the order of 10^{-8}, representing the best achievable performance for distance measurements in standard air [65]. While this method works well for relatively short distances, discrete sets of meteorological observations typically fail to represent the true spatial distribution of refractivity along the optical path over longer distances. Recent research has shown that even taking a dense set of meteorological measurements along the entire path (e.g., simultaneously every 10 m along a 600 m line-of-sight), achieving distance corrections below the ppm level is exceptionally challenging under practical outdoor conditions with forward modeling [13]. Therefore, achieving high accuracy EDM over long distances requires employing a method capable of self-correcting for refractivity errors, thereby alleviating the necessity to estimate the refractivity from meteorological parameters.

Dual-wavelength compensation (traditionally referred to as the two-color method) is a well-known technique that allows self-correction of refractivity variations using simultaneously acquired distance measurements obtained using optical radiation at two different wavelengths [14]. The technique achieves inline refractivity compensation through the differential delay caused by dispersion. The first experimental demonstration of dual-wavelength compensation was presented over 50 years ago using a He-Ne laser at 632.8 nm and light at 368.1 nm filtered from a mercury arc lamp [17]. Based on the same principle, the commercial instrument Terrameter was later conceived using a He-Ne (633 nm) and a He-Cd (440 nm) laser [19]. However, limitations imposed by the technical challenges of the setup made this commercial realization impractical, and the necessary fractional stability ($\Delta f/f$) of the laser frequency (f) prevented the achievable accuracy from getting close to the accuracy level of the empirical equations.

In recent years, with the discovery of frequency combs [75], the fractional stability of the laser frequency has improved to the precision levels of a Rubidium (Rb) atomic clock, i.e., $\Delta f/f \approx 10^{-11}$ or even better [66]. This significant improvement, along with

concurrent advances in spectral manipulation technologies and high-frequency/low-noise electronic instrumentation [29], has provided a foundation for pushing EDM accuracy further.

Following the pioneering work by [53] on EDM using a frequency comb derived from a mode-locked femtosecond (fs) laser, numerous investigations have continually improved the state-of-the-art of precision distance metrology [27, 60, 28]. Inline refractivity-compensated EDM using dual-wavelength frequency combs has been reported [63, 65, 66, 76]. However, in general, two fixed-wavelength combs are used (usually around the standard telecommunication wavelength of around 1560 nm and its frequency multiplied components, e.g., 780 nm), which restricts the possible spectral combinations and requires co-aligning of different beams.

In this work, we use a 420 nm wide supercontinuum (SC) coherently broadened from a 780 nm mode-locked fs laser. The broad spectral range of the SC, ranging from 580 to 1000 nm, allows more flexibility in selecting the optimal combination of wavelengths, possibly even more than two from the entire span of the spectrum. Additionally, compared to the traditional comb sources, the SC offers increased flexibility in gathering power and phase signatures over a wide range of available wavelengths, representing a suitable source to enable dispersion-based inline refractivity compensation through multiwavelength EDM. The experimental feasibility of this approach has been previously demonstrated over very short distances of only about 5 cm [31]. In this paper, we extend the previous work by demonstrating SC-based dual-wavelength EDM over 50 m, i.e. increasing the distance by 3 orders of magnitude. The experimental platform is already designed such as to be later adaptable for distances again longer by 1-2 orders of magnitude and thus for surveying and monitoring applications.

The remainder of the paper is organized as follows: we give a brief introduction to the dual-wavelength method and describe intermode beating. We then explain the experimental setup and results for dual-wavelength measurements over 50 m. Finally, we summarize and conclude with key areas to be investigated for improving the present performance.

3.2. Approach

3.2.1. Dual-wavelength method

The atmosphere is dispersive for optical waves, i.e. the refractivity depends on the wavelength. Fig. 3.1 shows this for the group refractivity $(n_g - 1)$ and wavelengths between 400 and 1600 nm.

By exploiting dispersion, the true geometrical distance (D) can be determined from simultaneous distance measurements, i.e. measurements of the optical path length (L_1, L_2) on two wavelengths (λ_1, λ_2) as

$$D = L_1 - A(L_2 - L_1) \tag{3.1}$$

where $A = (n_1 - 1)/(n_2 - n_1)$ is the dispersion-coefficient; n_i is the average refractive

index of air along the measurement path at the wavelength λ_i and the optical path length is related to the true length by $L_i = n_i D$. In the case of dry air, A is very weakly dependent on the environmental parameters and can be assumed constant under practical conditions. E.g. for the set of parameters in Fig. 3.1 with $RH = 0\%$ and any wavelength pair in the range from 400 to 1600 nm, changes of $\Delta T = 10$ K or $\Delta P = 40$ hPa introduce relative changes of around 2 ppm in A, causing negligible relative errors of the estimated distance (below 10^{-9}). For wet air with $RH = 50\%$, the dependence of A on T and P increases, and the same changes in $\Delta T = 10$ K or $\Delta P = 40$ hPa introduce relative distance errors of around 1 ppm and 0.05 ppm respectively. The impact of ΔX_c on relative distance errors can be neglected. However, the dependence of A on RH is also relevant. E.g., for the set of parameters in Fig. 3.1 and any wavelength pair in the above range, a change $\Delta RH = 40\%$ results in relative distance errors of close to 1 ppm. This shows a practical limitation of the method, but it also indicates that inline atmospheric compensation with an accuracy of about 1 ppm or better is possible with coarse meteorological measurements at the instrument location or even just assumptions on P and X_c. Sub-ppm level accuracy using the two-color method requires a good approximation of T and RH along the propagation path for appropriately computing the A factor and the corrected distance.

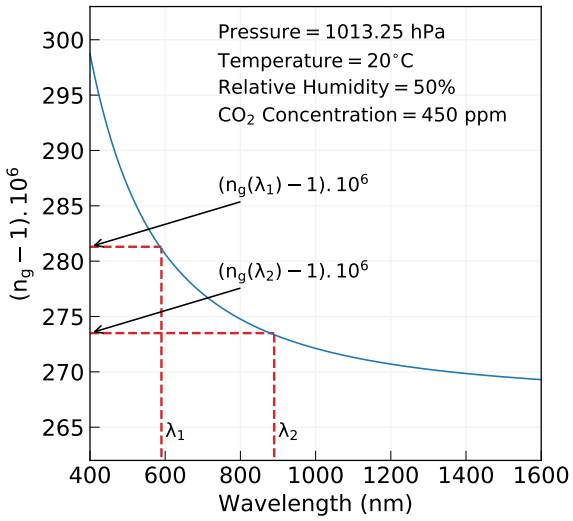

Figure 3.1. Dispersion profile of standard air over 400-1600 nm. Group refractivity indices for the wavelength pair 590/890 nm.

An important design choice is the selection of the two wavelengths which determines the value of A. Some approximate values of A for different wavelength pairs are listed in Table 3.1 (the values in the table and thereafter are calculated using Ciddor's group refractive index according to the corrected equations and implementation provided in the literature [38]). Taking these values and Eq. 3.1 into account, it can be deduced that any measurement noise of the difference between L_1 and L_2 is scaled up significantly, resulting in a higher standard deviation of the atmospherically corrected distance (D) than of the individual measurements L_1 and L_2. Thus, it is desirable to select the wavelength pair such that the value of A is as low as possible given the technological constraints of the instrument (e.g., the possible range of wavelengths, different atmospheric attenuation

at different wavelengths, and different measurement noise). This implies that the two wavelengths should be far separated from each other around the steeper gradient region of the dispersion curve while avoiding spectral regions (e.g., too close to the ultraviolet regime) with excessive atmospheric absorption or scattering.

Table 3.1. Dispersion coefficient for different wavelengths

Wavelength Pairs (nm/nm)	$\|A\|$ calculated from n_g
1560/780	47
1560/590	23
890/590	35

3.2.2. Intermode beating

The measurement principle that we use for the experimental setup relies on intermode beating [53, 28], where the beat notes are generated by direct photodetection of a filtered region of an SC. This technique assures a traceable link between the optical (THz) and radio (GHz) frequencies with high accuracy [75]. For example, if the frequency spacing of each comb line in the optical domain is f_r, the adjacent comb lines from filtered SC interfere with each other at the photodetector (PD), resulting in an electrical comb spectrum of mf_r where $m = 1, 2, 3, ...$ and limited by the PD bandwidth. Fig. 3.2 shows the optical power spectral density (PSD) of the filtered SC and the generated electrical comb PSD from direct photodetection.

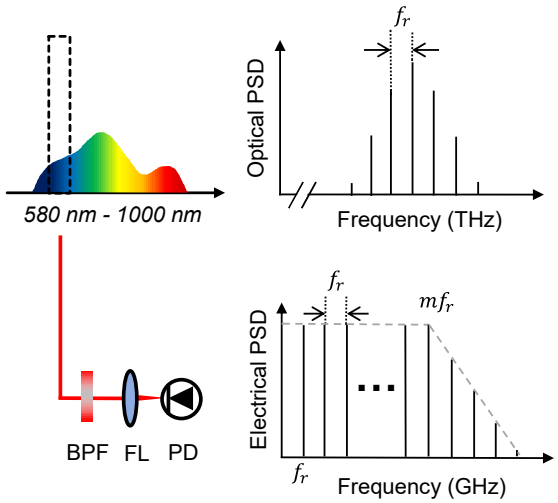

Figure 3.2. Schematic representation of the optical comb from the filtered spectrum of the supercontinuum and the intermode beat notes constituting the electrical comb (BPF, band-pass filter; FL, focusing lens; PD, photodetector; PSD, power spectral density)

A key advantage of this approach is that the individual intermode beat notes can be used for EDM like different measurement wavelengths in conventional phase-based EDM but without the need for actual modulators [28]. Besides, the frequency stability of

beat notes is similar to that of the original comb and is therefore suitable for delivering high-accuracy EDM.

Our measurements are derived from the phase difference ($\Delta\phi = \phi - \phi_{\text{ref}}$) of one of the beat notes $m'f_r$ over a measurement path of length L with respect to a fixed reference path L_{ref}. Omitting phase ambiguity for simplicity, the measured phases are

$$\phi(m'f_r) = \left(2\pi n_g^{\lambda}/c\right)\ m'f_r\ L + \phi_0 \tag{3.2}$$

$$\phi_{\text{ref}}(m'f_r) = \left(2\pi n_g^{\lambda}/c\right)\ m'f_r\ L_{\text{ref}} + \phi_0 \tag{3.3}$$

Where, n_g^{λ} is the group refractive index of air at λ, c is the speed of light in vacuum, and ϕ_0 is the common phase offset for the two paths. The differential path length ($\Delta L = L - L_{ref}$) is then estimated from the phase difference $\Delta\phi(m'f_r) = \phi(m'f_r) - \phi_{\text{ref}}(m'f_r)$ as

$$\Delta L = \left(c/2\pi n_g^{\lambda}\ m'f_r\right)\ \Delta\phi(m'f_r) \tag{3.4}$$

In general, higher-order beat notes are helpful to obtain higher distance precision for the same signal-to-noise ratio (SNR) due to the smaller scaling between phase and distance. The maximum beat note frequency is only defined by the PD bandwidth. Higher beat notes can therefore be accessed by selecting a faster PD as far as the current photodetector technology allows.

Besides the intermode beating approach, several other interferometric [37, 66, 77], advanced time-of-flight [59], and hybrid methods combining the interferometric phase and delay-based approaches [60] have also been reported in the literature. Although the sensitivity and precision of intermode beating-based EDM are not as high as the interferometric methods, this approach is robust against practical environmental fluctuations [31] hence adequate for long-distance measurements. Recent research has also shown that it is a promising alternative to other established EDM techniques such as time-of-flight or amplitude modulated phase-based EDM [53, 28].

3.3. Experimental setup

We have developed and calibrated an experimental platform implementing intermode beating based simultaneous EDM on two spectral bands derived from an fs-laser coherent supercontinuum (SC). A schematic of this setup is shown in Fig. 3.3. We use a 420 nm wide supercontinuum (SC) source spanning wavelengths from 580 nm to 1000 nm having a total optical power of slightly over 50 mW. The SC is derived from a frequency stabilized 780 nm mode-locked fs-laser (Menlo Systems C-fiber 780 SYNC100), spectrally broadened through a photonic crystal fiber (PCF) (Menlo Systems SCG1500). A Rubidium (Rb) frequency standard (SRS FS725) is used for internal stabilization of the 100 MHz pulse repetition frequency f_r of the laser and as the time basis for the mixing and acquisition electronics.

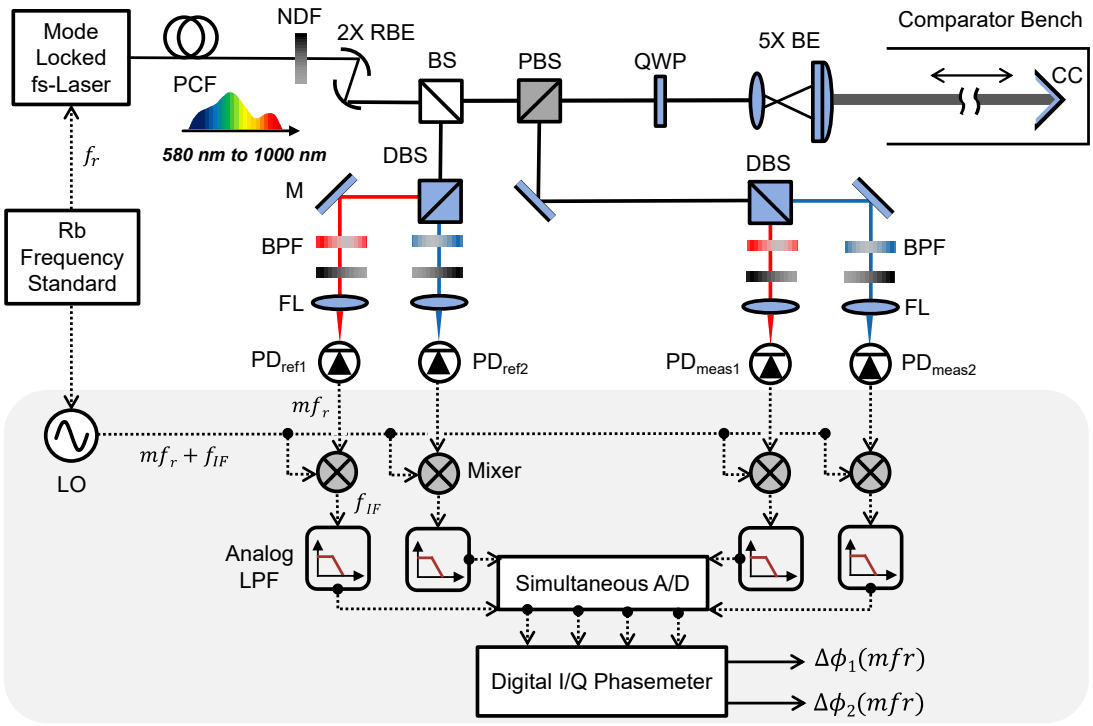

Figure 3.3. Diagram of the experimental setup (PCF, photonic crystal fiber; NDF, neutral density filter; RBE, reflective beam expander; BS, beam splitter; PBS, polarization beam splitter; QWP, quarter-wave plate; BE, beam expander; CC, corner cube; DBS, dichroic beam splitter; M, plane mirror; BPF, band-pass filter; FL, focusing lens; PD, Photodetector; LO, local oscillator; LPF, low-pass filter; A/D, analog-to-digital; I/Q, inline-quadrature)

Fig. 3.4 shows the optical spectrum of the generated SC as indicated by a Thorlabs CCS175 spectrometer. Although the average power of the SC is stable, its power spectral density is affected by significant temporal variations due to the high sensitivity of the seed 780 nm laser to thermal effects and optical changes (e.g., power, pointing, polarization) [49].

The wavelength pair and spectral bandwidth selection for the dual-wavelength measurements should therefore not only consider the dispersion factor (A) favoring wavelengths separated as far as possible, but also the spectral stability over time, and the integrated power per band defining the SNR of the generated beat notes. Taking these aspects into account, along with observations of our actual SC spectrum and its variability over time, we have selected two stable regions around 590 nm and 890 nm, extracted from the SC by band-pass filtering with 10 nm width right before photodetection (see Fig. 3.3).

These filtered bands from the reference and measurement paths are fed to individual high-speed avalanche photodiodes (Menlo Systems APD 210). The intermode beat notes generated at the detector are separated by 100 MHz (corresponding to the pulse repetition frequency of the laser), with a relatively constant power within the photodiode bandwidth up to 1 GHz. Our experiments use the phase-delay information on the 1 GHz beat note, which is the fastest available mode still providing high SNR. The 1 GHz intermode

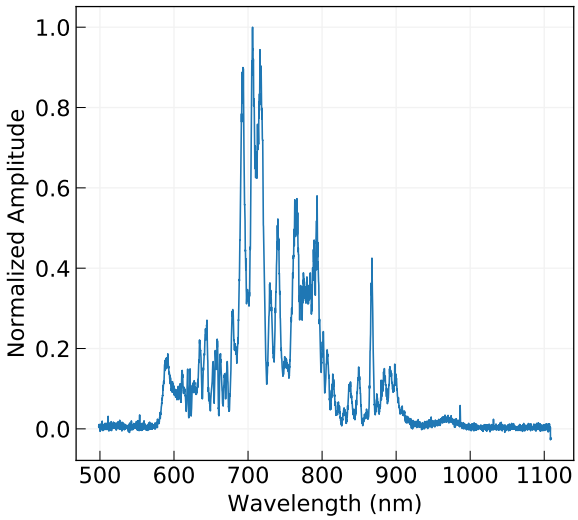

Figure 3.4. Instantaneous spectrum of the supercontinuum

beat is then down-converted to an intermediate frequency $f_{\mathrm{IF}} = 1$ MHz and acquired on a simultaneous digitizer at a sampling rate of 1.25 GS/s after anti-aliasing filtering. The phase difference between the reference and measurement paths per spectral band is estimated via a digital Inline-Quadrature (I/Q) phasemeter.

The measurement path is represented by a delay line formed using a moveable, highly achromatic corner cube (CC). The CC is mounted on a motorized, computer-controlled trolley that moves along a linear comparator bench. An additional reflector for a He-Ne laser Doppler interferometer (Agilent 5529A) is used as a reference for ground truth distances along the comparator, as shown in Fig. 3.5. The experiments were conducted under stable lab conditions of 20 °C, 960 hPa, and 50% relative humidity.

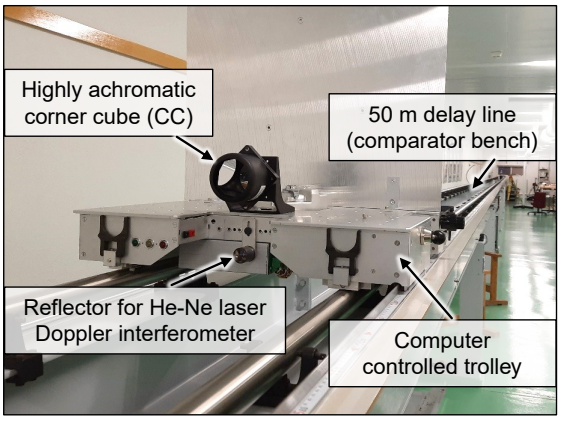

Figure 3.5. Picture of the computer-controlled trolley on a linear 50 m long comparator bench, along with the reflectors for SC-based EDM and He-Ne laser Doppler interferometer

3.4. Results

We assessed the distance measurement precision of the above dual-wavelength EDM experimentally using measurements to the CC located approximately 50 m away from the optical bench. Distance deviations from the initial value were computed from the beat note phase observations for the 590/890 nm wavelength pair. Fig. 3.6 shows the distance deviation (ΔL_λ) recorded over 20 minutes on the two spectral bands, where each measurement is averaged over 3 ms. The measurement precision estimated from the experimental standard deviation of the distance residuals is around 30 µm for 590 nm and 25 µm for 890 nm. We chose a relatively low data averaging time of 3 ms as a practical trade-off between precision and experiment duration considering current limitations in our processing speed (extracting the I/Q phase information from the acquired samples) for real-time use.

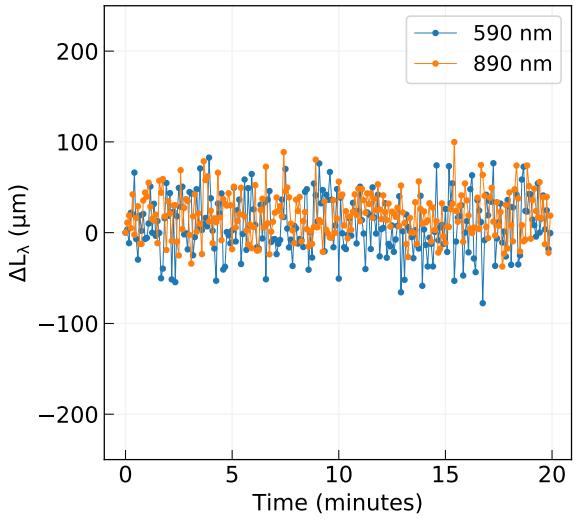

Figure 3.6. Distance deviation of individual observations averaged over 3 ms on a static reflector at 50 m

We have nevertheless investigated the expected distance uncertainty $\sigma(\Delta L_\lambda)$ for longer averaging time τ(s) on a single acquisition of 3.52 s at 1.25 GS/s. The results are obtained by computing the standard deviation of the distance time series ΔL_λ processed with moving average window length τ(s). The results, shown in Fig. 3.7, indicate a slightly higher overall measurement uncertainty on the 590 nm than on the 890 nm channel, likely introduced by higher phase noise in that region on the source spectrum.

The relatively flat response below $\tau = 10^{-4}$ s is caused by the noise bandwidth being limited by the internal 10 kHz filter used in the digital I/Q phasemeter. The flat region between 10^{-3} s to 10^{-1} s averaging time, on the other hand, suggests the presence of flicker frequency-modulation (FM) noise, which is typically related to the physical resonance mechanism of the active oscillator or FM noise in the electronics [78]. This flat region shows no significant improvement in the measurement uncertainty with increasing averaging time from 10^{-3} s to 10^{-1} s. Beyond $\tau = 10^{-1}$ s, a slope of around -1 suggests that white noise dominates the frequency range in the Hz level, enabling efficient precision improvement for averaging times of some tenth of a second. Such a reduction in distance

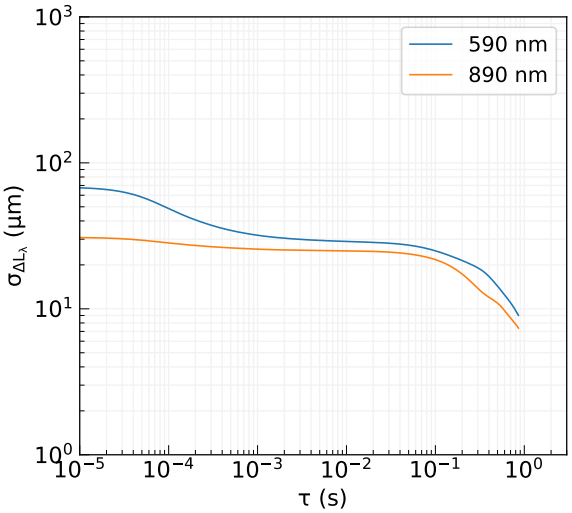

Figure 3.7. Distance deviation as a function of averaging time on a static reflector at 50 m

uncertainty indicates the feasibility of achieving $\sigma(\Delta L_\lambda)$ better than 10 µm over 50 m by using averaging times of about 1 s, i.e., precision on the order of 0.2 ppm.

Further experiments were performed to evaluate the measurement accuracy of the developed experimental platform, where the measurements obtained using our setup are compared with those from the reference interferometer. The experiments were repeated in 3 cycles at different instances of time (over 6 hours), where each cycle comprises of a forward (from 50 m to 49.4 m) and reverse motion (from 49.4 m to 50 m). The range of the measurements (0.6 m) was selected to cover more than one ambiguity range of the 1 GHz beat note frequency. Defined by half of the beat note wavelength, the ambiguity range in our experiments is 15 cm, which also determines the period of the main cyclic error component. The obtained results are shown in Fig. 3.8, where each data point represents an individual measurement averaged over 3 ms.

No further averaging could be introduced due to practical limitations related to the processing time of our setup. The obtained results are thus fully affected by the noise, and the precision in the current experiment is not better than the approximately 30 µm per channel described above. The results agree with the reference interferometer within 100 µm for both channels. Besides noise, a systematic cyclic error period of 15 cm is observed, as expected, in the 590 nm results.

Usually, such cyclic errors occur when the optical beam in the measurement path interferes with another phase-delayed component of itself (e.g., due to the presence of some spurious reflections from any optical component) or from electrical cross-talk of the photodetected beat notes before digitization. Generally, such cyclic errors are repeatable under similar measurement conditions and can be compensated through instrument calibration. On the other hand, the results obtained on 890 nm show no visible cyclic systematics, likely due to better optical isolation of this channel provided by a more efficient anti-reflection coating on the optical components.

Both channels show additionally slightly different bias per cycle. This shift in bias

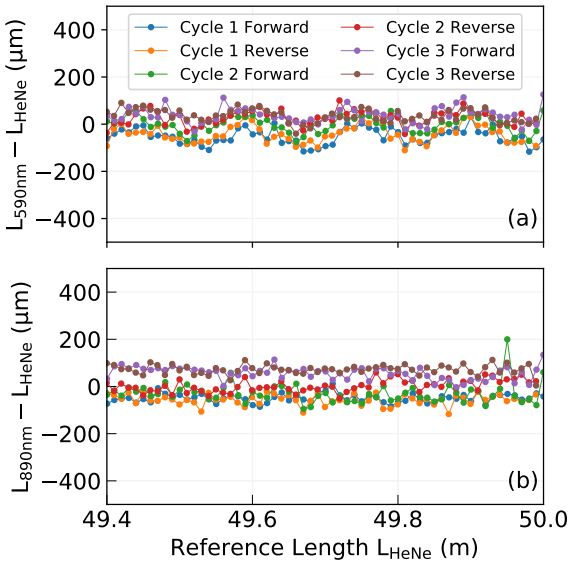

Figure 3.8. Residuals between the measured and reference (interferometer) distances for (a) 590 nm, (b) 890 nm

is caused by slow time-dependent drifts identified in long-term stability tests and can also be seen in these results upon careful inspection. Note the increasing bias with cycle number, which shows its correlation with time, evident in subsequent cycles 2-reverse and 3-forward of the 890 nm channel. Considering the timescale of this change (hours), we suspect this is due to the slow variations in the filtered SC power that couples into phase variations through optical power to phase coupling at the photodetector. Such effects due to power to phase coupling and pointing fluctuations have been previously reported in the literature [79] and are generally mitigated by adding an additional internal path measurement, also referred to as self-reference measurements [28, 31]. Fig. 3.9 shows the power fluctuations of our SC laser around the selected spectrum of interest and indicates the need for such self-referenced measurements in our setup. Further work is underway to study the long-term stability by investigating the performance of a self-referenced path in our setup.

3.5. Conclusions and outlook

We have developed a supercontinuum-based EDM platform using the intermode beating approach for dual-wavelength distance measurements over 50 m. The broad spectral bandwidth of the SC offers spectral flexibility in the wavelength selection and can also be extended to multi/hyperspectral EDM.

The measurement precision is approximately 30 µm on both the 590 nm and 890 nm spectral channels over a 50 m delay line for an integration time of around 3 ms, which can be further improved to $<$ 10 µm by increasing the averaging time up to around 1 s. This represents a transfer of performance from our previously reported results [31] to a range 3 orders of magnitude longer without any degradation. Considering these performance parameters and the dispersion coefficient ($|A| = 35$) for the 590/890 nm

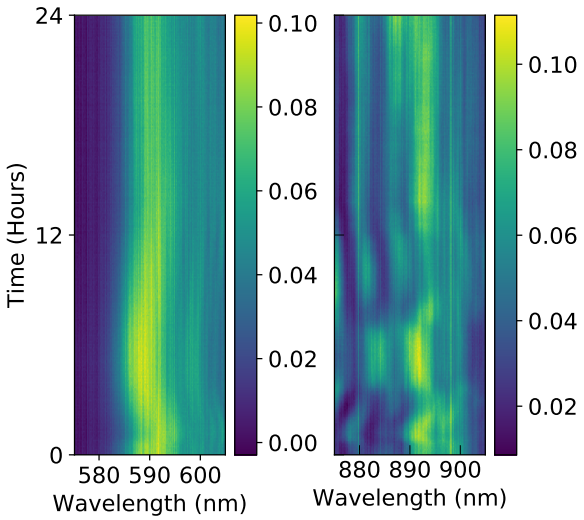

Figure 3.9. Long-term variation of the filtered supercontinuum spectrum

pair, the expected measurement precision of the refractivity-compensated distance from the dual-wavelength solution would be around 35 × 10 µm = 350 µm, with promising perspectives to similar performance on longer ranges over several hundred meters.

Besides the precision results, deviations between our results using intermode beating and the ground truth distances obtained from the interferometer were less than 100 µm on relative displacements at 50 m. These results are partly affected by systematic cyclic errors that can be largely reduced by calibration and by a slow drift caused by power and pointing to phase coupling, which we expect to mitigate significantly using internal self-reference double differences.

Further work is underway to implement these mitigation strategies and investigate the long-term stability of our setup. In addition, actual inline refractivity compensated EDM will be tested along with an investigation extension to more than two wavelengths for better atmospheric compensation.

4 | Refractivity corrected distance measurement using the intermode beats derived from a supercontinuum

Pabitro Ray, David Salido-Monzú, Robert Presl, Jemil Avers Butt, and Andreas Wieser
Optics Express, 32(7), pp. 12667-12681, 2024
doi: 10.1364/OE.514997

Abstract

Simultaneous distance measurements on two or more optical wavelengths enable dispersion based correction of deviations that result from insufficient knowledge of the refractive index along the signal propagation path. We demonstrate a supercontinuum-based approach for highly accurate distance measurements suitable for such an inline refractivity compensation. The distance is estimated from the phase delay observations on the intermode beats. We use a supercontinuum (SC) coherently broadened from a 780 nm frequency comb and spanning the spectral range of 570-970 nm. Experiments are performed on the 590 and 890 nm wavelength bands filtered from the SC spectrum. Results show distance measurements with standard deviations of around 0.01 mm at 50 m, and a distance-dependent component below 0.2 ppm on the individual spectral bands. Distance residuals compared to a reference interferometer are on the order of 0.1 ppm for displacements up to 50 m. Controlled pressure-induced refractivity variations are created over a length of 15 m, resulting in an optical path length change of 0.4 mm. Using the two-color method, we demonstrate refractivity-corrected distance measurement with a standard deviation of around 0.08 mm for a 60 s averaging window. The current experimental configuration can be easily extended to distance measurements on more than two wavelengths. The results highlight its potential for practical long-distance measurements through inline refractivity compensation.

4.1. Introduction

High-accuracy contactless distance measurements are essential in various applications such as large-scale industrial manufacturing, alignment of particle accelerators, surveying, and environmental monitoring. Commercially available laser-based distance meters can provide instrumental accuracy in the sub-mm to mm level over distances ranging from a few meters to several km. However, the measurement accuracy in practical conditions is limited by the spatial and temporal variability of the refractive index (n) of air resulting from variations in the density and composition of the air.

Conventionally, the refractive index of air is modeled as a function of temperature (T), pressure (P), relative humidity (RH), and CO_2 content (x_c) using empirical equations [10, 9]. The standard approach to account for refractivity in electro-optical distance measurement (EDM) is to record the meteorological parameters with sufficient temporal resolution at a few locations along the measurement path—typically only near the instrument and, if higher accuracy is needed, also near the end point of the distance—to calculate so-called meteorological corrections using a forward modeling approach [13]. The relative humidity and even more so the CO_2 content can often be neglected as they have much less impact than T and P for visible light and near-infrared. However, to properly account for refraction, the integral refractive index along the entire optical path is needed. Determining it from the few available meteorological measurements is very challenging. This is mostly due to the local differences and temporal changes in the spatial distribution of the temperature, and inherent uncertainties in the meteorological observations [13].

An alternative approach for refractivity compensation relies on atmospheric dispersion and uses simultaneous distance measurements at two or more wavelengths [14]. The method allows estimating the integral effect of the refractive index along the optical path and is robust to spatial and temporal fluctuations. Refractivity compensation using two wavelengths is typically known as the 'two-color method' [17]. It yields the estimated geometrical distance D as a linear combination of the measured optical path lengths ℓ_{λ_1} and ℓ_{λ_2} at two wavelengths λ_1 and λ_2:

$$D = \ell_{\lambda_1} - A \cdot \left(\ell_{\lambda_2} - \ell_{\lambda_1}\right). \tag{4.1}$$

The coefficient A is formally

$$A = \frac{n_{\lambda_1} - 1}{n_{\lambda_2} - n_{\lambda_1}}, \tag{4.2}$$

i.e., a function of the refractive indices along the path at the two wavelengths. It turns the second term on the right-hand side of eq. (4.1) into the correction of the integral refraction effect on ℓ_{λ_1}. Equations (4.1) and (4.2) hold for all atmospheric conditions. However, for dry-air ($RH = 0\%$) and under the practically valid assumption that the optical paths are nearly identical for both wavelengths, A is only a function of the wavelengths [37]. Thus, the significance of the two-color method is that it allows compensation for the refraction effect on distance measurements in dry air without any meteorological observations.

The main challenges of this method are that (i) the measurement uncertainties of $(\ell_{\lambda_2} - \ell_{\lambda_1})$ are scaled by the typically large value of A, and (ii) the air is rarely completely

dry and thus an error of $\Delta A \cdot (\ell_{\lambda_2} - \ell_{\lambda_1})$ is introduced in the compensation because the value of A calculated only from the wavelengths differs from the correct value according to eq. (4.2).

The first challenge can be mitigated by selecting a wavelength pair that ensures a comparably low value of A. This requires the wavelengths to be far apart, ideally one of them as close to the short wavelength end of the visible spectrum as possible and the other one in the near-infrared. While it is theoretically possible to achieve $A < 10$ with such a choice, values of about 20 or higher result if both wavelengths are longer than 550 nm. So, additionally very high accuracy (ideally µm level) for the optical path length measurements on the individual wavelengths, or at least for their difference, is needed in order to achieve high accuracy (mm- or sub-mm level) of the refraction compensated distance.

The impact of RH on D (in Eq. 4.1) is approximately 3 times higher than on the individual observations ℓ_{λ_i}. Neglecting RH introduces a relative error of around 2 ppm on D for $RH = 100\%$ at temperatures below about 20°C, and more at higher temperatures. Nevertheless, a relative uncertainty better than 0.1 ppm on D can be achieved if RH is monitored with a measurement uncertainty below 4% [63], although this may be difficult in practical conditions and undermines the original idea of the two-color method, namely to compensate without requiring meteorological observations. Theoretically, the impact of RH can also be eliminated by using optical path length measurements on more than two wavelengths. A three-color method has been proposed in the literature [15]. However, the measurement uncertainties in this approach are scaled by parameters on the order of 10^3 in the visible and near-infrared region, making the three-color method so far unsuitable for practical applications. For many applications, challenge (ii) thus remains but affects the two-color method mostly by a moderate or even negligible degradation of the accuracy as compared to what can be achieved in dry air.

Recent technological advances in optical frequency combs (FC) have enabled highly precise and accurate measurements over long distances due to the intrinsically high stability of the optical frequencies and coherence lengths of several km [29]. Since the first demonstration of applying FC for distance measurements, using the intermode beats [53], various alternative techniques also using FC have been demonstrated, such as those based on interferometry [64], dual-combs [60, 61], and time-of-flight [59] ranging.

FC-based two-color solutions have also been presented in the literature [62, 67, 80, 66]. In controlled conditions, two-color refractivity compensated distance measurements have achieved accuracies even better than the accuracy of the empirical refractive index equations and thus better than the accuracy achievable using meteorological observations and forward modeling, see [65, 81]. Recently, a sub-mm two-color EDM using an intensity-modulated continuous wave approach has also been demonstrated over 5 km [82]. Typically, a frequency-doubled source or a combination of FC centered at different wavelengths has been used in such investigations. However, the approaches lack spectral flexibility in selecting the wavelength pair and require very high accuracy and stability of the spatial alignment of the multiple beams [83]. A multi-color method ($>$ 3 wavelengths) has recently been demonstrated to mitigate the impact of varying RH [16]. The authors used a SC source ranging from 1100 to 1700 nm and a dispersive interferometry-based

approach to achieve high-precision distance measurements. The sweep speed of the optical spectrum analyzer (OSA) limits the data acquisition rate in this approach. The method requires high signal-to-noise (SNR) and fine resolution of the OSA for enhanced distance resolution [84].

We have previously demonstrated a new approach for SC-based multi-wavelength distance measurement using intermode beating [30]. This approach allows accurate and absolute distance measurements using the FC as a modulator [28]. The SC used in our experiments covers the spectral range of 570-970 nm, taking advantage of the steeper gradient of the dispersion curve to achieve a low A factor. Additional co-alignment of multiple beams (at different wavelengths) is not necessary with our approach as the wavelengths are optically filtered from the same SC beam.

In this paper, we show an improved experimental design achieving a measurement precision on the order of 10^{-7} over a distance of 50 m. Distances are simultaneously measured on two spectral bands filtered from the SC spectrum. We further assess the observed distance precision as a function of the measurement distance and data integration time. Our results demonstrate long-term measurement stability over several hours, which was a major limitation in our earlier work. We compared our results with those obtained from a reference interferometer to estimate the distance accuracy of our measurements. For the first time, we also show two-color inline refractivity correction using the intermode beats obtained through the wavelength pair filtered from the SC. The current experimental setup offers the flexibility to select any wavelength pair within the bandwidth of the SC. Additionally, the system could easily be modified to allow for using a larger number of wavelengths and thus apply the intermode beating approach to multi-color distance measurements.

The paper is organized as follows: the measurement principle and the experimental setup are described in Sec. 4.2. This includes a presentation of the lab setup for creating a significant but controlled refraction effect already at short distances. The experimental results on range precision, relative accuracy, long-term stability, and refractivity correction are presented in Sec. 4.3. In Sec. 4.4 we summarize the primary contributions with an outlook on the practical challenges and future directions of this work.

4.2. Methods

4.2.1. Experimental approach

We use a SC spectrally broadened from a 780 nm mode-locked fs laser (Menlo Systems C-fiber 780 SYNC) by transmitting through a photonic crystal fiber (Menlo Systems SCG1500). The generated SC spectrum ranges from 570 to 970 nm with an integrated optical power of around 26 mW. We set the pulse repetition rate of the mode-locked laser to $f_r = 100\,\mathrm{MHz}$, locked to a rubidium frequency standard (SRS FS725) for accurate reference. Fig. 4.1(a) shows an instantaneous spectrum of the resulting SC as observed by a commercial spectrometer (Thorlabs CCS 175).

As mentioned earlier, a low A-factor is desirable for the two-color method. Given the

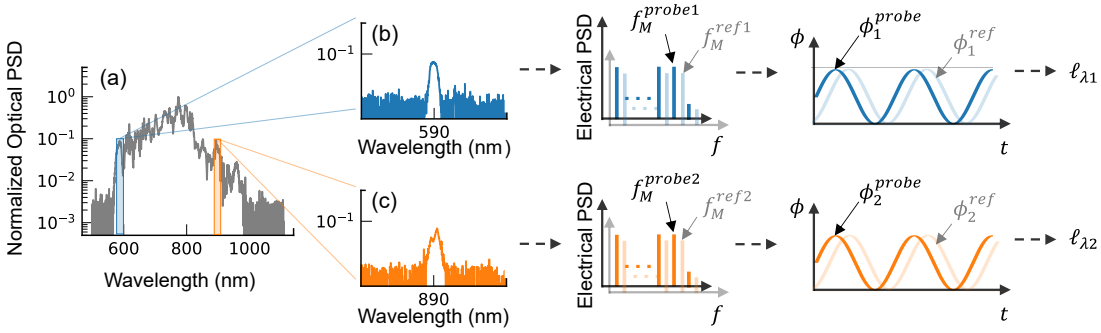

Figure 4.1. (a) Normalized instantaneous spectrum of the SC output; band-pass filtered spectrum of the (b) 590 nm and (c) 890 nm spectral bands; a schematic representation of the measurement principle showing the electrical power spectral density (PSD) of the intermode beat notes and phase shifts allowing distance estimation.

dispersion characteristics of air, this implies that the wavelength pair should be taken from the extreme ends of the SC spectrum. However, taking the power distribution of the available SC into account, we have selected 10 nm wide spectral bands centered at $\lambda_1 = 590$ and $\lambda_2 = 890$ nm for further use herein. This resulted in a still acceptably low A factor (approximately 36) while ensuring an adequate SNR. The A factor is calculated from the group refractive indices at λ_1 and λ_2 from the corrected Ciddor's equation provided in [38]. The spectral bands are filtered using optical bandpass filters (BPF) centered at λ_1 and λ_2, see Fig. 4.1.

Corresponding electrical beat notes (mf_r, where $m = 1, 2, 3, \cdots$) equally separated by f_r are generated upon the photodetection of these spectral bands. The maximum beat note frequency is limited by the bandwidth of the photodetector (PD). Any of these beat notes can be used for distance measurements, where the higher frequency intermode beats offer better measurement precision due to their higher distance-to-phase sensitivity. Herein, we use an avalanche photodiode (APD) with a -3 dB bandwidth of 1 GHz, and process the 10^{th} harmonic mode, $f_M = 1$ GHz, to achieve high-precision distance measurements. For each of the wavelengths λ, the optical path length (ℓ_λ) is calculated from the differential phase observations on f_M between a fixed local reference path (ϕ^{ref}) and a probe path (ϕ^{probe}), see Fig. 4.1. The estimated distance L_λ at each wavelength is derived from these phase observations as

$$L_\lambda = \frac{c}{2n_g^\lambda f_M}\left[\frac{\phi_\lambda^{\text{probe}} - \phi_\lambda^{\text{ref}}}{2\pi} + N_M\right], \tag{4.3}$$

where, n_g^λ is the group refractive index at λ, c is the speed of light in vacuum, N_M is number of round-trip range ambiguity cycles $\Lambda_M := c/(2n_\lambda^g f_M)$, and the optical path length is $\ell_\lambda = n_g^\lambda L_\lambda$. Due to our choice of the 1 GHz beat notes, we have $\Lambda_M \approx 15$ cm, herein.

4.2.2. Experimental setup

A schematic diagram of the experimental setup is shown in Fig. 4.2. The system depicted here comprises the optical and electronic parts along with a test track (comparator bench) on which a corner cube reflector can be moved to distances up to about 50 m, and refractivity variations can be introduced in a controlled manner.

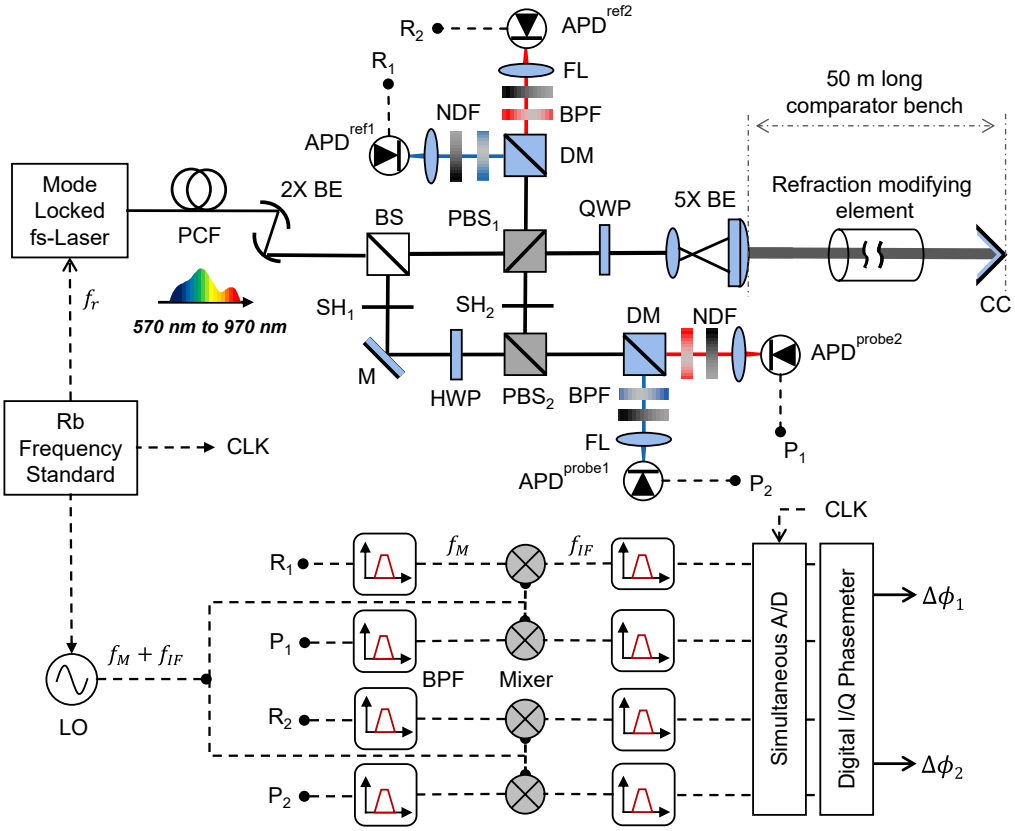

Figure 4.2. Schematic representation of the experimental setup (PCF: photonic crystal fiber; BE: beam expander; BS: beam splitter; PBS: polarization beam splitter; DM: dichroic mirror; BPF: band-pass filter; FL: focusing lens; NDF: variable neutral density filter; APD: avalanche photodiode; SH: mechanical shutter; M: plane mirror; HWP: half-wave plate; QWP: quarter-wave plate; CC: corner cube; CLK: clock; LO: local oscillator; A/D: analog-to-digital; I/Q: in-phase/quadrature.

Distance meter

The fiber-collimated SC output beam has a diameter of about 4.5 mm. It is expanded in two stages to a final diameter of about 45 mm to maintain collimation over the entire probe path, and to reduce the impact of pointing fluctuations on the measurements. Taking potential chromatic aberration into account, we have chosen a reflective-type beam expander (BE, 2X magnification) and a set of achromatic doublets (5X BE) for this. The s-polarized light reflected from a broadband polarization beam splitter (PBS_1, Thorlabs CCM1-PBS252) between the first and second stage of the beam expansion forms the local reference path, and the transmitted p-polarized light constitutes the probe path.

The reference path beam is spectrally split using a dichroic mirror (DM, Thorlabs DMSP650). The spectral bands, mentioned above, are filtered using the respective optical BPF, and each of them is fed to one APD. R_1 and R_2 represent the two RF signals (containing the electrical beat notes) for λ_1 and λ_2, respectively. On the probe path, the p-polarized light passes through a broadband quarter-wave plate (QWP) and is launched onto the comparator bench. An achromatic corner cube (CC), mounted on a computer-controlled trolley that can move along the entire length of the comparator bench, reflects the beam along the same optical path. The beam becomes s-polarized after passing again through the QWP. It gets reflected, spectrally separated and directed onto the two probe APDs (one for each wavelength) in a configuration similar to the reference path. The RF signals from the probe APDs are denoted as P_1 and P_2.

An additional compensation path is included to monitor the phase errors introduced by small drifts in the electronic setup, including variations of the propagation speed within the high-frequency cables. This approach is similar to the experimental configuration described in [28] and used there to achieve stable measurements over several hours. We use a 70:30 beam splitter (BS) to redirect 30% of the SC power onto the compensation path. This beam passes through a broadband half-wave plate (HWP) and finally the same elements as the probe beam before reaching the probe APDs. The optical power illuminated on each APD is controlled using variable neutral density filters (NDF) and is adjusted to around 12 µW to guarantee operation within the linear region of the APDs. Two mechanical shutters SH_1 and SH_2 are used to alternate between the probe and compensation path measurements.

The 1 GHz beat note is filtered from the respective RF signals using analog BPFs centered at f_M. The filtered beat notes are downconverted to an intermediate frequency of $f_{\mathrm{IF}} = 400$ kHz upon mixing with a signal generated from a local oscillator (LO). The downconverted signals are again filtered using analog BPFs, now centered at f_{IF}, to reduce SNR degradation by noise aliasing. The signals are subsequently digitized simultaneously using a 4-channel analog-to-digital converter (ADC, Spectrum Instrumentation M4i.2234-x8). A digital in-phase/quadrature (I/Q) phasemeter is implemented to retrieve the phase observations on each channel. Using Eq. 4.3, the optical path length at each wavelength is then estimated from the observed phase differences. Accurate clock references to the LO and ADC are also obtained from the Rb frequency standard.

To later also assess the accuracy of the measured distances, a He-Ne Doppler interferometer (Agilent 5519A) is included in the setup. It provides reference values of the trolley's displacement. The interferometer uses a different retroreflector mounted below the CC on the same automated trolley. Although Abbe's principle [85] is therefore not maintained, the spatial separation of approximately 5 cm between these two reflectors is small enough such that potential (minute) tilt or orientation changes of the trolley are negligible, see. Fig. 4.3(a). The probe and interferometer beams are both aligned to be sufficiently parallel along the comparator bench such that also the potential cosine error [86] is negligible.

Refraction modifying element

Air conditioning keeps the temperature in our lab constant within about 0.5 °C and relative humidity within 3%, or better. Spatial variations of the refractive index of the air in the lab are small (on the order of 1 ppm or less), and temporal variations are mostly caused by natural changes of the barometric pressure outside the building. In order to produce refractive index variations of experimentally useful magnitude along the probe path in a controlled manner, we have included a refraction modifying element on the comparator bench for the experiments described in Sec. 4.3.4. Taking into account the dimensions of the lab, the previously found precision of the optical path length measurements (a few micrometers), the A factor, and the desired flexibility to easily add or remove the element, we have decided for a design which can create a relatively large change of the refractive index (on the order of 45 ppm or more, as compared to the ambient conditions in the rest of the lab) over a short distance.

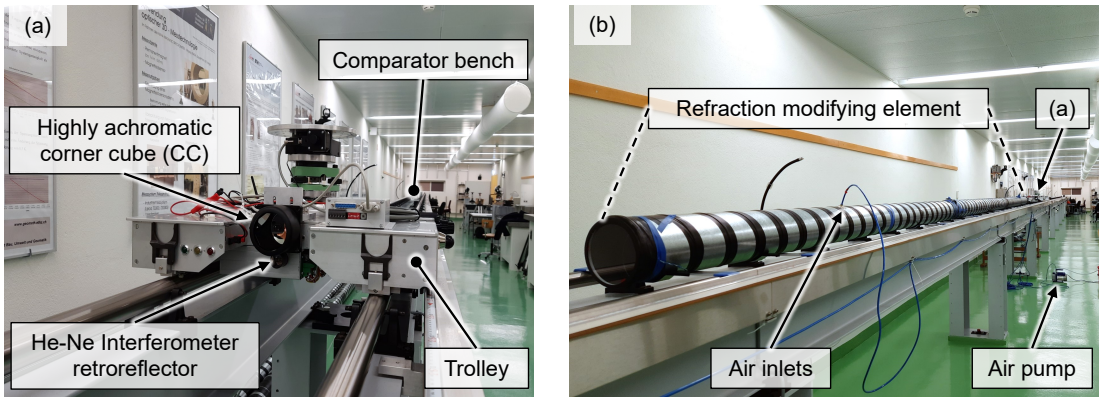

Figure 4.3. Picture of the (a) computer-controlled trolley on a linear 50 m long comparator bench fitted with the retroreflectors for SC-based distance measurements and the reference He-Ne interferometer, (b) refraction modifying element i.e., 9 m long sealed cylindrical tube placed on the comparator bench.

We initially considered introducing refractivity changes through temperature variations along the probe path. However, it required a temperature difference of about 45 °C or more to create the refractivity change mentioned earlier. Instead, the solution that we found practical and have finally used in our experiments was based on creating a local change of the barometric pressure within a sealed cylindrical tube with clear optical windows on both ends. We used a 9 m long sealed steel tube connected to an electrical air pump that depressurizes the tube by extracting air from the inside. We obtained the experimental results shown in Sec. 4.3.4 by carrying out measurements while this tube was temporarily placed on the comparator bench between the distance meter and the trolley with the CC. A picture of the computer-controlled trolley and the sealed cylindrical tube is shown in Fig. 4.3.

Our experiments were conducted under stable lab conditions at 20°C, 50% relative humidity, 410 ppm CO_2 content, and an average barometric pressure of around 960 hPa.

The meteorological changes over the maximum duration of our experiments (i.e., around 5 hours) were $\Delta T \leq 0.3$°C, $\Delta P \leq 2$ hPa, $\Delta RH \leq 1.5\%$ and $\Delta x_c \leq 30$ ppm, which resulted in meteorologically-induced distance errors (driven by ΔT and ΔP) that do not exceed 0.4 ppm. Distance errors originating from potential physical deformations of the comparator bench during the experiments are negligible compared to the target accuracy of our experiments. So, noticeable distance changes were only introduced in a controlled manner by moving the trolley and by using the depressurized tube.

4.3. Results

4.3.1. Measurement precision

In this section, we present experimental results on the estimated measurement precision as a function of distance and data integration time. The CC was moved from a distance of 10 m to 50 m in equidistant steps of 5 m and kept stationary during the data acquisition at each distance. The variable NDFs were adjusted at each step to maintain approximately the same intensity of the illumination on all APDs and for all distances of the CC. This helped to reduce potential errors related to the relative power-to-phase coupling [28].

Fig. 4.4(a, b) shows the time series of distance deviations (ΔL_λ) from the initial measurement simultaneously acquired on λ_1, λ_2 for the CC at a (one-way) distance (L) of 10 and 50 m, respectively, from the instrument. Each of these data points was obtained by averaging over an integration length of τ_w. Unless otherwise indicated, we use $\tau_w = 27$ ms to compute our results and denote this particular integration time as τ_w' henceforth.

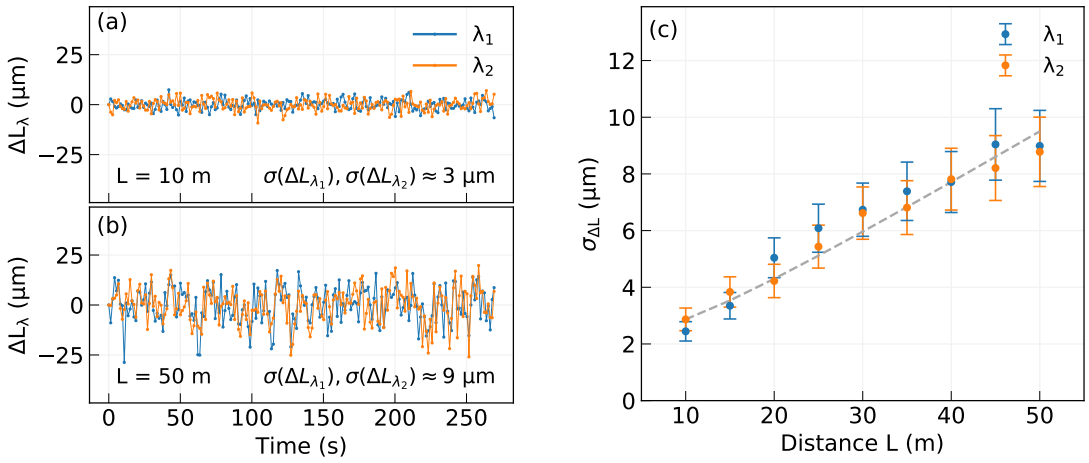

Figure 4.4. Time series of the observed distance deviations at (a) 10 m and (b) 50 m where each measurement point is averaged over 27 ms, (c) empirically estimated measurement precision as a function of the distance (L) to the corner cube. The estimated fit to the observations (from Eq. 4.4) is shown as dotted line.

We quantify the measurement precision using the empirical standard deviation ($\sigma_{\Delta L}$) calculated from the 200 data points of the respective time series. The standard deviation is around 3 µm at 10 m and 9 µm at 50 m on both wavelengths. The data were processed in

near real-time, where each measurement epoch takes about 1.3 s of computation time on a standard PC to process the data acquired on both wavelengths. The processing speed could be significantly improved by more powerful or dedicated hardware and parallel processing if a higher acquisition rate were required.

Fig. 4.4(b) illustrates the observed $\sigma_{\Delta L}$ for each color and distance. Assuming a normal distribution of the distance deviations, we have calculated the 95% confidence bounds of the empirical standard deviations and plotted them as well in this figure. We express the dependence of $\sigma_{\Delta L}$ on L using the conventional model

$$\sigma_{\Delta L} \approx \sqrt{\sigma_0^2 + (k_L \cdot L)^2}, \tag{4.4}$$

where σ_0 represents the measurement noise floor including error sources from mechanical vibrations and other optical and electronic instabilities, and k_L represents the coefficient of the distance-dependent contributions, which include, among others, impacts of beam divergence, atmospheric attenuation, and beam pointing. From our data we estimated these values to be $\sigma_0 \approx 2$ µm and $k_L \approx 0.18$ µm/m. The magnitude of k_L suggests the possibility of achieving sub-mm level precision over several km in controlled conditions. However k_L may increase under practical outdoor conditions, considering more significant air turbulence and scattering due to atmospheric particles. This needs to be further investigated once outdoor measurements are possible with a successor of our current setup.

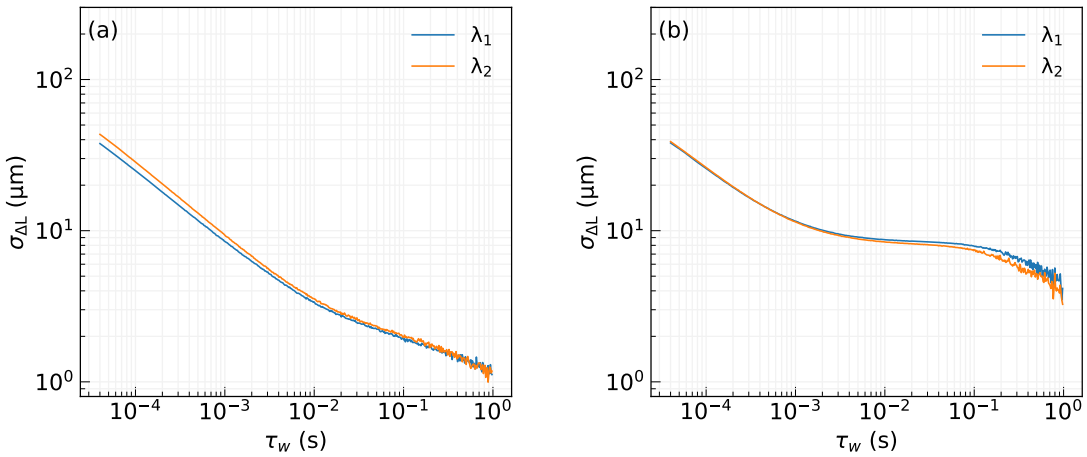

Figure 4.5. Empirically estimated distance precision as a function of data integration time τ_w at (a) 10 m and (b) 50 m.

We also investigated the dependence of $\sigma_{\Delta L}$ on the data integration time, as shown in Fig. 4.5(a,b) for 10 and 50 m respectively. The underlying raw data are a time series of distance observations acquired with a data rate of approximately 78 MS/s during around 56 s (limited by the ADC buffer memory). These data were then processed offline using non-overlapping moving average windows of length τ_w. For each chosen value from $\tau_w = 0.04$ ms to $\tau_w = 1$ s we calculated the empirical standard deviation $\sigma_{\Delta L}$. The log-log plot of the results for the 10 m distance, see Fig. 4.5(a), indicates a slope of around $-1/2$ up to 10 ms, implying that the measurement processes are dominated by white noise [78] at this distance. The slower improvement of precision with integration time

beyond 10 ms suggests the presence of slow drifts at sub-Hz to Hz levels. They may originate from mechanical vibrations of the experimental setup and temporal variations of the optical power on the individual spectral channels.

At a distance of 50 m, see Fig. 4.5(b), white noise characteristics are observed up to integration times of $\tau_w = 1$ ms. The improvement of precision with increasing integration time then reduces, and the precision hardly changes for integration times from 40 ms to 0.1 s, suggesting the presence of correlated noise in the data [78]. This effect may be attributed to temporal beam-pointing fluctuations at these timescales. For integration times beyond 0.1 s, the measurement precision again shows white noise-dominated characteristics and improves further with longer integration times. The range precision can be improved to around 5 µm at 50 m using $\tau_w = 1$ s. The results suggest the possibility of achieving a measurement precision below 0.1 ppm using integration times of about 0.5 to 1 s.

4.3.2. Relative accuracy

To evaluate the measured distance accuracy, we compared our results with those obtained using the reference interferometer. We moved the CC back and forth in 3 cycles between 49 and 50 m at equidistant steps of 1 cm. At each step we averaged a set of 5 data points, where each data point was obtained in real-time by integrating over τ'_w.

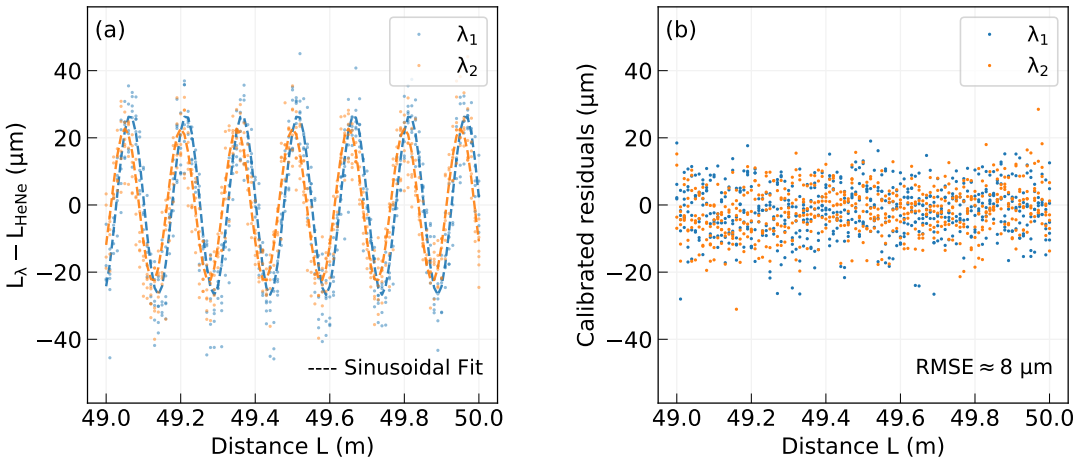

Figure 4.6. (a) Residuals between the measured (L_λ) and the reference interferometer (L_{HeNe}) showing cyclic error and the sinusoidal calibration fit between 49-50 m, (b) residuals after calibration.

The residuals obtained by subtracting our measurements from the reference measurements are shown in Fig. 4.6(a). They are all within ±45 µm and dominated by systematic cyclic errors which are induced by optical or electrical cross-talk. Due to their systematic nature they can be mitigated by calibration [87]. The observed cyclic error period is around 15 cm, which corresponds to the range ambiguity Λ_M, see sec. 4.2, of the 1 GHz beat note used in our experiments. We determined a correction by fitting a sinusoidal function with a fixed period of Λ_M to the residuals from Fig. 4.6(a). The post-calibration residuals are shown in Fig. 4.6(b). The root-mean-square error (RMSE) of these residuals

is around 8 µm on both wavelengths, corresponding to a relative accuracy on the order of 0.1 ppm at a distance of 50 m.

4.3.3. Long-term stability

As described in Sec. 4.2.2, we have implemented an internal compensation path to ensure the stability of our measurements over extended periods. Regulated by the two mechanical shutters SH_1 and SH_2, the distance observations are acquired on the probe (L^{probe}) and compensation (L^{comp}) path alternatively. L^{probe} is estimated using Eq. 4.3 from the simultaneous phase observations on the reference and probe path. Equivalently, L^{comp} is estimated from the reference and internal compensation path. A low-pass filtered (moving-averaged) output $\bar{L}^{\text{comp}}$ is used to rectify the slow bias errors on L^{probe}.

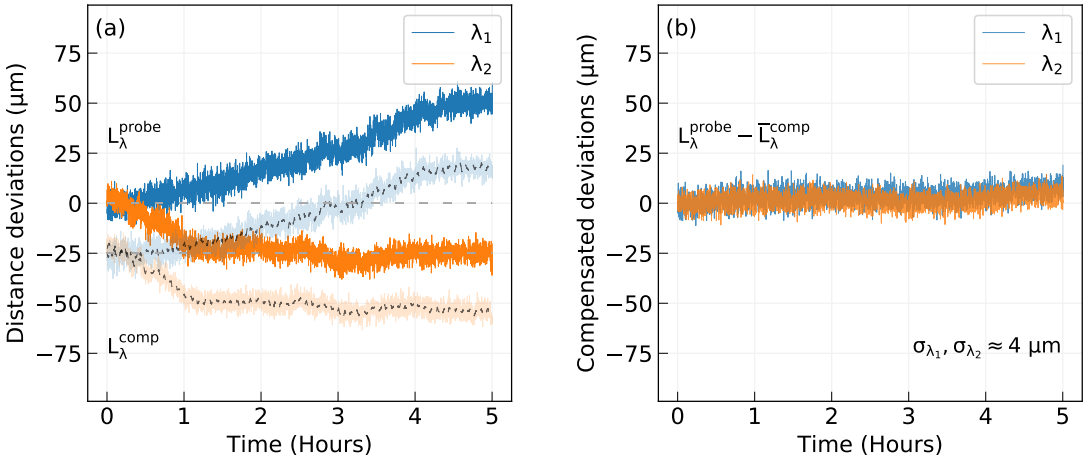

Figure 4.7. Distance deviations ($L \approx 2$ m) monitored over 5 hours showing (a) long-term drifts in the probe path measurements L^{probe} and corresponding measurements from the internal compensation path L^{comp} (shifted by −25 µm for clarity), (b) compensated measurements ($L^{\text{probe}} - \bar{L}^{\text{comp}}$).

Fig. 4.7(a) shows the deviations in the probe and compensation path measurements monitored over 5 hours. The CC is placed at a close distance (about 2 m) to reduce the distance-dependent errors and assess the performance of the internal compensation. Measurements are taken approximately every 4 s, each averaged over τ'_w. The observations of L^{comp} are shown in a lighter color tone with an offset of −25 µm for better clarity. The 15-point moving-averages $\bar{L}^{\text{comp}}$ are shown as black dashed lines. The moving-average window size corresponds to a time constant of around 59 s. Deviations of around 60 and 40 µm can be observed on the L^{probe} measurements at λ_1 and λ_2 respectively, depicting significant temporal variations over the measurement duration. The variations of the compensation measurements L^{comp} exhibit a similar trend.

The distance observations representing long-term stability are then calculated as ($L^{\text{probe}} - \bar{L}^{\text{comp}}$) and are shown in Fig. 4.7(b). The significant temporal drifts are eliminated, and the compensated measurements are almost stable over time. The estimated standard deviation and mean offset of the resulting time series is around 4 µm. The minor residual drifts are correlated with the small changes in the barometric pressure (≈ 2 hPa) and temperature (≈ 0.3 °C) during the measurement.

4.3.4. Refractivity compensation

We conducted further experiments to demonstrate inline refractivity compensation using intermode beating. The 9 m long sealed tube was placed on the comparator bench to create pressure-induced refractivity changes along the probe path. The CC was placed at a distance of 15 m (i.e., $L = 15$ m), and the tube was positioned between the distance meter setup and the CC, leaving a gap of 3 m on each side. Fig. 4.8(a) shows a time series of the air pressure (P) variation attained inside the tube. The pressure starts decreasing when the connected air pump is switched on and gradually increases again when the pump is switched off (driven by small leaks in the pipe assembly). The maximum ΔP achieved is approximately -166 hPa, and the temperature change (ΔT) within the tube is about 0.2 °C following a similar pattern as the pressure change. The resulting refractive index change Δn is around -45×10^{-6} inside the sealed tube, which is primarily dominated by the pressure variations.

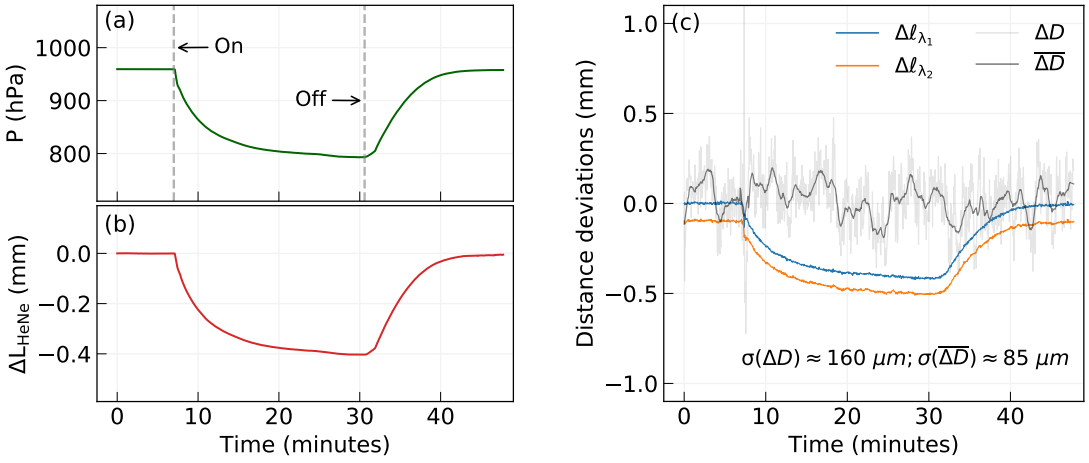

Figure 4.8. Time series showing (a) pressure variations of P monitored within the tube, (b) corresponding distance deviations measured using the reference interferometer ΔL_{HeNe}, (c) simultaneously acquired optical path length deviations on the two wavelengths $\Delta\ell_{\lambda_1}$ and $\Delta\ell_{\lambda_2}$ (which is shifted by -0.1 mm for clarity), two-color refractivity compensated measurements ΔD, and its 21-point moving-averaged result $\overline{\Delta D}$.

Fig. 4.8(b) shows the apparent distance changes ΔL_{HeNe} of up to -0.4 mm, observed using the reference interferometer. This is consistent with our theoretical predictions from the empirical equations [10, 9] and can be estimated as Δn times the length of the refraction modifying tube, i.e approximately $-45 \cdot 10^{-6} \times 9$ m. As expected, ΔL_{HeNe} follows the same pattern as the pressure variations introduced within the pipe.

The observed optical path length changes ($\Delta\ell_{\lambda_1}, \Delta\ell_{\lambda_2}$) with respect to the initial value at each wavelength are shown in Fig. 4.8(c), where $\Delta\ell_{\lambda_2}$ is shifted by -0.1 mm for clarity. The experiment implements differential measurements to the internal compensation path to ensure long-term stability. The variations $\Delta\ell_\lambda$ of the measured path lengths also exhibit a similar pressure-driven pattern and distance deviations as observed for the reference interferometer in Fig. 4.8(b). The estimated change in geometrical distance ΔD derived from Eq. 4.1 using the observations ℓ_λ is depicted in Fig. 4.8(c). The resulting

estimated distance shows that the induced drift apparent in $\Delta\ell_\lambda$ and in the reference interferometer measurements is suppressed, thereby demonstrating an effective two-color refractivity compensation. As anticipated, the measurement uncertainty is scaled by the A factor. The empirical standard deviation $\sigma(\Delta D)$ before filtering is around 160 µm. The noticeable sharp peak in ΔD at around 7 minutes is likely caused by a large beam pointing related phase error when the pump is switched on. The ΔD observations are averaged using a 21-point (about 60 s) moving window to eliminate the higher frequency fluctuations. The filtered data ($\overline{\Delta D}$) is also shown in Fig. 4.8(c). The empirical standard deviation $\sigma(\overline{\Delta D})$ is around 85 µm, indicating a relative distance precision on the ppm-level without using any external meteorological observation. Each data point is based on only 27 ms integration time followed by a break of almost 3 s, introduced in this experiment because of data storage and raw data processing limitations of our current experimental setup. Based on the noise analysis presented earlier (see. Sec. 4.3.1), we expect that the same standard deviation would be achieved by averaging 21 measurements collected directly after each other, i.e. by averaging over less than 0.6 s, and a further improvement can be achieved by averaging longer.

Due to non-dry conditions the A-value calculated from the wavelengths (see Sec. 4.1) is wrong by about $|\Delta A| \approx 0.031$ for the maximum ΔP observed herein. The dispersion measurement $(\ell_{\lambda_2} - \ell_{\lambda_1})$ is around 10 µm at the corresponding time. Consequently, the impact of humidity on the distance measurements is on the order of $\Delta A \cdot (\ell_{\lambda_2} - \ell_{\lambda_1}) \approx$ 0.3 µm, and can thus be neglected in comparison to our measurement precision. The residual errors in $\overline{\Delta D}$ over the expected noise-related uncertainty scaled up by the A factor may originate from wavelength-specific beam pointing and optical power instability [88]. Nevertheless, using our current experimental setup, we were able to achieve refractivity-corrected distance measurements on the ppm level over the assessed range.

While this relative precision indicates promising perspectives towards the extension of the method to longer practically useful ranges, some additional challenges should still be considered. On the one hand, the distance errors induced by refractivity variations become more noticeable when the measurement range extends beyond a few hundred meters. Considering e.g. a range of 500 m, i.e. more than 30 times longer than our current experiments, a refractivity change or error of 10 ppm that can be expected in practical conditions would lead to a single-wavelength distance error of about 5 mm. Considering the distance-dependent coefficient k_L for the precision on individual wavelengths as modeled through our experiments, the two-color compensated precision would be better than 5 mm using integration times of tens of ms and can be further improved by longer averaging, thus still providing useful compensation. However, increased turbulence over longer distances may lead to further degradation of performance led by pointing and power fluctuations. Extending the averaging time window can partly reduce these errors, but more specific mitigation procedures should also be considered and further investigated.

Various techniques have been demonstrated in the literature to experimentally analyze [28], suppress [89], and characterize the pointing and power-to-phase conversion effects [90, 79]. An amplitude fluctuation-based data selection has been shown to be effective in eliminating power-to-phase errors for measurements over several km, which are strongly affected by atmospheric turbulence [91]. The recent technological advances in developing

ultra-low-noise SC sources (characterized by low relative intensity noise and high phase coherence) also contribute towards reducing the phase errors caused by the inherent power instabilities [92]. Further exploring the potential solutions to mitigate these effects is essential to develop the proposed approach towards working implementations in real conditions.

4.4. Conclusion and outlook

We have investigated the potential of coherently broadened fs-lasers for refractivity-compensated distance measurement. The developed experimental platform achieves highly precise and accurate distance measurements at multiple spectrally filtered bands from a coherent supercontinuum. Distances are estimated from the differential phase delay accumulated on the 1 GHz beat note. For single-wavelength measurements integrated over 27 ms, we obtained standard deviations below 10 µm over a distance of 50 m, and found that this standard deviation contains a length-dependent contribution of below 0.2 ppm. Additionally, we observed that the precision of the measurements can be improved by integrating over longer times; the standard deviation generally decreases with integration time τ_w, and is even inversely proportional to the square root of the integration time for certain ranges of τ_w. Compared to a reference interferometer, our measurements show a relative accuracy on the order of 0.1 ppm after calibrating the systematic cyclic deviations. Additional observations from an internal compensation path are used to achieve measurement stability over several hours. We further demonstrated inline refractivity compensation using the two-color method. Pressure-induced refractivity variations were created along the measurement path, and the refractivity corrected distance measurements show an empirical standard deviation less than 0.1 mm at 15 m when the optical path length change is about 0.4 mm. Phase errors originating from power and pointing instability are the current limitations of our experimental setup. Further investigations are necessary to calibrate or suppress the power-to-phase conversion characteristics. The experimental setup can be easily extended for simultaneous multi-color distance measurements by including measurements from additional photodetectors. This may enable a promising technological basis for practical long-distance measurements.

5 | Supercontinuum-based hyperspectral LiDAR for precision laser scanning

Pabitro Ray, David Salido-Monzú, Sandro L. Camenzind, and Andreas Wieser
Optics Express, 31(20), pp. 33486-33499, 2023
doi: 10.1364/OE.498576

(Author version; for typeset version please refer to the original paper)

Abstract

Hyperspectral LiDAR enables non-contact mapping of the 3D surface geometry of an object along with its spectral reflectance signature and has proved to be effective for automated point cloud segmentation in various remote sensing applications. The established hyperspectral LiDAR methods offer a range precision of a few mm to a few cm for distances exceeding several meters. We propose a novel approach to hyperspectral LiDAR scanning based on a supercontinuum (SC) coherently broadened from a 780 nm frequency comb. It provides high precision distance measurements along with target reflectance over the 570–970 nm range of the SC output. The distance measurements are carried out by monitoring the differential phase delay of intermode beat notes generated by direct photodetection, while the backscattered light spectrum is acquired using a commercial CCD spectrometer with 0.16 nm resolution across the 400 nm bandwidth of the SC output. We demonstrate a measurement precision below 0.1 mm for a stand-off range up to 50 m on a diffuse target with around 89% reflectance. The measured relative accuracy as compared to a reference interferometer is on the order of 10^{-5} for distances up to 50 m. Initial results also indicate spectrum-based material classification within a 3D point cloud using a linear support vector machine. The results highlight the potential of this approach for joint high-precision laser scanning and automated material classification.

5.1. Introduction

Light detection and ranging (LiDAR) enables accurate three-dimensional (3D) digitization of our surroundings and is widely used for applications like remote sensing, surveying, autonomous driving, and deformation monitoring [5, 93, 21]. Conventional laser scanning (also referred to as LiDAR scanning) uses a monochromatic laser source to capture the 3D surface geometry (x, y, z) of a target and, after compensating for attenuation due to distance and angle-of-incidence also surface reflectance (R_λ) at the optical wavelength (λ). As compared to monochromatic LiDAR, combining the range information with extended spectral reflectance data over several (multispectral) or a continuous distribution of wavelengths (hyperspectral) has proved to be advantageous for finer point cloud segmentation, remote spectroscopy, and material classification [94, 95].

Photogrammetric methods can be used to derive 3D point clouds with spectral information $(x, y, z, R_{\lambda_1,..,\lambda_n})$ from images of conventional cameras and multi- or hyperspectral cameras. However, the co-registration of spectral and range data can be challenging in such imaging methods [23]. Besides, the photogrammetric methods typically rely on identifying radiometric surface features to establish point correspondences between images acquired from different viewpoints. Hyperspectral LiDAR (HSL) can overcome these challenges by simultaneously acquiring geometric and spectral information from the same measurement point and more independently from the surface appearance [96]. This facilitates accurate target identification by capturing the distinct spectral signatures of objects [97, 73].

Dual-wavelength solutions using independent laser sources are already used commercially for airborne laser scanning [98]. Some experimental systems on dual or multiwavelength solutions for terrestrial laser scanning have also been presented in the literature. For instance, the Echidna LiDAR uses data from two 5 ns pulsed lasers at 1064 and 1548 nm to distinguish leaves from wood over a range of more than 70 m for characterizing forest canopy structures [99]. A multiwavelength approach using measurements at four different visible and near-infrared wavelengths combined with a separate range finder has also been shown to be advantageous for remote sensing of vegetation [100]. However, these approaches primarily rely on prior knowledge for selecting the optical wavelengths corresponding to a specific classification task e.g. selecting specific wavelength pairs for known vegetation indices. The broader range of available wavelengths provided by HSL allows for greater spectral flexibility to gather further insights into the target material properties.

The first prototype of an active full-waveform HSL was based on a SC incoherently broadened from a pulsed laser and provided spectral data for 16 channels within 450-1050 nm [24]. The authors demonstrated a range precision of 11.5 mm over distances of 20 m using direct time-of-flight (ToF) based ranging. Other techniques based on ToF measurements and advancements over the performance (measurement range, precision) of the initial prototype have also been reported in the literature [26, 101, 25]. Nevertheless, these early HSL methods use direct delay-based ToF approaches with limited scope for further pulse optimization and are limited to mm to cm range precision over a few tens of meters.

Recent advances in frequency combs (FC) technology have opened a possibility to achieve high precision for distance measurements even over long range [53]. Key properties of FC laser sources are their very high frequency stability ($\Delta f/f \approx 10^{-10}$ or better) and their extended coherence length (km-range) [102, 75]. Since the first demonstration of using FC for distance measurements on cooperative targets (reflectors) [53], various methods have been implemented to extend their application towards non-cooperative targets (natural surfaces). FC-based frequency-modulated continuous wave (FMCW) LiDAR has been demonstrated over distances up to 10.5 m with sub-µm accuracy and measurement precision below 10 µm [68]. Similar precision at 3.5 m has been reported using dual-comb ranging [103]. An intermode beating (self-beating) based non-scanning experimental setup has been also proposed for profile measurements of rough surfaces with a relative accuracy of around 0.4 mm compared to a coordinate measuring machine [69]. While these techniques substantiate the possibility of achieving high precision ranging over several meters, their spectral flexibility is limited to the center wavelength of the FC used in the application.

In this paper, we propose a novel approach for HSL based on a supercontinuum (SC) obtained from coherent broadening of a 780 nm FC. Distance measurements are acquired using the intermode beats derived from direct photodetection of the SC. The spectrum of the backscattered light is captured over the 400 nm (570–970 nm) bandwidth of the SC. We assess the performance of the proposed approach experimentally under controlled conditions over a range of up to 50 m. The assessment includes precision and its dependence on target reflectance, distance, and data integration time, as well as accuracy in comparison to a laser Doppler interferometer (LDI). The achieved results demonstrate the potential of broadband intermode beating-based LiDAR to overcome the ranging performance limits of current HSL alternatives. Furthermore, we present initial results on SC spectrum-based material classification distinguishing different types of wood within the scan of a test object. This provides an outlook on combined high-precision laser scanning and simultaneous material probing.

The paper is organized as follows: the measurement principle, experimental setup, and reflectance properties of the targets used in our work are introduced in Section 5.2. The experimental results in terms of range precision, relative accuracy, and spectrum-based material classification are presented in Section 5.3. Section 5.4 summarizes the primary contribution of this work with directions for further research.

5.2. Methods

5.2.1. Experimental setup

We use a SC source spanning the spectral range of 570-970 nm with an available optical power of around 26 mW. An instantaneous spectrum of this SC as observed on a commercial Czerny-Turner CCD spectrometer (Thorlabs CCS 175) is shown in Fig. 5.1(a). The SC is generated through a photonic crystal fiber (PCF) (Menlo Systems SCG1500) that coherently broadens a 780 nm mode-locked femtosecond laser (Menlo Systems C-fiber 780 SYNC100) with a pulse repetition rate (f_r) of 100 MHz locked to a Rubidium (Rb)

frequency standard (SRS FS725). Coherent broadening using the PCF ensures retaining the comb line spacing f_r in the SC [49].

When the SC illuminates a photodetector (PD), these equally separated optical comb lines at f_r beat with the adjacent modes resulting in an electrical comb spectrum mf_r (where $m = 1, 2, 3, ...$) limited by the PD bandwidth [53]. Fig. 5.1(b) shows the electrical power spectral density of the intermode beats obtained from an avalanche photodiode (APD) with a nominal bandwidth of 1 GHz. The electrical beat notes each separated by 100 MHz can be clearly observed up to the APD bandwidth in Fig. 5.1(b). The spurious beat notes (prominent beyond 1.2 GHz) are measurement artifacts of temporal aliasing caused by the analog-to-digital converter (ADC) sampling rate. The sampling rate of the ADC was set to 5 GHz.

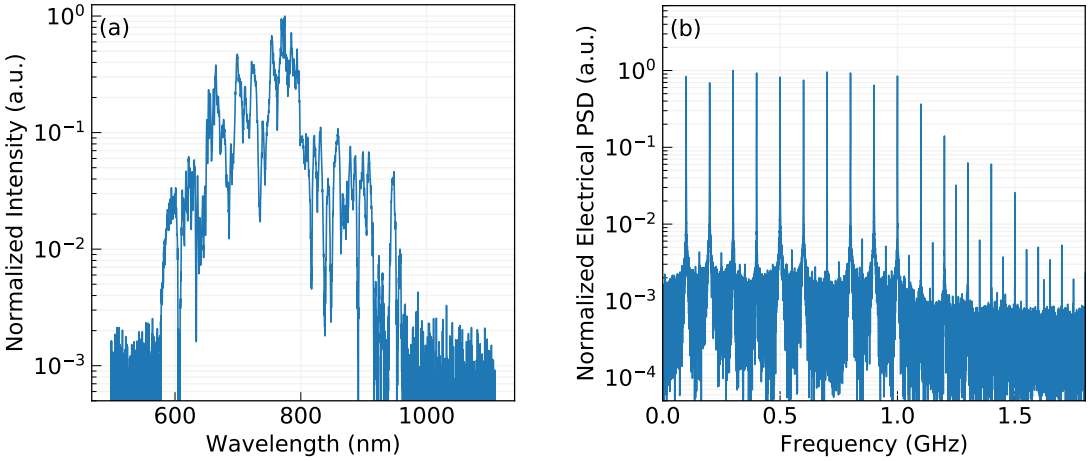

Figure 5.1. (a) Instantaneous optical spectrum of the supercontinuum, (b) electrical power spectral density (PSD) of the intermode beat notes obtained from direct photodetection of the supercontinuum on a high-speed avalanche photodiode with a bandwidth of 1 GHz

Compared to established phase-based distance measurement techniques which use amplitude-modulated continuous-wave lasers, the intermode beat notes provide high-quality radio-frequency (RF) modulation signals without requiring an external modulator. The phase of the beat notes is proportional to the propagation delay. The distance measurement (D) is estimated from the differential phase delay observed simultaneously on a local reference and probe path, which can be expressed as

$$D = \frac{c}{4\pi n_g^{\lambda} f_M}[\phi_{\text{probe}}(f_M) - \phi_{\text{ref}}(f_M)] + N_M \cdot \frac{c}{2f_M} \tag{5.1}$$

where c is the speed of light in vacuum, n_g^{λ} is the group refractive index of air at wavelength λ, $f_M = M \cdot f_r$ is the specific M^{th} beat note selected for the distance measurements, $\phi_{\text{probe}}(f_M)$ is the phase delay accumulated on the probe path and $\phi_{\text{ref}}(f_M)$ is the local reference path phase, both measured on beat note f_M. A center-of-mass calculation is used to estimate the effective $n_g(\lambda)$ [26], which corresponds to $\lambda \approx 750$ nm in our measurements. The second additive term in Eq. 5.1 represents the range ambiguity as an unknown integer N_M times half the modulation wavelength cycles $c/(2f_M)$ [104].

Conventionally N_M is determined by combining measurements at different modulation wavelengths or by an independent measurement having an absolute accuracy better than the range ambiguity. Since the higher frequency beat notes offer better distance precision due to higher distance-to-phase sensitivity, we use the 1 GHz beat note (limited by the APD bandwidth) for precision measurements i.e. $f_M = 1$ GHz. The 1 GHz beat note corresponds to a range ambiguity of around 15 cm considering the round-trip propagation path. A significant increase in precision can be expected by accessing the higher-order beat notes using faster photodetectors and adapting the acquisition electronics accordingly. Detailed explanations of the intermode beating approach for distance measurement and related experimental implementations can be found in [31, 30].

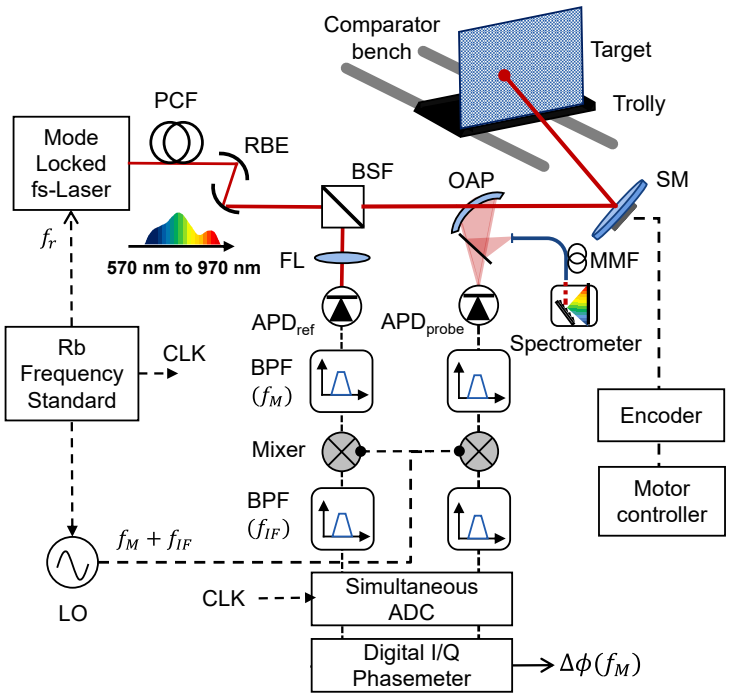

Figure 5.2. Schematic representation of the experimental setup (PCF: photonic crystal fiber; RBE: reflective beam expander; BSF: beam sampler; OAP: off-axis parabolic mirror; SM: Scanning mirror; FL: focusing lens; APD: avalanche photodiode; MMF: multi-mode fiber; BPF: band-pass filter; LO: local oscillator; CLK: clock; ADC: analog-to-digital converter; I/Q: inline-quadrature)

A schematic of the experimental setup is shown in Fig. 5.2. The fiber-collimated SC output is expanded to a beam diameter of 9 mm using a reflective-type beam expander (RBE) to maintain collimation over a longer range while minimizing chromatic aberration. A beam sampler (BSF) picks off ∼10% of the SC output to establish a reference arm which is used to monitor ϕ_{ref} (see Eq. 5.1) using APD$_{\text{ref}}$. The probe arm passes through the scanning unit which comprises an achromatic off-axis parabolic (OAP) mirror, the scanning mirror (SM) assembly, the probe photodetector (APD$_{\text{probe}}$), and a spectrometer. An OAP mirror with a 17.7 mm through-hole and 3″ surface diameter is used to optimize the forward beam propagation without clipping and to efficiently collect the back-reflection

from diffusely reflecting targets. The scanning mirror assembly consists of a 4″ diameter flat deflection mirror placed on a programmable motor-controlled 2-axis gimbal, which enables accurate and repeatable beam steering for laser scanning. The current design of our experimental prototype can measure up to about 180° horizontally and 90° vertically. A detailed explanation of the features and calibration of the scanning unit is provided in **Supplement 1** (see 5.5).

The back-reflection collected by the OAP mirror is focused onto the $\mathrm{APD}_{\mathrm{probe}}$ for the distance measurements. The electrical intermode beats generated at the APDs (see Fig. 5.1(b)) are fed to an analog band-pass filter (BPF) to isolate the 1 GHz beat note (denoted as f_M). The 1 GHz signals from the reference and probe paths are downconverted to an intermediate frequency $f_{\mathrm{IF}} = 400$ kHz upon mixing with the output of a local oscillator (LO) set to $f_M + f_{\mathrm{IF}}$. To further improve the signal-to-noise ratio (SNR) and reduce phase uncertainty, a second set of analog BPF centered at 400 kHz with 100 kHz BW is used. The f_{IF} signals are acquired simultaneously using a 2-channel ADC at a sampling rate of around 78 MS/s. The acquired time series is processed using a digital inline-quadrature (I/Q) phasemeter to estimate the phase difference corresponding to the propagation distance. Accurate timing references to the LO and ADC are also obtained from the Rb-frequency standard used for the mode-locked laser.

Due to practical space constraints in our initial design, the focused light from the OAP could not be coupled simultaneously to both the spectrometer and the $\mathrm{APD}_{\mathrm{probe}}$ placed on the scanning module. For the experimental investigation herein, we thus replaced the $\mathrm{APD}_{\mathrm{probe}}$ with the spectrometer to record the reflection spectrum of the target in a consecutive set of measurements. The target and the scanning module are not moved within these sets to ensure point-to-point correspondence between the range and spectral information (limited by the position accuracy of the scanning mirror assembly). This experimental choice is not a fundamental limitation of the approach; simultaneous acquisition is possible with a modified setup at the expense of optical power by splitting the backscattered light to the photodetector and spectrometer.

All the experiments are conducted under stable lab conditions at 20 °C and 50% relative humidity. The barometric pressure cannot be controlled in the lab but remained within the range of 955 to 958 hPa over the entire duration of the experiments. Thus, the distance error caused by variations of the meteorological conditions and corresponding changes of the refractive index of air as well as potential temperature-induced deformations of the experimental setup can be neglected over the measurement range of 50 m.

5.2.2. Target properties

A picture of the two targets used in our experiments is shown in Fig. 5.3. The planar target (Fig. 5.3(a)) with visibly white, grey, and black cardboard is used to assess the ranging precision and accuracy performance of our experimental setup and to investigate the effect of surface reflectance on the measurement precision. The cardboard pieces are pasted on a 60 × 60 cm^2 aluminum plate for stability and are fixed to a computer-controlled motorized trolley that can move along the 50 m length of a comparator bench. The type of cardboard was chosen such as to be smooth and reflect diffusely over the

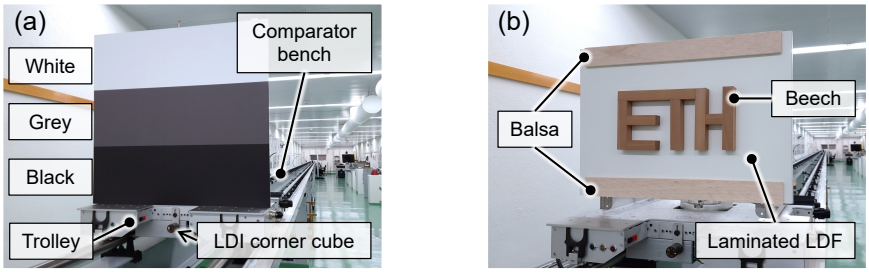

Figure 5.3. (a) Planar target with visibly white, grey, and black cardboard having different reflectances placed on a computer-controlled trolley for 5–50 m displacement tests on the comparator bench; a corner cube reflector is fitted to trolley for laser Doppler interferometer (LDI) measurements, (b) target made of three wood varieties: beech, balsa, and laminated low-density fiberboard (LDF)

entire SC spectrum. To assess the relative ranging accuracy, the measurements obtained from our experiments are compared with reference measurements from a 633 nm He-Ne laser Doppler interferometer (Agilent 5529a). The interferometer uses a corner-cube reflector fixed on the trolley to deliver high-accuracy reference measurements and provide position feedback to the motor-controlling software. The experimental results presented in Sec. 5.3.1 and Sec. 5.3.2 are obtained using this planar cardboard target.

Fig. 5.3(b) shows the second target made of three varieties of wood that are used to demonstrate hyperspectral laser scanning and spectral signature-based material classification on a 3D-point cloud since the different materials exhibit different spectral signatures. A 40 cm × 55 cm white lacquer-coated flat low-density fiberboard (LDF) made from mixed wood is used as a background. Two rectangular pieces of 10 mm thick balsa are placed on the top and bottom part of the LDF, whereas the ETH letters are constructed using 25 mm thick beechwood pieces. Experimental results showing the acquired 3D point cloud of the wooden target along with spectrum-based material classification are presented in Sec. 5.3.3.

To estimate the reflectance (R_λ) of the cardboard and wooden specimens, an arbitrarily selected region on each of the samples was illuminated with a stabilized tungsten-halogen broadband light source (SLS201L, Thorlabs) at normal incidence through a contact probe and the reflected spectrum normalized to a diffusive 80% reflectance standard (Labsphere, SRT-80-050 Spectralon®) was recorded using the spectrometer. Using a second set of reference measurements acquired on a 5% reflectance standard (Labsphere, SRT-05-050 Spectralon®), the sample reflectance was estimated using two-point calibration. Fig. 5.4(a, b) shows the reference reflectances of the cardboard and wooden target captured through the contact probe using the broadband light source. The average estimated $\overline{R}$ for the white, grey, and black cardboard is approximately 89%, 42%, and 7% respectively over the spectral range of our SC. $\overline{R}$ of the wood varieties is around 82%, 63%, and 40% for the LDF, balsa, and beech samples respectively.

The spectrometer used in our experiments allows an integration time of 10 µs to 60 s. For the experiments herein, we chose an integration time of 90 ms as a trade-off

between the SNR of the collected light on the spectrometer and the scanning speed. The scanning speed of HSL using a spectrometer for acquiring the spectral signatures is primarily limited by the necessary integration time for an adequate SNR. However, the overall scanning speed of our prototypical lab setup is currently constrained by the real-time data processing of the range measurements, i.e. around 0.8 s per point, as discussed later in Sec. 5.3.1.

Fig. 5.4(c) shows the SC spectrum reflected from an arbitrarily selected region on the wooden samples and normalized to the spectrum of the background LDF. These measurements are collected using the scanning module for the target placed at a stand-off range of 5 m. The raw spectrum (shown in a lighter color tone) shows a higher measurement noise due to a lower SNR for measurements acquired over a longer distance. The peaks observed toward both extremes of the spectral distribution originate from the very low output power of the SC at these wavelengths and consequently higher deviations after normalizing with the background spectrum. The raw observations are processed with a moving-average window length of 10 nm to indicate the relative spectral differences between the different varieties of wood (shown in a darker color tone). These spectral variations exhibit similar trends as the reference spectrum in Fig. 5.4(b) which is exploited for their classification. The differences in the observed baselines may occur from a partly non-Lambertian reflection and from temporal variations of the SC power spectral distribution between the individual measurements [30]. These spectrum measurements using the SC do not reflect the absolute reflectance of the target specimens and would require extensive calibration as a function of distance, angle-of-incidence, surface roughness, etc. [105]. Nevertheless, preliminary investigations presented in Sec. 5.3.3 show spectrum-based classification of the wooden target using the relative differences in their acquired spectral signatures.

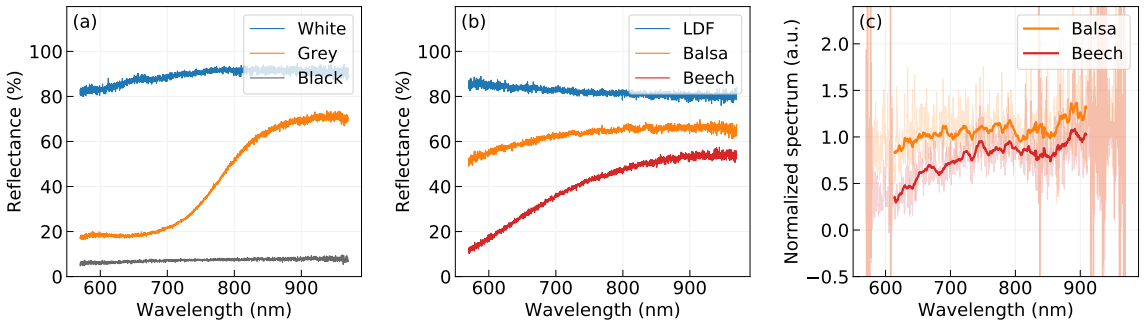

Figure 5.4. Reference reflectance signatures of the different targets: (a) visibly white, grey, and black cardboard surfaces, (b) laminated low-density fiberboard (LDF), balsa, and beech wood samples; (c) measured spectrum of the SC diffusely reflected from the wood specimens placed at a distance of 5 m and normalized to the LDF spectrum.

5.3. Experimental results

5.3.1. Range precision

We conducted the initial experiments on the planar target shown in Fig. 5.3(a) on different surface reflectances to assess the dependence of measurement precision on both reflectance (R) and distance (D) to the target. In a simplified approximation, the received signal power P_s can be expressed as

$$P_s = \eta \frac{\rho_R}{\pi} P_0 \cos\theta \frac{A_s}{D^2} \tag{5.2}$$

where η is the joint transmission and collection efficiency, ρ_R is the target reflectance ($= 0.01R$) at normal incidence, P_0 is the output laser power, θ is the incidence angle of the laser beam on the target, and A_s is the effective area of the scanning mirror [3]. This results in $P_s \propto \rho_R$, whereas $P_s \propto 1/D^2$. On the other hand, optical direct detection systems are typically dominated by the thermal noise of the PD under low optical power, being the standard mode of operation for long-range measurements on diffusive targets. Due to this constant noise contribution, the SNR of the acquired beat notes is expected to be directly proportional to the square of the optical power given the power-to-current conversion at the PD. The measurement uncertainty for I/Q-based phase measurements can be quantified by the standard deviation $\sigma_D \propto 1/\sqrt{SNR}$ [71] or as $\sigma_D \propto 1/P_s$. So, we expect the standard deviation of the distance measurements to be directly proportional to D^2 and indirectly proportional to the reflectance ρ_R, i.e.,

$$\sigma_D = k(\tau_w) \cdot \frac{D^2}{\rho_R} + \sigma_0 \tag{5.3}$$

where $k(\tau_w)$ is a scale factor depending on the data integration time τ_w and σ_0 is the signal-independent measurement noise floor (including mechanical sources of uncertainty such as vibrations).

Fig 5.5(a) shows the range precision empirically assessed using 100 measurements on an arbitrarily chosen fixed beam position on each of the three surfaces. The incidence angle of the laser beam is approximately normal to the white cardboard and $< 2.5°$ on the grey and black cardboard surface. Each data point is obtained by integrating the I- and Q- samples over a quasi-randomly chosen time of $\tau'_w = 13$ ms. The processing time for each measurement point is around 0.8 s on the standard PC used for processing the experimental data, herein. This is much longer than the acquisition duration. However, this is not a fundamental limitation for further development, because the processing time can be reduced using a faster computational unit e.g. using a GPU or FPGA. A measurement precision of around 3, 6 and 22 µm is achieved on the white, grey, and black surfaces, respectively, for a stand-off range of 5 m (see Fig. 5.5(a)). As expected the measurement precision is inversely proportional to R. However, the absolute precision values at a close-range (i.e. 5 m) are likely dominated by the underlying noise floor σ_0. σ_0 is empirically estimated to be around 2 µm.

We carried out further experiments to evaluate the effect of R and D on the range precision. The cardboard plate was displaced from 5 m to 50 m at equidistant steps of

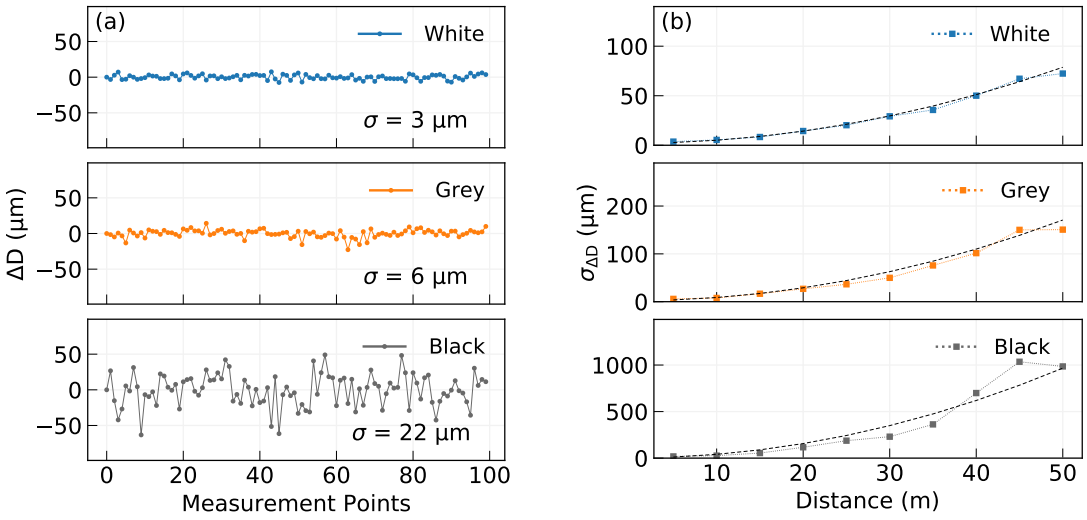

Figure 5.5. (a) Distance deviation of individual observations averaged over 13 ms on a static plate with three different reflectances, placed at 5 m; (b) precision as a function of the measurement distance (D) from 5 m to 50 m for the areas of different reflectance. The dotted lines represent the $\overline{k}D^2/\rho_R$ model shown in Eq. 5.3

5 m. A continuous time series of distance variations are recorded within 56 s at each of these distances and processed offline. Each measurement series is again integrated over τ_w' (i.e., 13 ms), which corresponds to around 4300 measurement points in the time series. The data points in Fig. 5.5(b) show the empirical standard deviation of these measurements at different distances. The theoretical model in the form of Eq. 5.3 (shown as dashed lines) is also computed for each case. The average scale factor $\overline{k}(\tau_w')$ for the three surfaces is estimated to be around 0.027 µm/m^2. A maximum relative error of 6% from this average model is observed for the black surface. The experimental results agree with the prior expectations with respect to reflectance and distance. A high measurement precision of 72 µm, 150 µm, and 985 µm at 50 m is demonstrated on the white, grey, and black surfaces respectively for an integration time of 13 ms.

We also analyzed the dependence of precision on the integration time. Using the acquired continuous time series of 56 s at 5 and 50 m, the standard deviations of the time series were processed within non-overlapping consecutive windows of duration $\tau_w(s)$. Within a certain range of window lengths, i.e. integration times, the measurement noise is dominated by white noise, as shown by the slope of $-(1/2)$ in the logarithmic plot of the empirical standard deviation versus τ_w (see Fig. 5.6). The slower precision improvement prominent after 20 ms on the white and grey surfaces visible only at 5 m suggest the presence of very slow signal drifts at Hz and sub-Hz rates that appear to be unrelated to the received signal noise distribution, and limit the reachable precision of the current implementation to the µm level. These may be introduced by mechanical vibrations of the measurement setup or electromagnetic interference at the high-frequency cables that are more apparent with increased signal strength. The slower precision improvement after 0.1 s for the black surface at 50 m appears to be dominated by quantization noise due to low SNR inherent to the challenging measurement conditions. Nevertheless, for

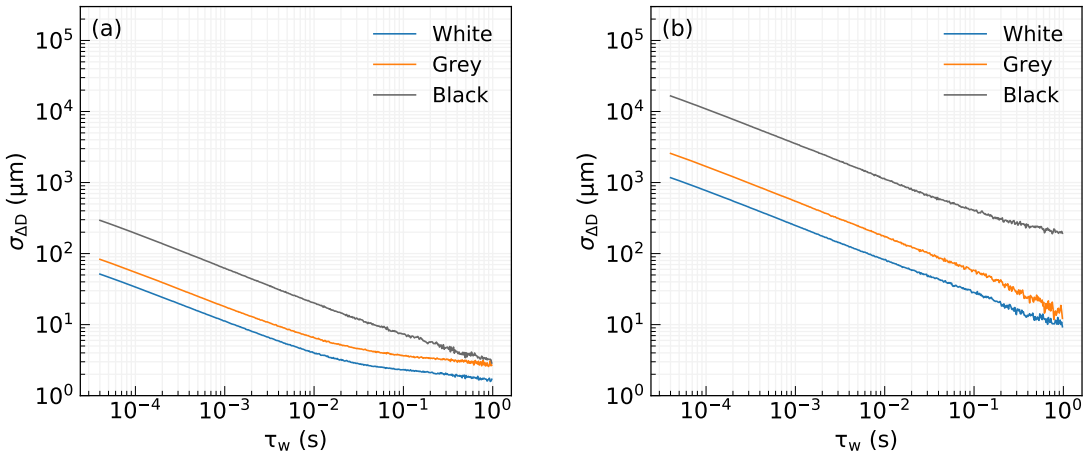

Figure 5.6. (a) Empirical standard deviation of distance as a function of data integration (averaging) time τ_w for different reflectances at (a) 5 m and (b) 50 m

longer averaging windows the measurement precision can improve significantly, e.g. to about 30, 60, and 400 µm for the white, grey, and black surfaces respectively for 50 m distance and integration time of 0.1 s.

The precision analysis is extended to include the impact of scanning. Fig. 5.7(a) shows a point cloud of the cardboard surfaces when placed at a stand-off range of 5 m. The corresponding histogram showing the statistical spread of the distance deviation is shown in Fig. 5.7(b). A total of 1722 points (574 points each on cardboard sample) were acquired on the planar target in a continued raster scanning pattern, where the deviations in range (or depth) are visible mainly along the z-direction because this is roughly the scanning direction, and the target is parallel to the x-y plane. We again used an integration time of τ'_w per point.

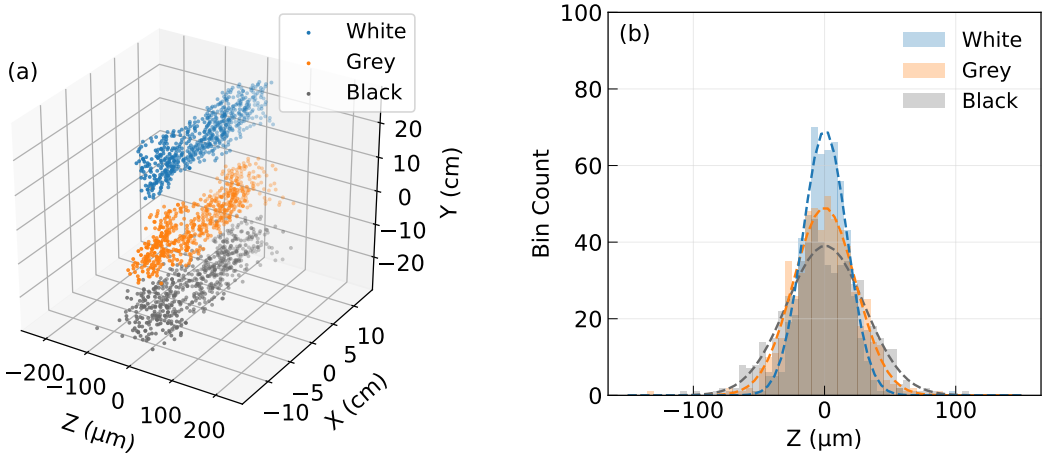

Figure 5.7. (a) Observed point cloud of the cardboard surfaces showing the distance deviations (along the z-axis, note different scale) for a stand-off range of 5 m, (b) histogram showing the statistical spread on the three surfaces

A standard deviation of 16, 23, and 29 µm is observed in the z-direction for points on the white, grey, and black surfaces. Similar to the observations on single-point precision, the scanning precision reduces for low-reflectance targets. However, the analysis is now also influenced by the non-planarity and surface roughness of the cardboard samples, as well as the remaining calibration errors of our scanning module. This explains the higher standard deviations compared to the precision of the single-point distance measurements (Fig. 5.5). However, we note that the apparent degradation of precision is large for the white surface for which the pure range noise was 3 µm before, while the degradation is small for the black surface for which the range noise was already 22 µm. These results suggest that the additional uncertainty caused by the surface and the scanning module is on the order of 10 to 20 µm, and the empirical standard deviations calculated from the point cloud represent the superposition of the pure range noise and these additional contributions.

5.3.2. Relative range accuracy

To also evaluate the measurement accuracy of the developed HSL prototype further experiments were conducted, where our measurements are compared to those obtained from the reference interferometer. These experiments were carried out in 3 cycles, each comprising a forward and reverse motion of the target from 5 to 6 m and from 49 to 50 m at steps of 1 cm. Measurements were acquired for one point on the white cardboard only for each of these target positions. This yields data of high precision, thus yielding high sensitivity of the analysis with respect to the identification of potential systematic effects (causing the accuracy to be lower than the precision). The results are shown in Fig. 5.8, where each data point represents an individual measurement averaged over τ'_w. Distance residuals were calculated as the differences between the measurements (D) of the SC-based distance meter and those of the reference interferometer (D_{HeNe}).

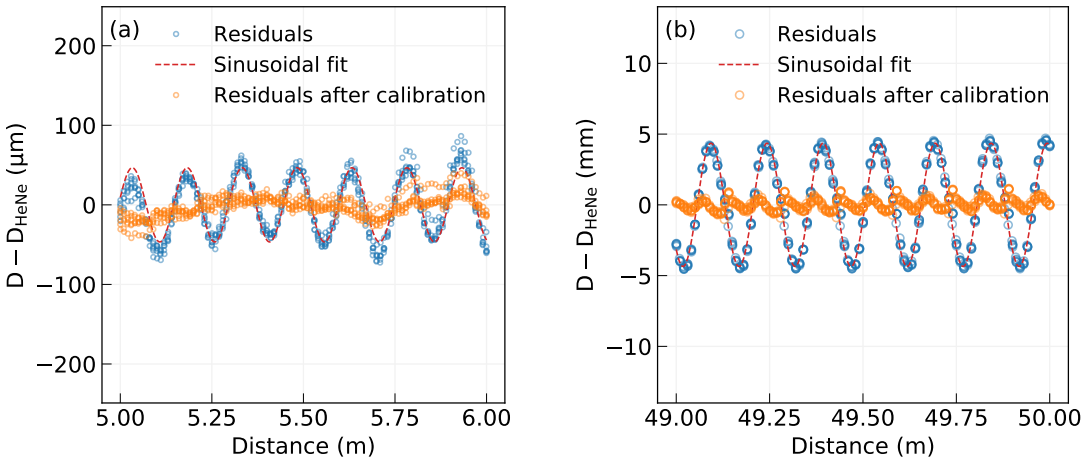

Figure 5.8. Residuals between the measured and reference (interferometer) distances for (a) 5-6 m, (b) 49-50 m, before and after calibration with a sinusoidal fit

Fig. 5.8 shows residuals within 100 µm for 5–6 m and 5 mm for 49–50 m. However, these large residuals are dominated by clearly systematic, sinusoidal error patterns with

a period of around 15 cm. This agrees with the range ambiguity corresponding to the 1 GHz beat note used for our experiments. Such errors are well known as 'cyclic deviations' from conventional phase-based electro-optic distance measurement [1]. They primarily arise from electrical cross-talk from the RF oscillator or the mixing of spurious optical reflections of the measurement beam and represent one of the main sources of correctable systematics in such phase-based measurement systems. We apply a simple calibration-based correction by fitting a single sinusoidal function to the residuals. The residuals remaining after subtraction of this calibration function indicate a measurement accuracy (root mean square error) of 12 µm for 5 to 6 m and 0.4 mm for 49 to 50 m, with potential for further correction as suggested by the remaining systematics[106]. Nevertheless, a post-calibration accuracy on the order of 10^{-5} is achieved already with this first prototypical measurement system for distances up to 50 m.

5.3.3. Hyperspectral laser scanning

In this part, we present the geometric point cloud and spectral information obtained from scanning the wooden target specimen shown in Fig. 5.3(b). We also show the preliminary results of a purely spectrum-based material classification within the point cloud. The target specimen was scanned from a distance of 5 m. About 3200 data points were acquired in a continued raster scanning pattern, with 1.7 mrad vertical and horizontal angular resolution. We chose this configuration as a compromise between high spatial resolution for resolving the geometrical features and low resolution for quick data acquisition and low memory needs. The 3D point cloud displaying the target geometry is shown in Fig. 5.9(a), where the z-coordinate represents the distance deviations measured from the instrument and the x-y plane is approximately parallel to the background surface. The geometrical features are accurately captured in our scan showing the 25 mm thickness of the ETH letters made of beech and the 10 mm thickness of the balsa bars. The points not conforming to any of the wood samples (mixed pixels) are typical artifacts of laser scanning that occur due to the partial overlap of the beam with regions of the target specimen at different depths [5].

As mentioned earlier, we use a CCD-based spectrometer to capture the hyperspectral reflection spectrum from the target surface within the initial investigation, herein. The reflection spectrum was acquired with 0.16 nm resolution over the entire spectral range of the SC. Although the intensity of the beat note observations is independent of any changes in the ambient illumination conditions, the measurements on the spectrometer are affected by background illumination. The background spectrum observed on the spectrometer was corrected before scanning and ambient light conditions were kept stable during the scanning process. Background correction can be performed regularly for fluctuating environmental illumination if necessary. An active HSL that is unaffected by ambient light fluctuations may be achieved by replacing the CCD-spectrometer with an array of high-speed photodetectors corresponding to individual spectral bands or by sequentially probing over the entire spectral range using tunable optical filters at the cost of scanning speed [73].

We used the entire set of wavelengths (features) between 570–970 nm. The mixed pixels have been temporarily filtered out from the data for training the classifier model.

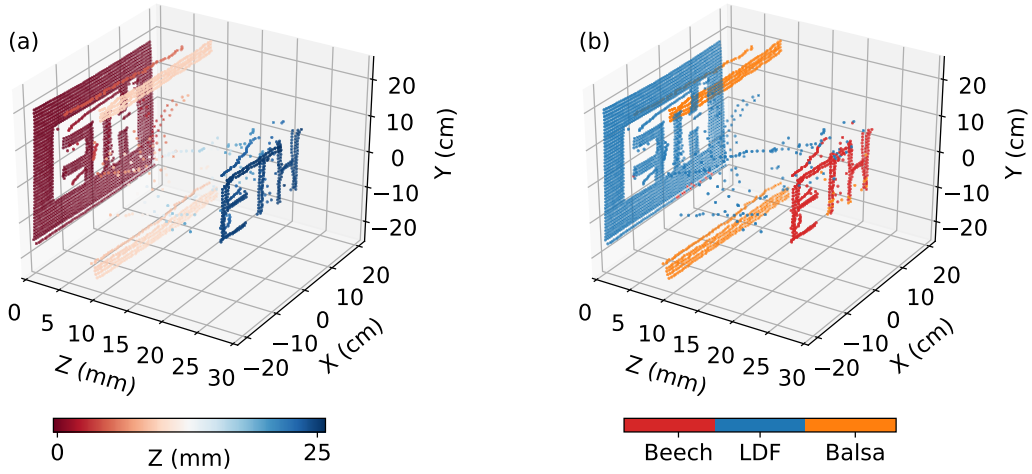

Figure 5.9. 3D point cloud of the wooden target showing (a) geometrical (range) profile, and (b) material classification using spectral information. z-axis represents the range information for the target placed in the x-y plane

Since the spectral properties are likely to be correlated for the neighboring areas on a single piece of wood, for a more independent evaluation we chose a test/train subset that corresponds to spatially different areas of the point cloud instead of using randomly split subsets. The data points on the lower balsa and left half (where $X < 0$) of the beech and LDF are used as a training set while the remaining data is used for testing. The class weights are balanced based on the relative frequencies of the classes in the training data and are then fed to a linear support vector machine (SVM)-based classifier [107]. A 5-fold cross-validation (CV) is used to tune the hyperparameters and evaluate the general performance of the classifier. The classification accuracy is around 96% (CV accuracy is 0.96 with a standard deviation of 0.01). Fig. 5.9(b) illustrates the classified point cloud showing the different material classes, i.e. beech, LDF, and balsa, on all the acquired points (including mixed pixels) demonstrating accurate classification of the wood varieties using their backscattered reflection spectrum. Fig. 5.10 shows the workflow of the classification approach.

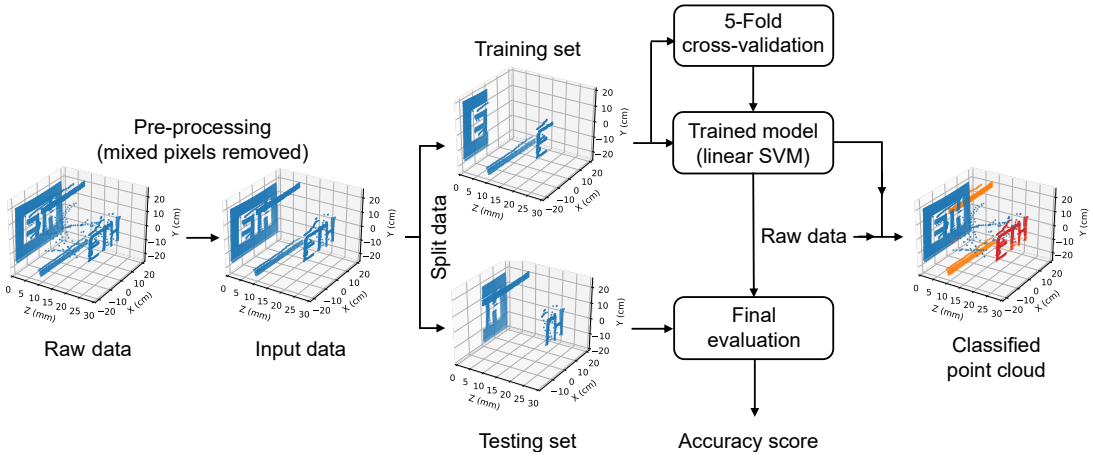

Figure 5.10. Workflow of the classification approach

A comprehensive evaluation of the classification accuracy would require a large number of independent and diverse training datasets to test and evaluate on fully independent data. The results presented herein still highlight the potential feasibility of extending our high-precision supercontinuum-based hyperspectral LiDAR approach to scanning with point-cloud classification based on spectral signatures of the materials. The enhanced range precision together with hyperspectral information is also beneficial for accurately estimating the surface geometry and orientation of complex geometrical features, and for radiometric calibration of the acquired intensities [108].

5.4. Conclusion and Outlook

We have developed and demonstrated a supercontinuum-based hyperspectral LiDAR prototype capable of high precision ranging over 50 m using phase delay observations from 1 GHz intermode beat notes while capturing spectral information of the diffusely reflecting surfaces between 590–970 nm. For measurements averaged over 13 ms, we obtained standard deviations of the distance measurements of around 3 µm at 5 m, and 72 µm at 50 m on cardboard surface with 89% average reflectance. These standard deviations were found to be directly proportional to distance squared and indirectly proportional to reflectance for distances larger than about 10 m, and dominated by a noise floor of a few µm for strongly reflecting targets at shorter distances. Additionally, we confirmed that the precision is approximately proportional to the square root of the integration time (τ_w) over a large range of τ_w, and can be improved by averaging the measurements over a longer duration. Compared to measurements from a reference interferometer, we achieved a relative accuracy on the order of 10^{-5} for stand-off distances up to 50 m after mitigating cyclic errors using a simple sinusoidal model. Preliminary results also show the potential of acquiring hyperspectral 3D point clouds of a target and using its back-reflection spectrum for material classification. Further work is underway to assess the long-term stability of the prototype, analyze the impact of the angle of incidence on targets having a more complex geometry, and investigate the benefit of high-precision measurements for efficient surface reconstruction. Improving the portability of the current prototype will lead to a promising technological basis for outdoor remote sensing and 3D digitization applications.

5.5. Supplement 1

5.5.1. Design of the scanning unit

The developed scanning module allows accurate, repeatable, and achromatic beam steering to generate the hyperspectral point clouds in our experiments. Fig. 5.11 shows a picture and the schematic design of the scanning module, which primarily consists of an achromatic off-axis parabolic (OAP) mirror and a 4-inch diameter silver-coated planar scanning mirror (SM), along with other beam routing optics. The SM is mounted on a 2-axis gimbal for controlled beam steering. The supercontinuum laser beam is coupled from an optical bench below the scanning module containing the rest of the optoelectronics. A

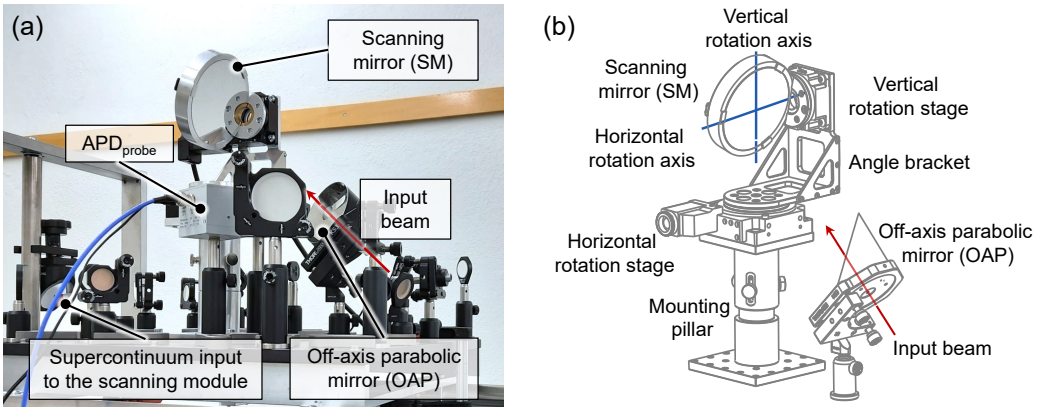

Figure 5.11. (a) Picture of the scanning module, (b) schematic design of the scanning unit showing the off-axis parabolic mirror and the scanning mirror mounted on a programmable 2-axis gimbal

3-inch surface diameter OAP mirror with a focal length of 6 inches and a 17.7 mm through-thickness hole is used to collect the back-scattered light onto the probe photodetector (APD_{probe}) and the spectrometer (see Fig. 5.2 in the primary document showing the schematic diagram of the experimental setup). The through-hole of the OAP is parallel to its optical axis to avoid beam distortion, and its diameter is optimized such that the back-scattered optical power is balanced between the losses encountered due to forward beam clipping and the collection efficiency. A slightly larger SM than the OAP is selected to ensure adequate light collection at high-deflection angles. A height-adjustable mounting pillar was used to elevate the SM above the remaining beam routing optics to increase the measurement field of view to around 180° horizontal and 90° vertical angle deflection without beam obstruction.

The flexibility and modularity of this prototype are designed as a compromise between its compactness, speed of operation, required accuracy, and development cost. The angular accuracy and scanning speed in our measurements are limited by the programmable 2-axis gimbal. The gimbal comprises of two motorized rotation stages to regulate the scanning mirror orientation around the horizontal (Standa 8MR190-2-28) and vertical axis (Standa 8MR151-1) respectively. The angular resolution of the stepper motors is around 0.01° and has a maximum rotation speed close to 50° per second i.e., around 8.33 rpm. The rotation stages are mounted perpendicularly to each other using a custom angle bracket such that the vertical and horizontal rotation axes intersect at the center of the SM where the input beam is directed. The minor residual offset between the SM and rotation axes causes systematic angular deviations, which can be modeled and calibrated through experimental observations. Nevertheless, the independently actuated programmable motor controllers facilitate achieving any desired scanning pattern. Moreover, target specimens can be scanned with varying pixel densities and data integration time. This feature can be particularly useful for analyzing mixed pixels where the beam can be traversed along the edges and corners of objects situated at different depths, and to evaluate the effect of beam waist on the apparent smoothing of the edges. Furthermore, the scanning flexibility would allow for increasing the point (or pixel) density to extract complex geometrical features and adapt the integration time for the required level of

precision.

The current scanning unit is 45 cm × 45 cm × 35 cm in size, weighs approximately 15 kg, and is built on top of a flat optical breadboard. Overall it lacks the portability for onsite and outdoor remote sensing applications and is presently only used in indoor laboratory conditions. Moreover, the scanning speed of the hardware (limited by the maximum operating speed of the motor controllers) is reasonable for laboratory-based analysis of static scenes, however would be time-consuming for scanning larger scenes.

5.5.2. Calibration

We calibrated the systematic angular deviations of the scanning unit to mitigate the errors originating from the offset in beam pointing and mechanical assembly of the 2-axis gimbal. A picture of the calibration setup is shown in Fig. 5.12. Initial experiments were conducted to reconstruct the true trajectory at different scanning angles by analyzing the beam projection on a checkerboard target placed at three different distances (as this is the minimal number of measurements required to quantify how well the measured projections describe the estimated beam trajectory).

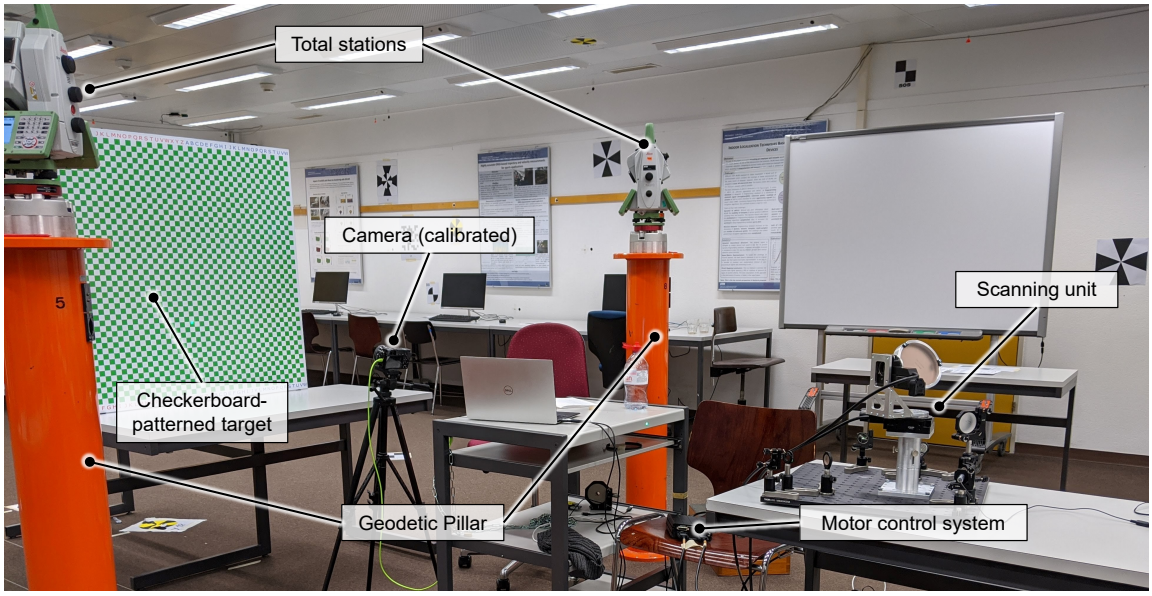

Figure 5.12. Measurement setup used to reconstruct the beam trajectory at different angles steered by the scanning unit. Two total stations, a calibrated camera, and a checkerboard target are used for calibration.

A camera (Sony-α6000) calibrated for radial and tangential lens distortions was used to extract the image coordinates of the projected laser spots on the checkerboard, where the corners of the squares forming the checkerboard pattern were used as reference points. By forward intersection of three marker points on the scanning unit and nine reference points on the target surface measured with two total stations (Leica Geosystems TS60, mounted on stable geodetic pillars), we ensured that the coordinates of the laser spots at the different positions of the target surface could be transformed into the same reference frame. A rigid body transformation was applied to the points extracted from the camera

images. The resulting coordinate system was defined by the scanning unit located at its origin with the orientation defined by its three marker points. The beam trajectory was determined from the projected points in this coordinate system using principal component analysis. Subsequently, the true position and orientation of the vertical and horizontal rotation axes (defined by the two rotation stages with respect to the SM) were estimated from the reconstructed beam paths for different azimuth (ϑ) and elevation (φ) angles. The resultant data is then used to calibrate the scanning unit by computationally adjusting the rotation angles in the scanning software to account for displacement errors of the SM as a function of ϑ and φ. An independent post-calibration test showed that angular deviations (calculated from actual beam direction) of less than about 0.2° were achieved within the entire field-of-view of our measurements.

6 | High-precision hyperspectral laser scanning for improved radiometric correction of backscatter intensity

Pabitro Ray, Tomislav Medić, David Salido-Monzú, and Andreas Wieser
Under review, 2023

(Author version)

Abstract

Radiometric information offers valuable insights into the surface and material properties of remote targets. Such information can be obtained along with the surface geometry by laser scanning. However, local variations in the surface geometry and orientation can introduce a bias in the radiometric data, related to the angle of incidence. We demonstrate a supercontinuum-based hyperspectral laser scanning approach for high-precision distance measurements, and its applicability to mitigate the angle of incidence effect by enabling an enhanced data-driven radiometric correction of the acquired intensities. Our experiments utilize a supercontinuum (SC) spectrally broadened to 570-970 nm from a 780 nm frequency comb. Distance measurements are derived from the differential phase delay of the intermode beat notes, while the backscattered reflection spectrum is captured using a commercial spectrometer over the spectral range of the SC output. We obtain hyperspectral point clouds with sub-mm range noise on natural targets (gypsum board and leaves of a plant used herein) placed at a distance of 5 m. The high-precision range measurements allow for correctly estimating the surface orientation and modeling the impact of the angle of incidence on the acquired radiometric data. The estimated model is applied to correct the acquired hyperspectral signatures, which are further exploited to compute various vegetation indices commonly used as plant health indicators. Our results illustrate enhanced information content on the direct 3D mapping of such spectral data of plant leaves with a reduced angle of incidence bias. These results highlight new opportunities for future research into remote sensing of vegetation and material probing with increased sensitivity.

6.1. Introduction

Laser scanners are extensively used in several applications such as industrial manufacturing, surveying, deformation monitoring, and remote sensing, where accurate three-dimensional (3D) geometric acquisition of the environment is essential [3, 5]. Commercially available terrestrial laser scanners (TLS) typically use a monochromatic light source. They can already provide sub-mm to cm level accuracy over ranges from a few meters to a few hundred meters, and an estimate of the surface reflectance of the target at the operating wavelength from the captured backscattered light intensity [4]. This radiometric information is practically useful for material probing and target identification. However, the gathered intensity is influenced by additional factors such as atmospheric conditions, sensor characteristics, surface properties, stand-off range, and angle of incidence, which consequently impact the estimated surface reflectance [109]. Traditionally, these effects are compensated by relying on the experimentally obtained calibration functions and direct or derived observations such as range and surface normals.

Compared to conventionally used monochromatic laser scanners, multi- or hyperspectral laser scanners (HLS) enable capturing the surface geometry of an object along with its spectral characteristics over a wider range of wavelengths. This makes HLS particularly interesting for enhanced target identification and material probing [94, 26, 21, 74]. For instance, dual- and multiwavelength solutions that can distinguish plant leaves from wood were shown to be effective for characterizing forest canopy structures [100, 99]. Such approaches use a combination of laser sources emitting different wavelengths, where the wavelengths were selected for the specific classification task. An active full-waveform HLS based on a supercontinuum (SC) source is also shown in the literature [24]. The authors used a SC source incoherently broadened from a pulsed laser and spanning from 450 to 1050 nm. A range precision of 11.5 mm over 20 m was achieved using direct time-of-flight (ToF) measurements on 16 spectral channels within the SC output spectrum. The approach was applied for accurately classifying mineral ores [25].

The broadband spectrum of the SC offers greater flexibility for selecting the wavelengths and allows extracting further information on the material properties. However, existing HLS technologies show mm to cm level range precision for distances over a few tens of meters [97, 101]. This reduced range precision as compared to the established commercial monochromatic instruments directly affects the geometric data quality and derived attributes, such as surface orientation or angle of incidence, which are necessary for effective radiometric calibration. Therefore, enhancing range precision is necessary for obtaining higher-quality structural and radiometric information.

We have recently demonstrated a SC-based HLS approach achieving sub-mm range precision for a stand-off distance up to 50 m [33]. The SC used in our experiments is coherently broadened to 570-970 nm from a 780 nm frequency comb. Distance measurements are estimated by monitoring the differential phase delay of the intermode beat notes generated upon direct photodetection of the SC. The spectrum of the light backscattered from the target is acquired using a commercial CCD-based spectrometer with a resolution of 0.16 nm over the SC output spectrum. The developed SC-HLS experimental setup provides high-precision ranging along with point-wise hyperspectral signatures of the scanned scene.

In this paper, we demonstrate how the proposed SC-HLS enables data-driven radiometric correction of intensity measurements for the effect of the angle of incidence (AoI). Our method leverages high-precision range measurements to achieve an improved estimation of the surface orientation and AoIs, necessary for mitigating this systematic influence. The latter was not deemed feasible with sufficient accuracy using the existing HLS approaches [110], and was only demonstrated for the cases where AoIs were provided with superior accuracy by additional rotation stage readings acquired at the position of the measured object [111].

We compare the geometrical quality of our point clouds with those obtained from a structured light scanner (used for ground-truth measurements) and with commercially available state-of-the-art TLSs that employ monochromatic light sources. The range performance of our measurements and the estimated AoIs are comparable to or better than those derived from the commercial instruments and, unlike those, supplemented by hyperspectral signatures at each data point. Relying on the estimated AoIs, we are able to apply a radiometric correction for individual spectral channels and achieve spectral signatures with a reduced AoI bias. We also demonstrate how the corrected hyperspectral data support accurate 3D mapping of vegetation indices, such as the normalized difference vegetation index (NDVI). Such indices are typically used as plant health indicators and were shown to be sensitive to AoI-related biases [112]. These results highlight the potential of our SC-HLS approach for remote sensing of vegetation. Nevertheless, the approach can be extended to a broader range of applications involving target identification and material probing.

This paper is structured as follows: Sec. 6.2 includes a brief description of the measurement principle and the experimental setup. The experimental results in terms of the range performance, radiometric correction, and the derived vegetation indices are presented in Sec. 6.3. Sec. 6.4 summarizes the primary contributions of this work, with directions for further research.

6.2. Experimental approach

Fig. 6.1 shows a schematic representation of our experimental setup. We use a SC source coherently broadened (Menlo Systems SCG1500) to a spectral range of 570-970 nm using a photonic crystal fiber (PCF) from a 780 nm mode-locked femtosecond laser (Menlo Systems C-fiber 780 SYNC100). The SC output power is around 26 mW integrated over the entire spectrum. The pulse-repetition rate (f_r) of the mode-locked laser (MLL) is set to 100 MHz, and a Rubidium (Rb)-frequency standard (SRS FS725) is used to provide accurate timing references to the MLL and acquisition electronics.

The reflective-type beam expander (RBE) increases the SC output beam to a diameter of 9 mm for better beam collimation over the optical path while minimizing chromatic aberration. A beam sampler (BSF) reflects about 10% of the SC power forming the reference arm, which is subsequently fed to the reference avalanche photodiode ($\mathrm{APD}^{\mathrm{ref}}$). The transmitted 90% of the optical power forms the probe arm and passes through the centered hole of an off-axis parabolic mirror (OAP) to reach the scanning mirror (SM).

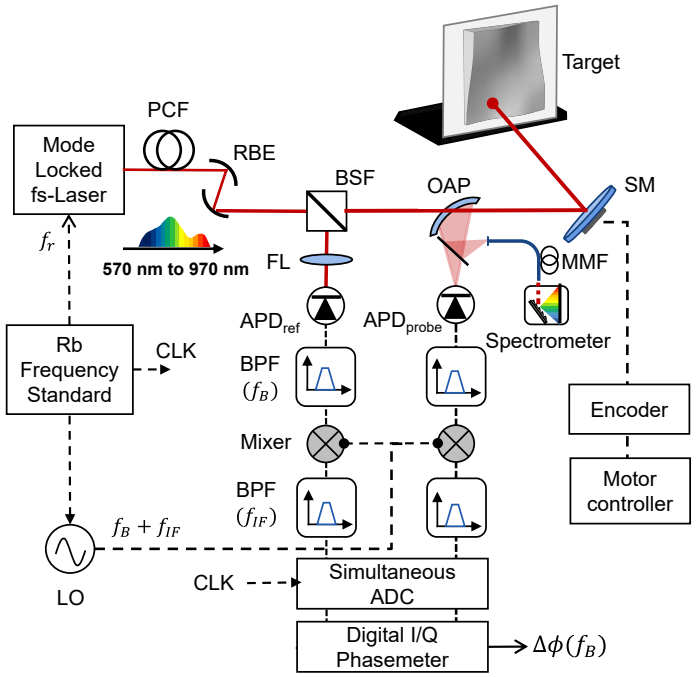

Figure 6.1. (a) Schematic representation of the experimental setup (PCF: photonic crystal fiber; RBE: reflective beam expander; BSF: beam sampler; OAP: off-axis parabolic mirror; SM: Scanning mirror; FL: focusing lens; APD: avalanche photodiode; MMF: multi-mode fiber; BPF: band-pass filter; LO: local oscillator; CLK: clock; ADC: analog-to-digital converter; I/Q: in-phase/quadrature).

The SM is placed on a programmable two-axis gimbal which allows accurately steering the beam to scan the target specimen. The details of the scanning module and its calibration are described in our previous work [33]. The backscattered light from the target is captured by the OAP and focussed onto the APD$^{\text{probe}}$. The -3 dB bandwidth of the APDs used in our experiments is 1 GHz.

The electrical beat notes generated at the APD are an integer multiple of f_r. Since a higher beat note frequency allows a higher measurement precision [28], we chose the 10^{th}-harmonic of f_r for distance measurements, i.e. $f_B = 1$ GHz. This choice was limited by the APD bandwidth. The selected beat note f_B is filtered using analog band-pass filters (BPF) centered at 1 GHz, and is then downconverted to an intermediate frequency of $f_{\text{IF}} = 400$ kHz before the analog-to-digital conversion (ADC). Both the reference and probe signals are concurrently digitized using a simultaneous-sampling ADC (Spectrum Instrumentation M4i.2234-x8). A digital in-phase/quadrature (I/Q) phasemeter retrieves the differential phase delay between the probe and reference signals, which is then used to estimate the distance to the target. The backscattered light is directed to a commercial CCD-based spectrometer (Thorlabs CCS175) to capture the reflection spectra of the target surfaces. These spectra are recorded with the maximum resolution (0.16 nm) of the spectrometer.

The measured distance (D) is estimated from the differential phase delay between the

probe and reference signals, as demonstrated in [30, 33]:

$$D = \frac{c}{2n_g f_B}\left(\frac{\phi^{\text{probe}} - \phi^{\text{ref}}}{2\pi} + N_M\right), \tag{6.1}$$

Here, c is the speed of light in vacuum, and n_g is the effective group refractive index estimated using a center-of-mass calculation for the observed optical power spectral density of the SC. The term $(\phi^{\text{probe}} - \phi^{\text{ref}})$ represents the differential phase delay $(\Delta\phi)$, accumulated on f_B. Here, N_M denotes the number of round trip range ambiguity cycles, where the range ambiguity is $(c/2n_g f_B)$.

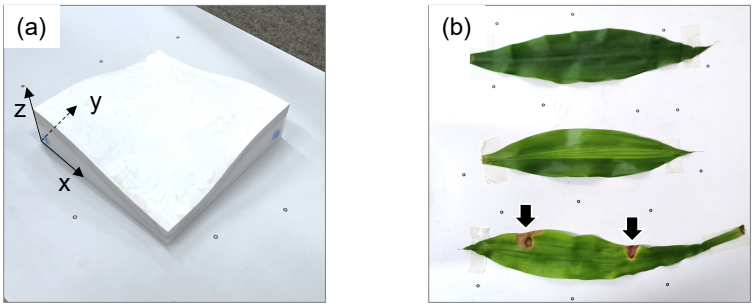

Figure 6.2. Pictures of the (a) doubly-curved target made of gypsum and (b) the leaves picked from a corn plant (dracaena fragrans, dry leaf spots as indicated by the arrows).

The test specimens used in our experiments are shown in Fig. 6.2. A rigid 16×16 cm^2 doubly-curved smooth surface made of gypsum, Fig. 6.2(a), is used to assess the range performance of our measurements. The doubly-curved surface has a maximum height difference of 2 cm (in the z-axis) across its surface. Fig. 6.2(b) shows the different leaves picked from a corn plant (dracaena fragrans) that are used to demonstrate direct 3D mapping of the acquired spectral data and the related derivatives. The leaves chosen herein are from the same plant. However, they partially differ in their size, shape (local curvatures), and radiometric properties, where their visual appearance (green chlorophyll content) and the presence of discolored regions act as health indicators. The leaves are attached to a 40×55 cm^2 large, flat wooden board. The board has been covered by a matt white varnish and provides mechanical stability during the experiments. All the experiments were conducted under controlled laboratory conditions at 20 °C, 955 to 958 hPa, and 50% relative humidity. Therefore, the impact of atmospheric fluctuations on the measurements can be neglected.

The measurement output for the i^{th} point of the scanning module is $(D_i, \vartheta_i, \varphi_i)$, where ϑ and φ are the azimuth and elevation angles of the scanning unit. The captured data is initially converted into 3D Cartesian coordinates x_i', y_i', z_i' with the calibrated center of the SM defined as the origin. The targets are placed vertically during measurements (Fig. 6.1) at the height of the SM with the main surface normal nearly coinciding with the line of sight. For further analysis, x_i', y_i', z_i' are transformed into x_i, y_i, z_i with the left bottom corner of the target as the origin, see Fig. 6.2(a), the z axis approximately parallel to the line of sight at the target center, and the xy-plane vertical in space. The

transformation is facilitated by exploiting the known relations (the line of sight vector direction, position, and orientation of the target) between the coordinate systems.

Moreover, the spectrometer acquires the point-wise backscattered light intensity $I_i'(\lambda)$ over the range of wavelengths (λ) of the SC output. The intensity values are affected by the angle of incidence (θ) and other systematic factors, which are not in the focus of this work. In a simplified approximation of the typically used LiDAR model [111], $I_i'(\lambda)$ can be expressed as:

$$I_i'(\lambda) \propto \eta(\lambda) g(D) I_0(\lambda) f_\rho(\lambda, \theta), \tag{6.2}$$

where, $\eta(\lambda)$ is the joint transmission and collection efficiency including the atmospheric and instrumental factors, $g(D)$ describes the dependence on measurement range to the target, $I_0(\lambda)$ is the intensity of the backreflected light at normal incidence, and $f_\rho(\lambda, \theta)$ represents the reflection coefficient (ρ) of the target as a function of θ and λ.

The acquired $I_i'(\lambda)$ is normalized to measurements obtained from a common background to eliminate the impact of $\eta(\lambda)$ and $g(D)$ which can be assumed as constant for an instrument at a fixed measurement range. This results in having $(x_i, y_i, z_i, I_i(\lambda))$ information for each scanned point, where $I_i(\lambda)$ is the normalized intensity.

The acquired $I_i(\lambda)$ is processed with a moving Gaussian kernel of 51 points to reduce the high-frequency noise of the individual channels. We chose a spectral range from 600 to 900 nm, taking into account the low signal-to-noise ratio (SNR) outside this range, resulting from the low power at the extreme edges of the SC spectrum available to us. We then subsample the data to a spectral resolution of 1 nm to reduce the number of spectral channels and thereby the computational time required for further analysis. Hence, λ represents the center wavelength of the individual spectral channels from 600 to 900 nm separated by 1 nm, i.e., there are 300 spectral observations in each $I_i(\lambda)$. We correct these hyperspectral signatures radiometrically and show their use for computing vegetation indices, in Sec. 6.3.2 and Sec. 6.3.3, respectively.

6.3. Results

6.3.1. Range performance

We use the doubly-curved gypsum specimen to evaluate the range performance of our measurements. The target specimen was placed at a stand-off range of 5 m. The SC beam hit the specimen approximately parallel to the z-axis, see Fig. 6.2(a), with a maximum deviation of 1.2°. For a non-moving beam fixed at a randomly selected position on the target, our measurements show an empirically estimated single-point precision of around 6 µm, evaluated from a time series of 100 measurement points each averaged over a data integration time of 13 ms. The 3D point cloud obtained by scanning the entire target was then compared with those obtained using two state-of-the-art commercial TLSs (Leica ScanStation P50, Z+F Imager 5016) and ground-truth observations from a structured light scanner (GOM Atos Core 300). The measurements using the commercial TLS were also carried out from a stand-off range of 5 m where the expected measurement precision

is around 300 µm as per instrument specifications. Due to the relatively short working range (< 1 m) of the structured light scanner (SLS), the ground-truth measurements were acquired at a stand-off range of only 0.4 m. The expected range precision of these measurements, according to instrument specifications, is at the µm level.

For our experiments, we chose a spatial point spacing of around 3 mm to sample the entire surface of the target. The SLS and TLS data were sub-sampled accordingly to a similar point spacing. The statistical outlier removal (SOR) algorithm [113] was applied to eliminate mixed pixels at the surface edges, and other artifacts. We aligned all the point clouds to the coordinate system of our measurements through transformations with 7 degrees of freedom (3 translations, 3 rotations, and scale) by using around 10 corresponding points selected in each dataset. The transformations were necessary for computing the comparable AOIs used in subsequent analyses.

The evaluation of the range performance involved locally fitting a surface using 1% of the total number of data points (26 points for HLS point cloud) within the neighborhood of each point, and computing the range residual of that point with respect to the fitted surface. The surface was approximated by a LOESS [114] regression method using second-order polynomials in the form of

$$z_i = p_1 x_i^2 + p_2 y_i^2 + p_3 x_i y_i + p_4 x_i + p_5 y_i + p_6 + \delta z_i, \tag{6.3}$$

where $p_{1,\cdots,6}$ are the locally estimated model parameters and x_i, y_i, z_i are the point cloud coordinates as described earlier in Sec. 6.2. The x_i and y_i are treated as error-free. Given the small angular range covered by the scans, the misfits δz_i are predominantly affected by the measurement range noise and can therefore be interpreted as range residuals. Fig. 6.3(a) shows the computed δz_i obtained from our measurements (SC-HLS), the SLS, and the two TLSs i.e., TLS^{a} and TLS^{b}.

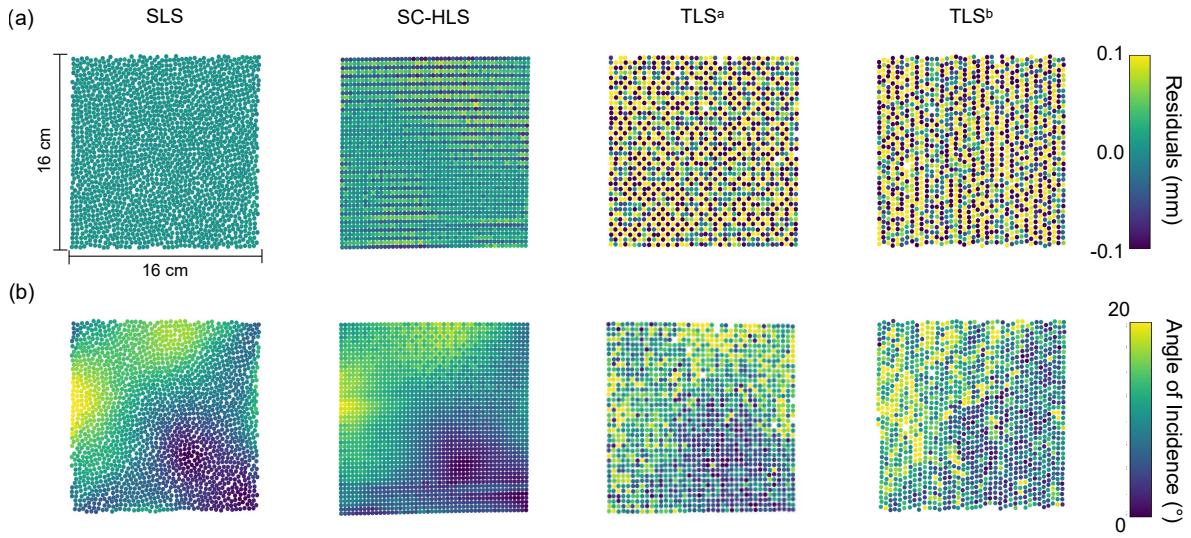

Figure 6.3. Comparison of the (a) range residuals and (b) angles of incidence obtained using different instruments.

It can be qualitatively observed from Fig. 6.3(a) that the range residuals are lower for the SC-HLS measurements than for the commercial TLS$^{a,\ b}$. However, they partially

exhibit some systematic variations. We expect these to be due to the remaining calibration errors of our scanning module, possibly slightly enhanced by power fluctuations and power-to-phase coupling effects at the APD. This will need to be investigated in the future. Nevertheless, the standard deviation of the residuals is around 4 µm for the SLS, 33 µm for SC-HLS, and around 163 and 178 µm for the two TLSs, thus indicating around 5 times better performance of the SC-HLS compared to the commercial terrestrial laser scanners at a range of 5 m.

To further assess the SC-HLS performance, the AoI (θ_i) at each data point was calculated as the angle between the line-of-sight and the normal vector of the locally fitted 3D surfaces. We calculated the normal vectors by principal component analysis (as implemented in the point-cloud library [115]), using the five nearest neighbors at each data point. This neighborhood size was chosen as a trade-off between ensuring an adequate level of detail and providing sufficient redundancy for the estimation. The estimated θ_i for the SC-HLS shown in Fig. 6.3(b) closely resemble the SLS observations and largely represent the actual surface curvature distribution, while the commercial TLSs exhibit notable noise superimposed on the real trends. To quantify the relative deviations, we calculated the difference of the estimated θ_i from the mean value ($\bar{\theta}_i$) within a neighborhood of 10 mm. The standard deviation of $\Delta\theta_i$ for the SLS data is around 0.3°, for SC-HLS around 0.7°, and for TLS[a, b] around 3.2°. These results indicate the benefits of high-precision scanning for correctly estimating the surface orientation which can lead to better surface reconstruction and is essential for radiometric correction of the spectral data as shown later in Sec. 6.3.2.

The relative impact of laser output power and data integration time on measurement precision across the different instruments is not accounted for in this work. For instance, commercial TLS technologies may as well achieve higher precision by adapting the integration time (slower scanning speed) and by using higher laser output power. The focus of this work is on demonstrating a potential solution to achieve precision laser scanning together with hyperspectral information.

6.3.2. Radiometric correction

As mentioned earlier, the SC-HLS approach can additionally acquire the reflection spectrum of the target surfaces across the SC output. Existing literature has demonstrated that AoI induces systematic biases in the estimated surface reflectance [112, 110, 111]. We carried out further experiments to demonstrate how SC-HLS can be used to reduce the AoI-related dependency on the gathered spectral data.

We acquired both geometrical and spectral information on the plant leaves placed at a range of 5 m using SC-HLS; the target specimen is shown in Fig. 6.2(b). The geometrical data were also acquired with SLS and TLS for comparison. We used one of the two commercial TLS instruments due to their comparable range performance, as shown in Sec. 6.3.1. To effectively demonstrate the impact of improved range precision on radiometric correction, relative to the existing HLS systems, we simulated a dataset (HLS$^{\text{sim}}$) exhibiting a higher range noise by adding a zero-mean Gaussian white noise having a standard deviation of 2 mm on our SC-HLS range data. We introduced a quasi-

randomly chosen mm-level range noise considering a range precision comparable to or better than that of the existing HLS systems. In this dataset, the contribution of the initial range noise of our measurements can be neglected as it is significantly lower than the simulated noise level (approximately 60 times).

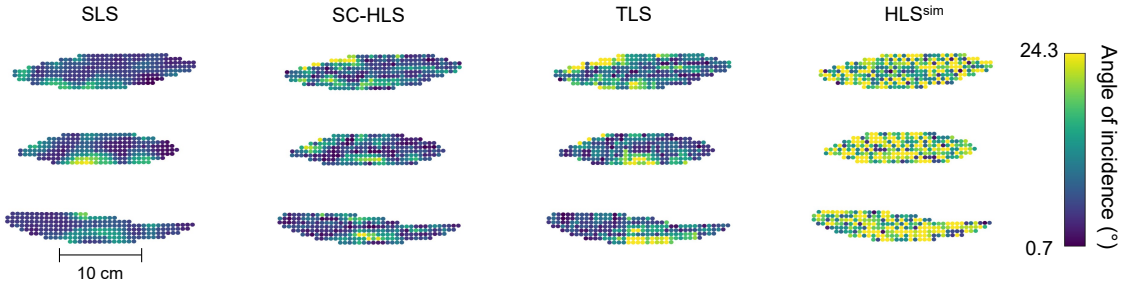

Figure 6.4. Comparison of the computed angle of incidence from the point cloud geometry for the different datasets

Fig. 6.4 illustrates the estimated θ_i on the plant leaves for the different datasets. They were computed as described earlier in Sec. 6.3.1. As compared to the simulated dataset HLS$^{\text{sim}}$, the SC-HLS and TLS measurements exhibit reasonable similarities to the ground-truth observations from the SLS. This is corroborated by evaluating the correlation coefficients with the SLS observations. The SC-HLS and TLS data exhibit a linear correlation coefficient of around 0.4 with the SLS data, whereas HLS$^{\text{sim}}$ indicates a value of 0.1.

To analyze the dependency of the measured intensity on AoI (see Eq. 6.2), we approximated their relationship by a radiometric correction function based on the combination of Lambertian and Beckmann scattering models for surfaces having both diffuse and specular properties as shown earlier in the literature [110, 111]. The radiometric correction function can be expressed as

$$I_i(\lambda) = I_0(\lambda) \cdot \left(k_d(\lambda) \cos\theta_i + \big(1 - k_d(\lambda)\big) \cdot \frac{e^{-\frac{\tan^2\theta_i}{m(\lambda)^2}}}{\cos^5\theta_i} \right) + \epsilon_i(\lambda), \tag{6.4}$$

where $I_0(\lambda)$ is the intensity at normal incidence and $k_d(\lambda)$ is a wavelength-dependent coefficient of the diffuse reflection having a value between 0 and 1. The parameter $m(\lambda)$ is related to the surface roughness of the target, and $\epsilon_i(\lambda)$ is an error term encompassing the random and systematic effects impacting $I_i(\lambda)$ that are not captured through the model in Eq. 6.4. The term $1 - k_d(\lambda)$ is the coefficient of the specular reflection. The parameters of the correction function were estimated using the robust M-estimator with Tukey's bisquare loss function [116] based on per point $I_i(\lambda)$ and $\theta_i(\lambda)$ values assuming homogeneous surface properties across the leaves; deviations from this assumption are the largest contributors to $\epsilon_i(\lambda)$.

Fig. 6.5 shows the estimated k_d values for each dataset (from Fig. 6.4). Since the SLS and TLS are monochromatic, we relied on the $I_i(\lambda)$ from SC-HLS for all datasets (related using nearest-neighbor interpolation). The estimated model parameters are affected by the respective θ_i observations and thus indirectly by the range noise. The k_d values derived from the SC-HLS and TLS data closely align with those derived using the geometric

ground truth SLS observations. In contrast, the HLS^{sim} data characterized by higher range noise leads to less accurate estimates. The other model parameters (I_0, m) exhibit comparable behavior.

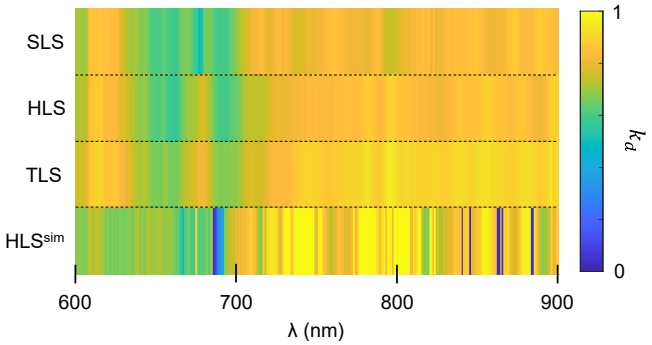

Figure 6.5. Comparison of coefficient of diffuse reflection (k_d) estimated from SC-HLS spectrum and geometry data from the various instruments.

We have determined the median absolute deviation of the estimated model parameters for SC-HLS, TLS, HLS^{sim} data from the reference SLS data, across different λ values. The differences of model parameters estimated from SC-HLS and SLS data are on average 40% lower than those estimated from TLS and SLS data, and 80% lower than the HLS^{sim} and SLS data. Fig. 6.5 further illustrates the wavelength dependency of k_d, which is consistent with the observations previously reported in the literature [111]. Although the spectral indices, often calculated as normalized differences of multiple spectral channels, exhibit reduced sensitivity to the influence of AoI, they cannot entirely eliminate its impact. These results therefore emphasize the necessity for correcting the AoI effect per spectral channel.

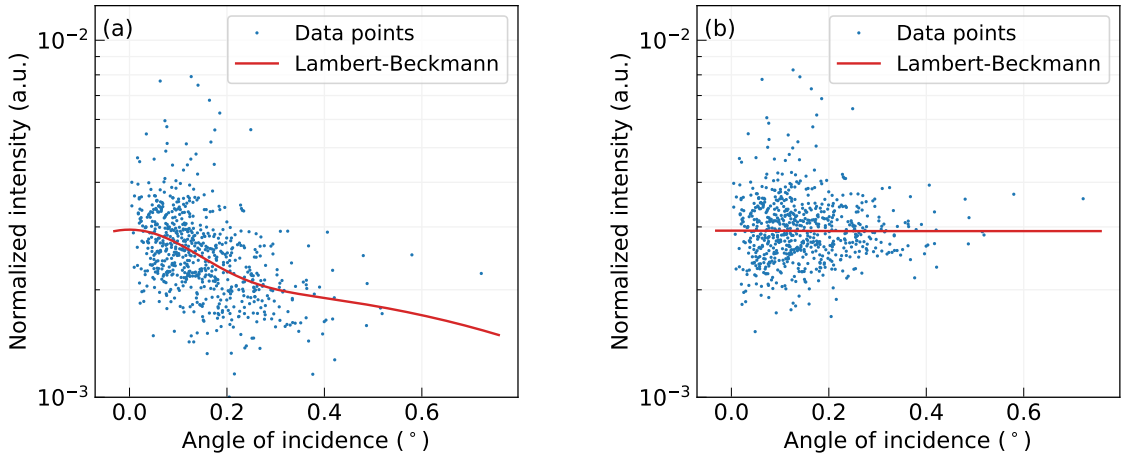

Figure 6.6. Normalized intensity observations for 790 nm with the fitted Lambert-Beckmann model (a) before, and (b) after radiometric correction

Fig. 6.6 shows an example of the correction function estimated using Eq. 6.4 for the SC-HLS point cloud at $\lambda = 790$ nm. Since the maximum deviation in θ_i is relatively small ($< 25°$) in our experiments, it contributes to only a portion of the overall variability within the I_i values, where $R^2 = 0.34$ in Fig. 6.6(a). Nevertheless, the data after correction

shown in Fig. 6.6(b) indicates that the implemented approach effectively eliminates any noticeable correlation between the I_i and θ_i values.

We further calculated the median absolute deviation of the I_i values before and after applying the correction functions for the respective datasets. Radiometric correction of the SC-HLS data reduced the average variability of I_i values by 23%, compared to 13% for the TLS data. However, the average variability of HLS^{sim} increased by 13%, suggesting that using the correction function based on inaccurate AoI estimates can even introduce further systematic biases rather than eliminating them. These results therefore demonstrate that the improved range precision of our SC-HLS measurements effectively mitigates the AoI-related bias in the acquired spectral data.

6.3.3. Relevance on the example of vegetation health monitoring

The hyperspectral signatures offer the flexibility to derive a number of vegetation indices (VIs) from a single spectrum. These indices are commonly used as indicators of physiological status related to plant health [117]. Tab. 6.1 shows several types of VI calculated from the I_λ observations that fall within the spectral range of our SC, along with a short description of their respective use cases [117, 118, 119]. For instance, higher normalized difference vegetation index (NDVI) values indicate a stronger presence of chlorophyll and thus healthier vegetation.

Table 6.1. Investigated vegetation indices (VIs) with an equation showing the spectral bands used for their computation and relevant use cases. NDVI: normalized difference vegetation index; RVI: simple ratio vegetation index; NDREI: normalized difference red edge index; FRI: fluorescence reflectance index; LCI: leaf chlorophyll index.

VI type	Calculated as	Use cases
NDVI	$(I_{800\ \text{nm}} - I_{650\ \text{nm}})/(I_{800\ \text{nm}} + I_{650\ \text{nm}})$	plant health, nutrition
RVI	$(I_{870\ \text{nm}}/I_{660\ \text{nm}})$	plant health, stress-level of crops
NDREI	$(I_{750\ \text{nm}} - I_{705\ \text{nm}})/(I_{750\ \text{nm}} + I_{705\ \text{nm}})$	indicative of mature, ripening crops
FRI	$(I_{600\ \text{nm}}/I_{690\ \text{nm}})$	chlorophyll fluorescence
LCI	$(I_{850\ \text{nm}} - I_{710\ \text{nm}})/(I_{850\ \text{nm}} + I_{680\ \text{nm}})$	chlorophyll content

Such indices have a reduced sensitivity to the AoI-related measurement bias, due to partially similar influence on different spectral channels. To eliminate the remaining residual bias, the channel-wise radiometric correction (as described in Sec. 6.3.2) is applied on I_λ before estimating the VIs. Tab 6.2 shows the correlation values (Spearmann's rank correlation) of the calculated VIs with AoI before and after applying the radiometric correction. For instance, the calculated NDVI values are initially significantly correlated ($\rho = 0.36,\ p \ll 0.001$) with the AoI before the radiometric correction. However, after the calibration, the correlation values reduce to $\rho = 0.02,\ p = 0.67$ demonstrating an effective correction. This is also observed for the other VIs (see Tab. 6.2), thus confirming that the AoI correction facilitated by the high-precision distance measurements supports the radiometric calibration of the acquired VIs.

Table 6.2. Correlation between the different vegetation indices (VI) and angle of incidence (AoI) before and after applying the radiometric correction. Here, ρ is Spearman's rank correlation coefficient, and the associated p-value indicates the statistical significance of the observed correlation.

VI type	ρ (before)	p-value (before)	ρ (after)	p-value (after)
NDVI	0.36	$\ll 0.001$	0.02	0.67
RVI	0.44	$\ll 0.001$	-0.03	0.44
NDREI	0.15	$\ll 0.001$	-0.01	0.80
FRI	0.26	$\ll 0.001$	$\ll 0.001$	0.95
LCI	0.15	$\ll 0.001$	-0.02	0.59

This effect is illustrated in Fig. 6.7 for NDVI and RVI point-wise mapped onto the acquired point clouds. Fig. 6.7 shows the corrected NDVI and RVI values, along with the differences in their respective observations ΔNDVI, ΔRVI before and after radiometric correction (indicating the associated errors). As anticipated, these differences ΔNDVI, ΔRVI show similar local variations as were observed in Fig. 6.4 for the AoIs. Although the absolute scale of the respective ΔVI is relatively small in our dataset compared to the VI values, their data spread corresponds to 13% of the overall spread of the NDVI values and 65% for the RVI values.

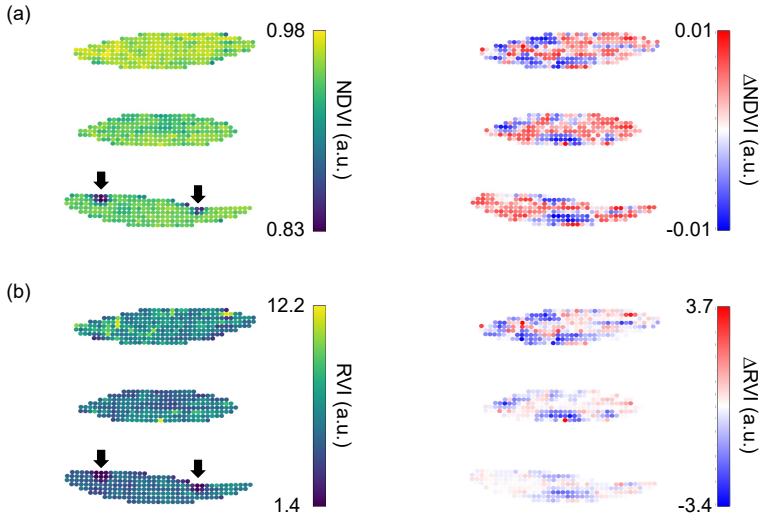

Figure 6.7. Point-wise mapping of the (a) NDVI and (b) RVI values calculated using the acquired hyperspectral information, along with their corresponding AoI-related corrections.

The calculated VI values also indicate adequate sensitivity to the leaf properties. A higher NDVI is observed for the visibly greener leaves, e.g., the topmost leaf in Fig. 6.2(b), despite only subtle differences between them in the RGB image. Additionally, we also recognize the dry leaf spots by lower NDVI and RVI values, see the marked arrows in Fig. 6.2(a) and Fig. 6.2(b). These results together highlight the potential of the developed SC-HLS approach for advanced plant health monitoring, which can also be further extended to enhanced material probing.

6.4. Conclusion and outlook

We presented a supercontinuum-based hyperspectral laser scanning approach capable of generating high-precision 3D geometrical information of a target with range residuals below 0.04 mm on natural surfaces placed at a range of 5 m. The advantages of precise distance measurements were demonstrated in the context of accurate estimation of the local surface geometry (orientation, surface normal, and angles of incidence). Our results show a data-driven approach for improved estimation of the surface orientation enabling reduced measurement biases in 3D mapping of spectral data through radiometric correction for the angle of incidence (AoI) effect, without prior knowledge of the surface orientation. We demonstrated the relevance of the achieved radiometric correction for correctly estimating various plant vegetation indices, such as normalized difference vegetation index (NDVI), with a reduced AoI-related bias. The developed approach can also be applied for improved material probing and automated point cloud classification.

7 | Conclusions

This thesis investigated the potential of coherently broadened optical supercontinuum (SC) sources for multi- or hyperspectral electro-optical distance measurements (EDM) suitable for long-distance applications. The research demonstrates a novel approach for, (i) multiwavelength EDM exploiting atmospheric dispersion to mitigate refractivity-induced errors, and (ii) hyperspectral LiDAR to gather precise geometric information along with a broadband spectral signature of natural targets. A brief overview of the background and existing literature was given in Chapter 2. Chapter 3 presented an experimental approach to multiwavelength EDM through spectral bands filtered from the SC [30]. Chapter 4 showed an improved experimental setup in terms of range performance and measurement stability and demonstrated the application of the multiwavelength EDM for dispersion-based inline refractivity correction [32]. While these chapters focused on measurements on cooperative targets (retroreflectors), Chapter 5 and 6 extended the approach to reflectorless targets, i.e. to natural surfaces and objects. The development of the hyperspectral LiDAR (HLS) and its range performance was presented in Chapter 5 [33]. Chapter 6 highlighted an application of the precise range information for improved radiometric correction of intensities, effectively reducing the angle of incidence bias [34]. These two chapters demonstrate the benefits of SC-based HLS for material probing, spectrum-based material classification, and remote sensing of vegetation. This chapter concludes the primary contributions by summarizing the gained knowledge, highlighting the main limitations, and providing an outlook on recommendations for future research.

7.1. Knowledge gained

The specific findings and insights from each research article (included in this thesis as Chapters 3–6) are elaborated within their respective conclusion sections above. The current section discusses the gained knowledge considering the overall goals and research questions outlined earlier in Sec. 1.2.

Supercontinuum as a basis for distance measurements: The thesis introduces the use of coherent SC sources for multi- or hyperspectral distance measurements, as a viable alternative to conventional EDM techniques which typically utilize a single wavelength narrow linewidth laser source. Benefiting from the frequency stability of a mode-locked fs laser, the research demonstrates that SC sources broadened from frequency combs can also be used to achieve highly precise distance measurements. Moreover, the broad bandwidth (a few hundred nm) of the SC enables spectral flexibility in selecting the number of wavelengths or spectral range for specific EDM or LiDAR applications as shown in this thesis. While previous studies reported in the literature have demonstrated the advantages and utility of frequency combs from mode-locked femtosecond lasers for

distance measurements, the use of SC sources has been relatively unexplored. Thus, the knowledge gathered from this thesis contributes toward highlighting the advantages and limitations of using SC for precise distance measurements, opening new opportunities for practical industrial applications and future research.

In particular, the utilization of intermode beats has proven to be effective in generating equally spaced modulation frequencies from a single source and at different spectral bands. The electrical beat notes eliminate the need for an external electronic radio-frequency (RF) modulator, thereby reducing the electromagnetic coupling issues and providing more flexibility in the electronic design of an EDM unit. The different spectral bands obtained from the same SC source eliminate the necessity of using multiple laser sources centered at different wavelengths. Using the phase-based measurement on the intermode beats, we evaluated the range performance in terms of precision and accuracy in the measurement conditions. Experimental results on cooperative targets showed an empirically estimated range precision of around 0.1 mm at 50 m, and a distance-dependent component below 0.2 ppm on individual spectral bands filtered from the SC. The observed value of the distance-dependent component indicates the potential to achieve sub-mm level precision over a few kilometers. It was also observed that overall the measurement precision could be further improved by using a longer data averaging time, primarily for timescales exhibiting white noise characteristics. Our measurements compared to a reference interferometer showed a relative accuracy on the order of 0.1 ppm for displacements up to 50 m, on a hollow retroreflector as a cooperative target. Through power spectral analysis of the distance observations and detected beat note amplitude, we identified phase errors arising from power and pointing fluctuations as the dominant sources of error in the measurements.

On diffuse targets i.e. natural surfaces, the empirically estimated range precision remained below 0.1 mm up to a stand-off range of 50 m for a target specimen with 89% surface reflectance; the relative accuracy was about 0.4 mm under the same conditions. The range precision showed a direct proportionality to the square of the distance and inverse proportionality to the surface reflectance. Similar to the measurements on cooperative targets, the precision exhibited an approximate proportionality to the square root of the data averaging time and thus could be further improved by averaging the measurements over a longer duration. These experimental results provide valuable insights into the potential use of SC for refractivity correction and LiDAR applications.

Application for inline refractivity correction: We demonstrated that distance measurements on two spectral bands filtered from a SC can be used for dispersion-based inline refractivity compensation. Considering the overall size and practical challenges of our experimental setup, a lab-based refraction modifying element was developed to test the performance of our approach within the lab, see Fig. 4.3(b). This refraction modifying element is a 9 m long sealed steel pipe that is connected to an electrical air pump to create pressure-induced refractivity changes inside the tube. It was designed to induce a substantial yet controlled refraction effect over short distances. The development process of this element also facilitated a better understanding of the effects of turbulence and beam bending on the measurements. Using this element, we were able to create an apparent distance change of around -0.4 mm in the measurement path.

The refractivity-corrected measurements estimated using the two-color method indicated that these apparent distance errors were effectively suppressed without using any external meteorological observation. The corrected distance measurements exhibited a standard deviation of less than 0.1 mm at 15 m when the optical path length change on the individual wavelengths was about −0.4 mm. The observed range performance was then extrapolated to assess its viability to longer practically useful ranges. Considering the distance-dependent component of the measurement precision modeled through our experiments, the two-color compensated measurements indicate the potential to achieve a precision better than 5 mm over a range of 500 m using a data averaging time of tens of ms. This precision could be further improved by employing even longer data averaging times. The study also investigated the fundamental and practical limitations of the approach, which were identified as phase errors caused by power and pointing stability. These results together provide valuable insights for the continued development of the methodology employed in this study.

Hyperspectral LiDAR: We demonstrated that our approach can enable 3D geometrical acquisition of natural targets with sub-mm to mm level range precision over a few tens of meters and acquire the hyperspectral reflectance of the target. The range performance was found to be better than the established hyperspectral LiDAR approaches. The SNR of the acquired signatures was shown to be adequate for spectrum-based material classification of targets.

By employing a data-driven approach, we illustrate that highly precise range observations contribute to a more accurate estimation of surface orientation and angle of incidence. This, in turn, enables an enhanced radiometric correction of intensities by mitigating the angle of incidence effect, which was previously constrained by the range precision of established methods. The resulting radiometrically corrected observations enabled precise point-wise mapping of vegetation indices on the acquired 3D point cloud of plant leaves. We explored the benefits of this approach for remote sensing of vegetation, with potential applications in enhanced material probing.

7.2. Limitations

Experimental complexity and instrumental effects: The process of spectral broadening through photonic crystal fibers is intrinsically susceptible to variations in laser pointing into the fiber and thermal effects on the fiber. These effects induce temporal fluctuations in the laser output spectrum. The achievable range performance of our measurements was constrained by the inherent noise contributions arising from these effects. As mentioned earlier, our measurements were affected by phase errors originating at the photodetector. These phase errors were primarily caused by optical power and pointing fluctuations resulting from the temporal fluctuations in the laser output, as well as atmospheric effects encountered for measurements over longer distances. While we reduced these effects through measures developed based on the results of experimental investigations, the posed challenges hindered our ability to fully realize the performance limits of our approach.

The processing time for each data point on our lab PC[1] ranged from about 0.8 s to 1.5 s, depending on the underlying sampling rate (approximately 78 MS/s) and number of samples (about 1 to 2 million, which corresponds to an acquisition time of 13 ms or 27 ms respectively for each data point). The much longer data processing time compared to the acquisition window currently poses a limitation on real-time data acquisition speed. Nevertheless, the processing speed could be substantially improved by more powerful and dedicated hardware. The scanning speed of the developed hyperspectral LiDAR was around 0.8 s per point, i.e. much slower than commercial terrestrial laser scanners. For example, scanning about 3200 data points on the wooden target specimen, see Fig. 5.3(b), took around 42 minutes. While the scanning module proved effective for laboratory use, its design needs further adaptation for applications involving the scanning of a large number of points, particularly in scenarios demanding rapid acquisition of the 3D surface geometry. Since the processing and scanning speed constraints are not fundamental limitations of the approach, our investigation did not prioritize the optimization of this aspect. Nevertheless, such optimization could have facilitated additional explorations into the performance and potential of the developed experimental units for practical applications.

The CCD spectrometer-based approach used in our hyperspectral LiDAR requires frequent correction of the background illumination and an adequate optical SNR of the backscattered light. Although the intensity of beat notes remains unaffected by ambient illumination, the spectrometer measurements can be influenced by rapidly fluctuating light conditions that are faster than the background correction. A fully active multi-spectral LiDAR could be achieved by replacing the CCD spectrometer with an array of high-speed photodetectors, each corresponding to an individual spectral band [73]. However, it would increase the overall cost and complexity of the experimental design.

Lack of investigation in outdoor conditions: Due to the current size and technical constraints of our experimental setup, our measurements were confined to laboratory conditions. Investigations under outdoor conditions would be beneficial for real-world applications (such as early deformation monitoring of large structures) and for evaluating the influence of potential environmental factors on our measurements. This may provide additional insights into the performance and robustness of our approach beyond controlled laboratory conditions.

For instance, the refractivity changes were replicated in a laboratory setting using a refraction-modifying element. Similarly, the targets used for hyperspectral laser scanning were limited to a few test specimens. To evaluate the impact of longer distances, we extrapolated the scale of the underlying uncertainties by modeling the impact of distance and distance-dependent effects that may be expected for practical conditions. Since these models are derived from experimental observations in a well-controlled environment they do offer some insights into the performance over longer ranges, however they may not encompass all distance-dependent phenomena, particularly those related to performance degradation in more turbulent media. Therefore further investigation is necessary to evaluate the performance of our experimental approach in practical outdoor conditions.

[1]Processor: Intel(R) Xeon(R) CPU E5-2609 v2 2.50 GHz, 4 cores; RAM: 28 GB; 64-bit operating system

7.3. Outlook

Potential solutions for improving the range performance: The range performance in terms of precision and accuracy is a crucial consideration in this study, and exploring potential factors to improve this performance is essential. A prospective solution to improve the measurement precision could be utilizing even higher-order beat notes. For example, using 10 GHz beat notes instead of 1 GHz may improve the range precision. Such improvements have already been reported in the literature [28]. Although a higher bandwidth photodetector incurs additional costs, the resulting improved range precision not only enhances the performance of refractivity-compensated distance measurements but also facilitates improved geometrical mapping. Additionally, exploring experimental solutions to mitigate cyclic errors introduced by electromagnetic coupling could be valuable in improving the measurement accuracy [87].

Moreover, addressing the impact of power and phase conversion effects on the photodetector is important, particularly for practical outdoor applications where higher power and pointing fluctuations are anticipated. Existing techniques proposed in the literature for suppressing [89] and characterizing [79] these effects should be further investigated. Recent advancements in the generation of ultra-low noise SC sources [92] may also contribute towards reducing the phase errors caused by inherent power instabilities.

Outdoor measurements for inline refractivity correction: Measurements under outdoor conditions for extended periods will contribute to a more robust understanding of the method's performance and limitation for achieving high precision EDM over several hundred meters in practical conditions. Outdoor measurements may require optimizing the experimental setup and detection stages against higher exposures of ambient light and thermal effects.

Given that the impact of refractivity variations on distance errors becomes more pronounced over long distances, it may be essential to explore effective solutions for addressing the larger power and pointing fluctuations as mentioned earlier. Ensuring the balance between laser output power and range performance, while considering eye safety, is also necessary for outdoor applications. These investigations may help in determining whether this approach can be a practical solution for refractivity compensation in field conditions.

Developing compact and portable systems: While compact and portable systems are not prerequisites for outdoor measurements, their availability could facilitate practical onsite studies in diverse environmental conditions. Developing such systems would require adapting the experimental design and incorporating miniaturized optoelectronic devices that are not only compact but also durable and robust for outdoor use. Further investigations into instrument calibration and stability aspects may also be necessary.

A portable unit extends the potential applications of multiwavelength EDM for monitoring small geological changes in mountainous terrain. In the context of hyperspectral LiDAR, a portable unit facilitates investigating the technology for further applications such as large-scale deformation monitoring, characterizing forest canopy structures, and mineral detection. The development of compact and portable systems thus generates new possibilities for applications across different fields.

A | Bibliography

[1] J. M. Rüeger. *Electronic Distance Measurement - An Introduction, 3rd Ed.* Springer, 1990.

[2] G. Berkovic and E. Shafir. Optical methods for distance and displacement measurement. *Advances in Optics and Photonics*, 4(4):441–71, 2012.

[3] M.C. Amann, T. Bosch, R. Myllyla, and M. Rioux. Laser ranging: a critical review of usual techniques for distance measurement. *Optical Engineering*, 40(1):10–19, 2001.

[4] G. Vosselman and H.G. Maas. *Airborne and terrestrial laser scanning.* CRC Press, 2010.

[5] B. Riveiro and R. Lindenbergh. *Laser scanning: An emerging technology in structural engineering (1st ed.).* CRC, 2019.

[6] M. Zámečníková, A. Wieser, H. Woschitz, and C. Ressl. Influence of surface reflectivity on reflectorless electronic distance measurement and terrestrial laser scanning. *Journal of Applied Geodesy*, 8(4):311–325, 2014.

[7] H. Barrell and J.E. Sears. The refraction and dispersion of air for the visible spectrum. *Philosophical Transactions of the Royal Society of London*, 786(238):1–64, 1939.

[8] B. Edlén. The refractive index of air. *Metrologia*, 2:71–79, 1966.

[9] G. Bönsch and E. Potulski. Measurement of the refractive index of air and comparison with modified edlén's formulae. *Metrologia*, 35(2):133–139, 1998.

[10] P.E. Ciddor. Refractive index of air: new equations for the visible and near infrared. *Applied Optics*, 35(9):1566–73, 1996.

[11] P.E. Ciddor and R.J. Hill. Refractive index of air. 2. group index. *Applied Optics*, 38(9):1633–67, 1999.

[12] F.K. Brunner and J.M. Rüeger. Theory of the local scale parameter method for EDM. *Bulletin Géodésique*, 66:355–64, 1992.

[13] F. Pollinger, T. Meyer, J. Beyer, N.R. Doloca, W. Schellin, W. Niemeier, J. Jokela, P. Hakli, A. Abou-Zeid, and Meiners-Hagen K. The upgraded PTB 600 m baseline: a high-accuracy reference for the calibration and the development of long-distance measurement devices. *Measurement Science and Technology*, 23(094018):1–11, 2012.

[14] P.L. Bender and J.C. Owens. Correction of optical distance measurements for the fluctuating atmospheric index of refraction. *Journal of Geophysical Research*, 70(10):2461–62, 1965.

[15] A.N. Golubev and A.M. Chekhovsky. Three-color optical range finding. *Applied Optics*, 33(31):7511–17, 1994.

[16] S. Xiong, Y. Wang, J. Chen, J. Zhang, and G. Wu. Multi-color method for the self-correction of the air refractive index. *Optics Letters*, 46(15):3785–88, 2021.

[17] K.B. Earnshaw and J.C. Owens. A dual-wavelength optical distance measuring instrument which corrects for air density. *IEEE Journal of Quantum Electronics*, 3(11):544–550, 1967.

[18] J. C. Owens. The use of atmospheric dispersion in optical distance measurement. *Bulletin Geodesique*, 89(1):277–291, 1968.

[19] G.R. Huggett. Two-color terrameter. *Developments in Geotectonics*, 16:29–39, 1981.

[20] J. Gervaise. First results of the geodetic measurements carried out with the terrameter, two wavelength electronic distance measurement instrument. In *Proc. Geodätischen Seminar Über Electrooptische Präzisionsstreckenmessung*, pages 213–29, 1983.

[21] J.U.H. Eitel, B. Höfle, L.A. Vierling, A. Abellán, G.P. Asner, J.S. Deems, C.L. Glennie, P.C. Joerg, A.L. LeWinter, T.S. Magney, G. Mandlburger, D.C. Morton, J.Müller, and K.T. Vierling. Beyond 3-d: The new spectrum of lidar applications for earth and ecological sciences. *Remote Sensing of Environment*, 186:372–392, 2016.

[22] J. Sun, S. Shi, W. Gong, H. Yang, L. Du, S. Song, B. Chen, and Z. Zhang. Evaluation of hyperspectral LiDAR for monitoring rice leaf nitrogen by comparison with multispectral LiDAR and passive spectrometer. *Scientific Reports*, 7(40362):637–41, 2017.

[23] J.T. Mundt, D.R. Streuker, and N.F. Glenn. Mapping sagebrush distribution using fusion of hyperspectral and lidar classifications. *Photogramm. Engg. and Remote Sensing*, 72(1):47–54, 2006.

[24] T. Hakala, J. Suomalainen, S. Kaasalainen, and Y. Chen. Full waveform hyperspectral LiDAR for terrestrial laser scanning. *Optics Express*, 20(7):7119–27, 2012.

[25] Y. Chen, C. Jiang, J. Hyyppä, S. Qiu, Z. Wang, M. Tian, W. Li, E. Puttonen, H. Zhou, Z. Feng, Y. Bo, and Z. Wen. Feasibility study of ore classification using active hyperspectral LiDAR. *IEEE Geoscience and Remote Sensing Letters*, 15(11):1785–89, 2018.

[26] M.A. Powers and C.C. Davis. Spectral LADAR: active range-resolved three dimensional imaging spectroscopy. *Applied Optics*, 51(10):1468–78, 2012.

[27] J. Ye. Absolute measurement of a long arbitrary less distance to less than an optical fringe. *Optics Letters*, 29(10):1153–55, 2004.

[28] N. R. Doloca, K. Meiners-Hagen, M. Wedde, F. Pollinger, and A. Abou-Zeid. Absolute distance measurement system using a femtosecond laser as a modulator. *Measurement Science and Technology*, 21(11):115302–9, 2010.

[29] S. W. Kim. Combs rule. *Nature Photonics*, 3:313–314, 2009.

[30] P. Ray, D. Salido-Monzú, and A. Wieser. High-precision intermode beating electro-optic distance measurement for mitigation of atmospheric delays. *Journal of Applied Geodesy*, 17(2):93–101, 2023.

[31] D. Salido-Monzú and A. Wieser. Simultaneous distance measurement at multiple wavelengths using the intermode beats from a femtosecond laser coherent supercontinuum. *Optical Engineering*, 57(4):044107, 2018.

[32] P. Ray, D. Salido-Monzú, R. Presl, J.A. Butt, and A. Wieser. Refractivity corrected distance measurement using the intermode beats derived from a supercontinuum. *Optics Express*, 32(7):12667–12681, 2024.

[33] P. Ray, D. Salido-Monzú, S.L. Camenzind, and A. Wieser. Supercontinuum-based hyperspectral LiDAR for precision laser scanning. *Optics Express*, 31(20):33486–33499, 2023.

[34] P. Ray, T. Medić, D. Salido-Monzú, and A. Wieser. High-precision hyperspectral laser scanning for improved radiometric correction of backscatter intensity. *Under review*, 2023.

[35] T. Medić, P. Ray, Y. Han, G.A.L. Broggini, and S. Kollart. Remotely sensing inner fruit quality using multispectral LiDAR: estimating sugar and dry matter content in apples. *under review, pre-print available at SSRN 448827*, 2023.

[36] H. Maar and H. Zogg. WFD-wave form digitizer technology. *White Paper on the Leica Nova*, MS50(506), 2014.

[37] K. Meiners-Hagen and A. Abou-Zeid. Refractive index determination in length measurement by two-colour interferometry. *Measurement Science and Technology*, 19(084004):1–5, 2008.

[38] F. Pollinger. Refractive index of air. 2. group index: comment. *Applied Optics*, 59(31):9771–72, 2020.

[39] K.B. Earnshaw and E.N. Hernandez. Two-laser optical distance-measuring instrument that corrects for the atmospheric index of refraction. *Applied Optics*, 11(4):749–54, 1972.

[40] L.E. Slater and G.R. Huggett. A multiwavelength distance-measuring instrument for geophysical experiments. *Journal of geophysical reseaerch*, 81(35):6299–6306, 1976.

[41] B. Querzola. High accuracy distance measurement by two-wavelength pulsed laser sources. *Applied Optics*, 1979:3035–47, 1979.

[42] T. Udem, R. Holzwarth, and T.W. Hänsch. Optical frequency metrology. *Nature*, 416:233–237, 2002.

[43] T. Fortier and E. Baumann. 20 years of developments in optical frequency comb technology and applications. *Communications Physics*, 2(153):1–16, 2019.

[44] A.D. Ludlow, M.M. Boyd, J. Ye, E. Peik, and P.O. Schmidt. Optical atomic clocks. *Reviews of Modern Physics*, 87(637), 2015.

[45] S.A. Diddams, A. Bartels, T.M. Ramond, C.W. Oates, S. Bize, E.A. Curtis, J.C. Bergquist, and L. Hollberg. Design and control of femtosecond lasers for optical clocks and the synthesis of low-noise optical and microwave signals. *IEEE Journal of Selected Topics in Quantum Electronics*, 9(4):1072–80, 2003.

[46] R.A. McCracken, J.M. Charsley, and D.T. Reid. A decade of astrocombs: recent advances in frequency combs for astronomy [invited]. *Optics Express*, 25(13):15057–78, 2017.

[47] N. Picqué and T.W. Hänsch. Frequency comb spectroscopy. *Nature Photonics*, 13:146–157, 2019.

[48] Y.S. Jang and S.W. Kim. Distance measurements using mode-locked lasers: A review. *Nanomanufacturing and metrology*, 1:131–47, 2018.

[49] J. M. Dudley, G. Genty, and S. Coen. Supercontinuum generation in photonic crystal fiber. *Reviews of Modern Physics*, 78(4):1135–83, 2006.

[50] J.M. Dudley and J.R. Taylor. Ten years of nonlinear optics in photonic crystal fiber. *Nature Photonics*, 3:85–90, 2009.

[51] P. Russell. Photonic crystal fibers. *Science*, 299(5605):358–62, 2003.

[52] K.L. Corwin, N.R. Newbury, J.M. Dudley, S. Coen, S.A. Diddams, K. Weber, and R.S. Windeler. Fundamental noise limitations to supercontinuum generation in microstructure fiber. *Physical Review Letters*, 90(11):113904–1–4, 2003.

[53] K. Minoshima and H. Matsumoto. High-accuracy measurement of 240-m distance in an optical tunnel by use of a compact femtosecond laser. *Applied Optics*, 39(30):5512–5517, 2000.

[54] H. Matsumoto, K. Minoshima, and S. Telada. High-precision long-distance measurement using a frequency comb of a femtosecond mode-locked laser. In *SPIE proceedings on Recent Developments in Traceable Dimensional Measurements*, volume 5190, pages 308–315, 2003.

[55] K. Minoshima, T.R. Schibli, H. Matsumoto, Y. Lino, K. Yoshino, and K. Kumagai. Ultrahigh dynamic-range portable distance meter using an optical frequency comb. *Conference on Lasers and Electro-Optics*, pages 1–2, 2006.

[56] S. Hyun, Y.J. Kim, Y. Kim, J. Jin, and S.W. Kim. Absolute length measurement with the frequency comb of a femtosecond laser. *Measurement Science and Technology*, 20(095302), 2009.

[57] P. Balling, P. Kren, P. Masika, and S.A. van den Berg. Femtosecond frequency comb based distance measurement in air. *Optics Express*, 17(11):9300–13, 2009.

[58] M. Cui, M.G. Zeitouny, N. Bhattacharya, S.A. van den Berg, H.P. Urbach, and J.J.M. Braat. High-accuracy long-distance measurements in air with a frequency comb laser. *Optics Letters*, 34(13):1982–84, 2009.

[59] J. Lee, Y.J. Kim, K. Lee, S. Lee, and S.W. Kim. Time-of-flight measurement with femtosecond light pulses. *Nature Photonics*, 4:716–720, 2010.

[60] I. Coddington, W.C. Swann, L. Nenadovic, and N.R. Newbury. Rapid and precise absolute distance measurements at long range. *Nature Photonics*, 3:351–356, 2009.

[61] H. Wu, T. Zhao, Z. Wang, K. Zhang, B. Xue, J. Li, M. He, and X. Qu. Long distance measurement up to 1.2 km by electro-optic dual-comb interferometry. *Applied Physics Letters*, 111(251901):1–5, 2017.

[62] K. Meiners-Hagen, T. Meyer, G. Prellinger, W. Pöschel, D. Dontsov, and F. Pollinger. Overcoming the refractivity limit in manufacturing environment. *Optics Express*, 24(21):24092–24104, 2016.

[63] K. Minoshima, K. Arai, and H. Inaba. High-accuracy self-correction of the refractive index of air using two-color interferometry of optical frequency comb. *Optics Express*, 19(27):26095–26105, 2011.

[64] S. van den Berg, S. van Eldik, and N. Bhattacharya. Mode-resolved frequency comb interferometry for high-accuracy long distance measurement. *Scientific reports*, 5(14661):1–10, 2015.

[65] G. Wu, M. Takahashi, K. Arai, H. Inabe, and K. Minoshima. Extremely high-accuracy correction of air refractive index using two-colour optical frequency combs. *Scientific reports*, 3(1894):1–6, 2013.

[66] H.J. Kang, B.J. Chun, Y.S. Jang, Y.J. Kim, and S.W. Kim. Real-time compensation of the refractive index of air in distance measurement. *Optics Express*, 23(20):26377–85, 2015.

[67] Y.S. Jang and S.W. Kim. Compensation of the refractive index of air in laser interferometer for distance measurement: A review. *International Journal of Precision Engineering and Manufacturing*, 18(12):1881–90, 2017.

[68] E. Baumann, F.R. Giorgetta, J.D. Deschênes, W.C. Swann, I. Coddington, and N.R. Newbury. Comb-calibrated laser ranging for three-dimensional surface profiling with micrometer-level precision at a distance. *Optics Express*, 22(21):24914–28, 2014.

[69] T. Onoe, S. Takahashi, K. Takamasu, and H. Matsumoto. Non-contact precision profile measurement to rough-surface objects with optical frequency combs. *Measurement Science and Technology*, 27(124002):1–7, 2016.

[70] E.W. Mitchell, M.S. Hoehler, F.R. Giorgetta, T. Hayden, G.B. Rieker, N.R. Newbury, and E. Baumann. Coherent laser ranging for precision imaging through flames. *Optica*, 5(8):988–995, 2018.

[71] David Salido-Monzú, Francisco J. Meca-Meca, Ernesto Martín-Gorostiza, and José L. Lázaro-Galilea. SNR degradation in undersampled phase measurement systems. *Sensors*, 16(10), 2016.

[72] X. Xu, Z. Zhang, H. Zhang, H. Zhao, W. Xia, M. He, J. Li, J. Zhai, and H. Wu. Long distance measurement by dynamic optical frequency comb. *Optics Express*, 28(4):4398–4411, 2020.

[73] Yu Han, David Salido-Monzú, and Andreas Wieser. Comb-based multispectral LiDAR providing reflectance and distance spectra. *Optics Express*, 30(23):42362–42375, 2022.

[74] Yu Han, David Salido-Monzú, and Andreas Wieser. Classification of material and surface roughness using polarimetric multispectral LiDAR. *Optical Engineering*, 62(11):114104, 2023.

[75] S. T. Cundiff and J. Ye. Colloquium: Femtosecond optical frequency combs. *Rev. Mod. Phys.*, 75(1):325–341, 2003.

[76] K. Meiners-Hagen, A. Bosnjakovic, P. Kochert, and F. Pollinger. Air index compensated interferometer as a prospective novel primary standard for baseline calibration. *Measurement Science and Technology*, 26(8):084002–01066, 2015.

[77] K. Hei, K. Anandarajah, E.P. Martin, G. Shi, P.M. Anandarajah, and N. Bhattacharya. Absolute distance measurement with a gain-switched dual optical frequency comb. *Optics Express*, 29(6):8108–16, 2021.

[78] W. Riley and D. Howe. Handbook of frequency stability analysis. *Special Publication (NIST SP*, 1065:1–71, 2008.

[79] J. Guillory, J. Garcia-Marquez, J.C. Alexandre, D. Truong, and J.P. Wallerand. Characterization and reduction of the amplitude-to-phase conversion in telemetry. *Measurement Science and Technology*, 26(084006):1–7, 2015.

[80] K. Meiners-Hagen, T. Meyer, J. Mildner, and F. Pollinger. SI-traceable absolute distance measurement over more than 800 meters with subnanometer interferometry by two-color inline refractivity compensation. *Applied Physics Letters*, 111(191104):1–5, 2017.

[81] K. Miyano, G. Wu, T. Makino, and K. Minoshima. Air refractive index self-correction exceeding empirical equation accuracy using two-color interferometry with optical frequency comb. In *Conference on Lasers and Electro-Optics*, page STh4H.4, 2016.

[82] J. Guillory, D. Truong, J.P. Wallerand, and C. Alexandre. A sub-millimetre two-wavelength EDM that compensates the air refractive index: uncertainty and measurements up to 5 km. *Measurement Science and Technology*, 35(025024):1–21, 2024.

[83] Y. Liu, A.Röse, G. Prellinger, P. Köchert, J. Zhu, and F. Pollinger. Combining harmonic laser beams by fiber components for refractivity-compensating two-color interferometry. *Journal of Lightwave Technology*, 38(7):1945–52, 2020.

[84] K.N. Joo and S.W. Kim. Absolute distance measurement by dispersive interferometry using a femtosecond pulse laser. *Optics Express*, 14(13):5954–5960, 2006.

[85] R. Köning, J. Flügge, and H. Bosse. A method for the in situ determination of Abbe errors and their correction. *Measurement Science and Technology*, 18:476–481, 2007.

[86] H. Wu, F. Zhang, T. Liu, J. Li, and X. Qu. Absolute distance measurement with correction of air refractive index by using two-color dispersive interferometry. *Optics Express*, 24(21):24361–76, 2016.

[87] R. Li, H. Tian, and K. Minoshima. Reduction of cyclic error induced by electromagnetic contamination in an EO-comb based distance measurement system. *Results in Optics*, 9(100308):1–6, 2022.

[88] E.N. Ivanov, S.A. Diddams, and L. Hollberg. Analysis of noise mechanisms limiting the frequency stability of microwave signals generated with a femtosecond laser. *IEEE Journal of Selected Topics in Quantum Electronics*, 9(4):1059–1065, 2003.

[89] M. Lessing, H. S. Margolis, C. Brown, P. Gill, and G. Marra. Suppression of amplitude-to-phase noise conversion in balanced optical-microwave phase detectors. *Optics Express*, 21(22):27057–62, 2013.

[90] J. Taylor, S. Datta, A. Hati, C. Nelson, F. Quinlan, A. Joshi, and S. Diddams. Characterization of power-to-phase conversion in high-speed P-I-N photodiodes. *IEEE Photonics Journal*, 3(1):140–151, 2011.

[91] J. Guillory, R. Smid, J. Garcia-Marquez, C. Alexandre, D. Truong, and J.P. Wallerand. High resolution kilometric range optical telemetry in air by radio frequency phase measurement. *Review of Scientific Instruments*, 87(075105):1–6, 2016.

[92] B. Sierro, P. Hänzi, D. Spangenberg, A. Rampur, and A.M. Heidt. Reducing the noise of fiber supercontinuum sources to its limits by exploiting cascaded soliton and wave breaking nonlinear dynamics. *Optica*, 9(4):352–359, 2022.

[93] M.A. Itzler, M. Entwistle, S. Wilton, I. Kudryashov, J. Kotelnikov, X. Jiang, B. Piccione, M. Owens, and S. Rangwala. Geiger-mode LiDAR: From airborne platforms to driverless cars. *Imaging and Applied Optics*, 2017.

[94] E. Puttonen, J. Soumalainen, T. Hakala, E. Räikkönen, H. Kaartinen, S. Kaasalainen, and P. Litkey. Trees species classification from fused active hyperspectral reflectance and LIDAR measurements. *Forest Ecology and Management*, 260(10):1846–52, 2010.

[95] J. Soumalainen, T. Hakala, H. Kaartinen, E. Räikkönen, and S. Kaasalainen. Demonstration of a virtual active hyperspectral LiDAR in automated point cloud classification. *ISPRS J Photogrammetry and Remote Sensing*, 66:637–41, 2011.

[96] S. Kaasalainen, T. Lindroos, and J. Hyyppä. Toward hyperspectral lidar: Measurement of spectral backscatter intensity with a supercontinuum laser source. *IEEE Geoscience and Remote Sensing Lett.*, 4(2):211–215, 2007.

[97] B. Chen, S. Shi, J. Sun, W. Gong, J. Yang, L. Du, K. Guo, B. Wang, and B. Chen. Hyperspectral lidar point cloud segmentation based on geometric and spectral information. *Optics Express*, 27(17):24043–59, 2019.

[98] Juan Carlos Fernandez-Diaz, William E. Carter, Craig Glennie, Ramesh L. Shrestha, Zhigang Pan, Nima Ekhtari, Abhinav Singhania, Darren Hauser, and Michael Sartori. Capability assessment and performance metrics for the titan multispectral mapping lidar. *Remote Sensing*, 8(936):1–34, 2016.

[99] E.S. Douglas, J. Martel, Z. Li, G. Howe, K. Hewawasam, R.A. Marshall, C.L. Schaaf, T.A. Cook, G.J. Newnham, A. Strahler, and S. Chakrabarti. Finding leaves in the forest: The dual-wavelength Echidna lidar. *IEEE Geoscience and Remote Sensing Letters*, 12(4):776–780, 2015.

[100] G. Wei, S. Shalei, Z. Bo, S. Shuo, L. Faquan, and C. Xuewu. Multi-wavelength canopy LiDAR for remote sensing of vegetation: Design and system performance. *ISPRS Journal of Photogrammetry and Remote Sensing*, 69:1–9, 2012.

[101] T. Malkamäki, S. Kaasalainen, and J. Ilinca. Portable hyperspectral lidar utilizing 5 GHz multichannel full waveform digitization. *Optics Express*, 27(8):A468–A480, 2019.

[102] S.A. Diddams, K. Vahala, and T. Udem. Optical frequency combs: coherently uniting the electromagnetic spectrum. *Science*, 369(267), 2020.

[103] D. Hu, Z. Wu, H. Cao, Y. Shi, R. Li, H. Tian, Y. Song, and M. Hu. Dual-comb absolute distance measurement of non-cooperative targets with a single free-running mode-locked fiber laser. *Optics communications*, 482(126566), 2021.

[104] J.A. Butt, D. Salido-Monzú, and A. Wieser. Phase ambiguity resolution and mixed pixel detection in EDM with multiple modulation wavelengths. *ISPRS Journal of Photogrammetry and Remote Sensing*, 198:255–71, 2023.

[105] K. Tan, X. Cheng, and X. Cheng. Modeling hemispherical reflectance for natural surfaces based on terrestrial laser scanning backscattered intensity data. *Optics Express*, 24(20):22971–22988, 2016.

[106] J. Qiao and J.A. Butt. Self-calibration of terrestrial laser scanner using a M3C2-based planar patch algorithm. *ISPRS Journal of Photogrammetry and Remote Sensing*, 197:335–345, 2023.

[107] F. Pedregosa, G. Varoquaux, A. Gramfort, V. Michel, B. Thirion, O. Grisel, M. Blondel, P. Prettenhofer, R. Weiss, V. Dubourg, J. Vanderplas, A. Passos, D. Cournapeau, M. Brucher, M. Perrot, and E. Duchesnay. Scikit-learn: Machine learning in Python. *Journal of Machine Learning Research*, 12:2825–2830, 2011.

[108] P. Ray, D. Salido-Monzú, A. Wieser, and T. Medić. Supercontinuum-based hyperspectral laser scanning: towards enhanced 3D surface reconstruction and its benefits for remote sensing. In *Multimodal Sensing and Artificial Intelligence: Technologies and Applications III*, volume 12621, page 126210M. SPIE, 2023.

[109] N. Sanchiz-Viel, E. Bretagne, E.M. Mouaddib, and P. Dassonvalle. Radiometric correction of laser scanning intensity data applied for terrestrial laser scanning. *ISPRS Journal of Photogrammetry and Remote Sensing*, 172:1–16, 2020.

[110] S. Kaasalainen, M. Åkerblom, O. Nevalainen, T. Hakala, and M. Kaasalainen. Uncertainty in multispectral lidar signals caused by incidence angle effects. *Interface Focus*, 8(20170033):1–10, 2018.

[111] W. Tian, L. Tang, Y. Chen, Z. Li, J. Zhu, C. Jiang, P. Hu, W. He, H. Wu, M. Pan, J. Lu, and J. Hyyppä. Analysis and radiometric calibration for backscatter intensity of hyperspectral LiDAR caused by incident angle effect. *Sensors*, 21(9):2960, 2021.

[112] J. Behmann, A.K. Mahlein, S. Paulus, J. Dupuis, H. Kuhlmann, E.C. Oerke, and L. Plümer. Generation and application of hyperspectral 3D plant models: methods and challenges. *Machine Vision and Applications*, 27:611–624, 2016.

[113] R.B. Rusu, Z.C. Marton, N. Blodow, M.E. Dolha, and M. Beetz. Towards 3D point cloud based object maps for household environments. *Robotics Autonomous Systems*, 56(11):927–941, 2008.

[114] W.S. Cleveland and S.J. Devlin. Locally weighted regression: an approach to regression analysis by local fitting. *Journal of the American statistical association*, 83(403):596–610, 1988.

[115] R.B. Rusu and S. Cousins. 3D is here: Point cloud library (PCL). In *IEEE International Conference on Robotics and Automation*, 2011.

[116] A.E. Beaton and J.W. Tukey. The fitting of power series, meaning polynomials, illustrated on band-spectroscopic data. *Technometrics*, 16(2):147–185, 1974.

[117] J. Penuelas and I. Filella. Visible and near-infrared reflectance techniques for diagnosing plant physiological status. *Trends in plant science*, 3(4):151–156, 1998.

[118] B. Datt. Remote sensing of water content in eucalyptus leaves. *Australian journal of botany*, 47(6):909–923, 1999.

[119] J. Jia, C. Jiang, W. Li, H. Wu, Y. Chen, P. Hu, H. Shao, S. Wang, F. Yang, E. Puttonen, and J. Hyyppä. Hyperspectral LiDAR-based plant spectral profiles acquisition: performance assessment and results analysis. *Remote Sensing*, 13(2521), 2021.

B | List of Publications

1. **P. Ray**, D. Salido-Monzú, R. Presl, J.A. Butt, and A. Wieser, "Refractivity corrected distance measurement using the intermode beats derived from a supercontinuum", Optics Express, 32(7), pp. 12667-12681, 2024.
2. **P. Ray**, D. Salido-Monzú, S.L. Camenzind, and A. Wieser, "Supercontinuum-based hyperspectral LiDAR for precision laser scanning.", Optics Express, 31(20), pp. 33486-33499, 2023.
3. **P. Ray**, D. Salido-Monzú, and A. Wieser, "High-precision intermode beating electro-optic distance measurement for mitigation of atmospheric delays", Journal of Applied Geodesy, 17(2), pp. 93-101, 2023.
4. **P. Ray**, T. Medić, D. Salido-Monzú, and A. Wieser, "High-precision hyperspectral laser scanning for improved radiometric correction of backscatter intensity", under-review, 2023.
5. T. Medić, **P. Ray**, Y. Han, G.A.L. Broggini, S. Kollart, "Remotely sensing inner fruit quality using multispectral LiDAR: estimating sugar and dry matter content in apples", under-review, 2023.
6. **P. Ray**, D. Salido-Monzú, A. Wieser and T. Medić, "Supercontinuum-based hyperspectral laser scanning: towards enhanced 3D surface reconstruction and its benefits for remote sensing," Proc. SPIE 12621, Multimodal Sensing and Artificial Intelligence: Technologies and Applications III, 126210M, 2023.
7. **P. Ray**, D. Salido-Monzú, and A. Wieser, "High-precision intermode beating EDM for mitigation of atmospheric delays", 5^{th} joint international symposium on deformation monitoring (JISDM), 2022.